Title
Influence of Defects' Mechanical Stability on Microscale Plasticity and Failure

Influence of Defects' Mechanical Stability on Microscale Plasticity and Failure

By

Hi Vo

A dissertation submitted in partial satisfaction of the

requirements for the degree of

Doctor of Philosophy

in

Nuclear Engineering

in the

Graduate Division

of the

University of California, Berkeley

Committee in charge:

Professor Peter Hosemann, Chair
Professor Massimiliano Fratoni
Professor Andrew Minor
Dr. Stuart Maloy

Spring 2021

Influence of Defects' Mechanical Stability on Microscale Plasticity and Failure

Abstract

Influence of Defects' Mechanical Stability on Microscale Plasticity and Failure

by

Hi Tin Vo

Doctor of Philosophy in Nuclear Engineering

University of California, Berkeley

Professor Peter Hosemann, Chair

Structural materials in nuclear applications are subjected to extreme environments including radiation flux, stress, corrosion, and temperature. These environments can induce brittle failures by changing the material microstructures through either introducing new defects or modifying the pre-existing defects. In this thesis, the role of defects' mechanical stability on the two primary causes of brittle failures, being strain localization and intergranular cracking are studied. A wide range of defect types from 0D to 3D defects – including interstitial atoms, radiation-induced loops, long-range ordered precipitates, voids, and interfaces – are considered. Additionally, the effects of radiation damage on various pre-existing defects in structural materials are studied.

The second aspect of the thesis is to expand the capability of *in situ* SEM small-scale mechanical testing for a wide range of testing geometries and material conditions. Single-crystal microcompression and microtension are developed to assess the plastic deformation of individual grains as a function of defect types. Furthermore, novel bicrystal testing of grain boundaries are developed to measure the grain boundary strength of oxidized and irradiated materials.

The key findings of the thesis reveal that the mechanical stability of the defects strongly influence strain localization, slip formation, and microscale plasticity. Furthermore, the stability of intragranular defects reduce the intergranular cracking susceptibility by inhibiting strain localization.

To my family,

Your support makes it happen

Contents
List of Figures
List of Tables
Acknowledgements

List of Figures

vii

Table of Figures

Acknowledgement

Chapter 1 - Introduction

1.1. Nuclear Energy

Nuclear fission energy has been used commercially to produce electricity for the last 60 years. The USA has been the world's largest producer of nuclear power, accounting for more than 30% of electricity generated by nuclear power in the world. There are currently 94 operating nuclear reactors; and they account for 20% of the USA's electricity production and more than 30% of the world's nuclear energy production [1,2]. In recent years, climate change due to emission of greenhouse gas (GHG) has become one of the most important issues of the 21st century. More than 190 countries have committed in an agreement signed at the United Nations Conference on Climate Change in 2015 (the Paris Agreement) to limit global warming by reducing GHG emissions [3]. The major source of GHG emissions is fossil fuels including oil, coal, and natural gas. Given the climate crisis and the urgent need to shift towards sustainable and renewable sources of energy, nuclear power has been an important alternative energy source of green and reliable baseload [2].

Figure 1-1 Current operating and under construction nuclear power plants in the US [4]

Figure 1.1 shows the map of current and under construction nuclear power plant sites in the United States. The US commercial nuclear power plants are either pressurized water reactors (PWRs) or boiling water reactors (BWRs). BWRs and PWRs also account for the majority of reactors in the world with other reactor types include heavy water reactors, gas-cooled reactors, graphite-moderated reactors, and liquid-metal-cooled reactors. While the nuclear physics behind these reactor concepts hold great prospect in terms of producing highly sustainable and clean form of energy, the materials science presented many challenges in maintaining currently

1

deployed reactors and realizing more advanced reactor concepts. The internal components of a nuclear reactor consist of many different structural materials subjected to various harsh environmental conditions including radiation flux, stress, high temperature, and corrosive environments. Figure 1.2 presents a schematic of the PWR primary and secondary loops showing the different structural materials and the corresponding environments. In the reactor core, the materials are subjected to a range of radiation fluxes (highest at the fuel rods and gradually decreasing toward the reactor vessel). The radiation damage not only changes the microstructure of the structural materials, it also causes radiolysis of coolant water which influences the material's corrosion behaviors. Low carbon and low alloy steels are used for the reactor pressure vessel, pressurizer, steam generator, and other pressure boundary components. 304 SS, 304L SS, 316L SS, and 308 SS are some of the common austenitic stainless steels for the core structural materials because they have excellent toughness for dealing with high pressure environment and excellent water corrosion resistance [1]. Nickel-based alloys such as alloy 600, alloy 690, Inconel X 750 are used for components requiring high strength (springs, steam generator tubes, fasteners).
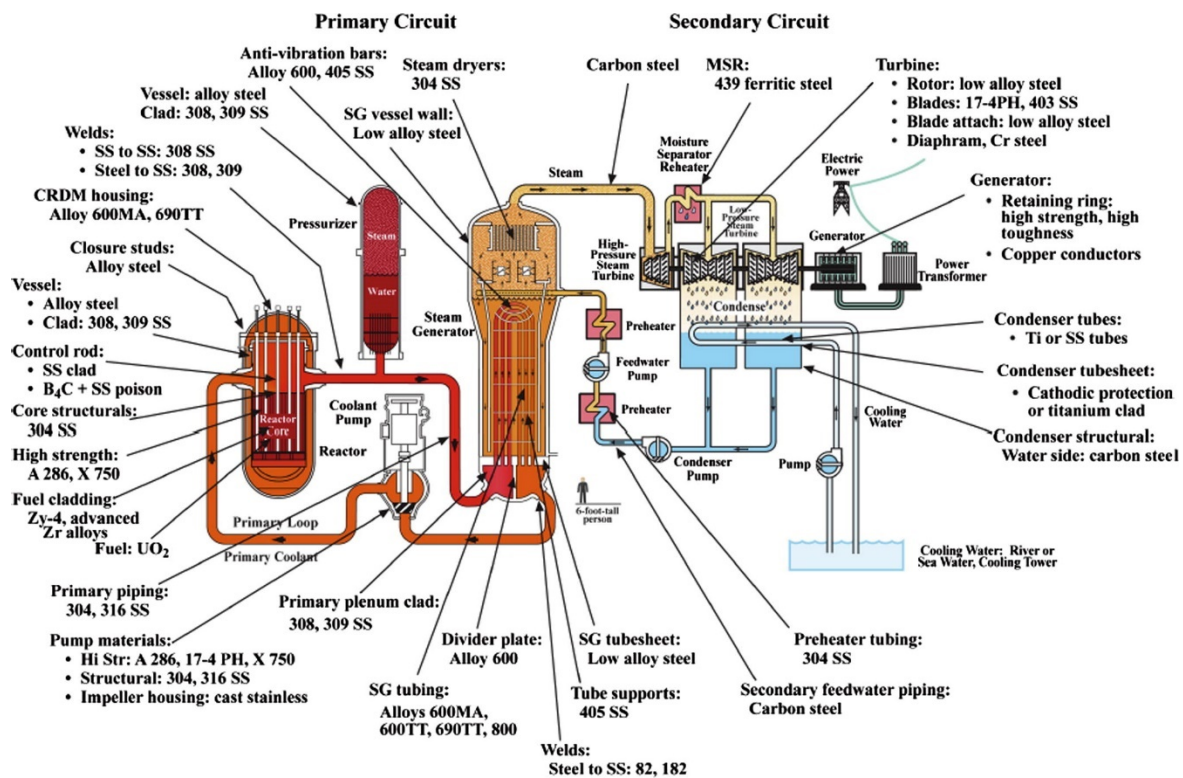
Figure 1-2 A schematic of the PWR [1] (Original source from R.W. Staehle)

Similar to PWRs, austenitic stainless steels and nickel-based alloys are used extensively for different components within the reactor interior. The BWR differs from the PWR by the fact that the BWR only consists of a single water loop instead of two water circuits. In addition to current generation, advanced reactors (Generation IV) are actively developed in order to increase fuel efficiency, increase safety, and reduce waste lifetime [5]. These advanced reactors require

materials to be subjected to much higher radiation damage (up to hundreds of displacement per atom or dpa) and higher operating temperatures. Other structural alloys such as tempered martensitic alloys (HT-9, T91), oxide-dispersed strengthened (ODS) steels and nickel-based alloys (Hastelloy) are introduced as promising candidates for structural components. One of the main challenges for all these structural materials in both the current or next generation reactors is the effect of radiation damage on the mechanical properties of these materials [6]. It can severely reduce the ductility and toughness of the structural materials, making them susceptible to brittle failures and catastrophic accidents. A classic example is shown in Figure 1.3 where the 316 SS creep tube irradiated to 140 dpa and ~400 ^{o}C has its ductility reduced to nonexistent, causing extreme brittle failure while being mounted on a vice for examination. In the following section, examples of different types of radiation-induced embrittlement are introduced.
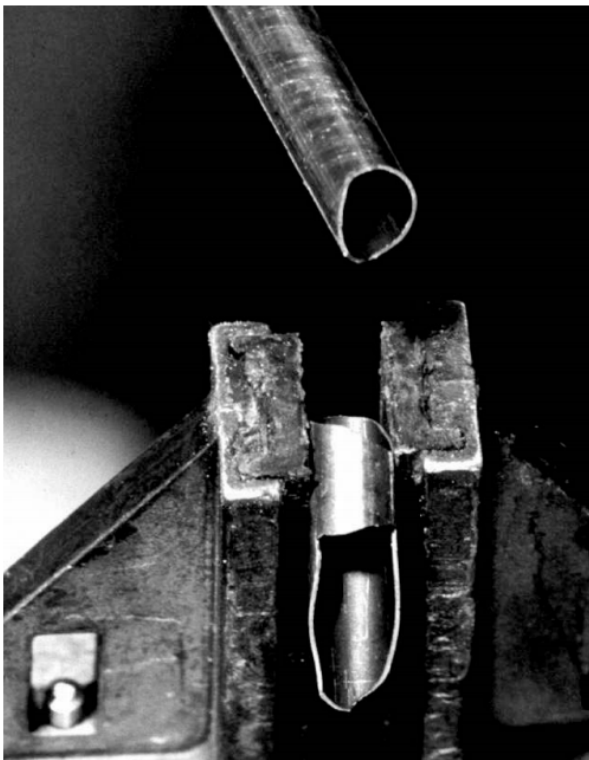
Figure 1-3 Instant failure during mounting in a vise of severely void-embrittled 316 stainless steel creep tube irradiated in the EBR-II fast reactor to 140 dpa at ~400 ^{o}C [7]

1.2. Brittle Failures induced by Radiation Damage

Before discussing about radiation damage in metals, the concept of displacement per atom (dpa) is briefly introduced. To universally express the degree of radiation damage exposure across different radiation environments (fast reactor, thermal reactor, accelerator, and fusion reactor), the radiation damage is quantified by the average number of times, each atom has been displaced from its lattice site, which is the definition of dpa. Components in the different types of reactor can reach up to hundreds of dpa during the reactors' lifetime [7]. During the irradiation, bombardment of energetic (neutron and ion) particles displace atoms from their

3

lattice sites, causing displacement cascades [8]. In this process, the interstitials, vacancies, and anti-site defects are created. While the majority of the defects annihilate during the subsequent recombination process, the remaining defects form defect clusters (vacancy and interstitial clusters), migrate to defect sinks (e.g. defect clusters, grain boundaries, voids, precipitates), or remain as anti-site defects [8,9]. Additionally, the increase in point defect concentration contributes to radiation-enhanced diffusion which can lead to phase instability (dissolution and segregation of elements). The accumulation of radiation-induced defects (interstitial/vacancy loops, voids, precipitates) lead to significant hardening and embrittlement of the structural materials. Different types of embrittlement and brittle failure were observed depending on the irradiation temperature and dose [10]. At 1>dpa and irradiation temperature <0.3Tm, the structural materials can experience embrittlement due to build-up of vacancy and interstitial loops. Figure 1.4 shows the stress-strain curves of 316L SS as a function of dpa to demonstrate the influence of radiation-induced loops. The yield strength and the flow stress increase with increasing irradiation dose while the total elongation (ductility), uniform elongation, toughness and work hardening ability decrease dramatically. The change in toughness significantly influences the safety consideration of the structural components in service.
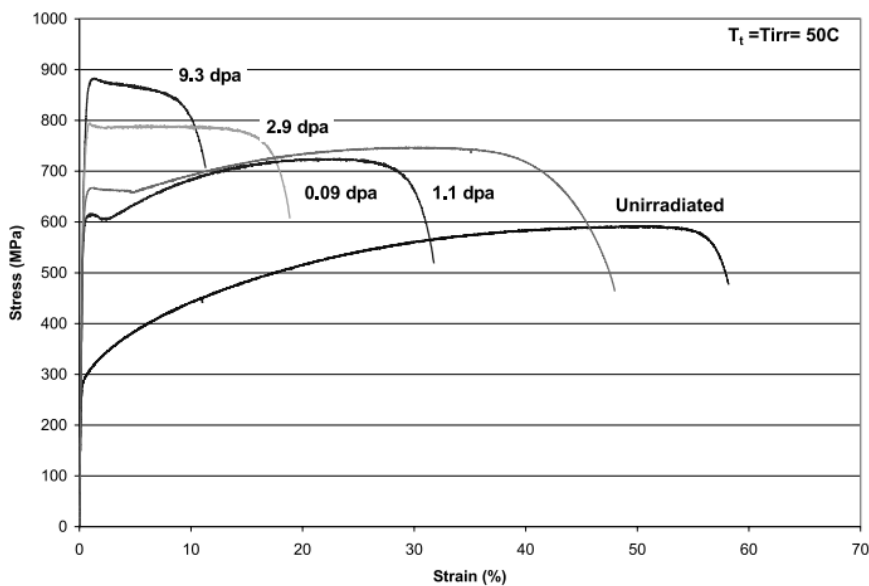
Figure 1-4 Representative stress-strain curves of macroscale tensile tests of 316L SS irradiated in spallation environment [11]

For irradiation temperatures of 0.3-0.6 Tm and >10 dpa, the metals face a different type of embrittlement induced by void swelling [10]. A classic example is the void swelling of 12X18H9T fuel assembly wrappers irradiated in BOR-60 fast reactors [7]. With void swelling of more than 14% (indicated in Figure 1.5A), the materials of the wrappers cannot plastically deform in response to stress as indicated by the severely brittle failure of the wrappers failing during the refueling operation. The bulk tensile testing of these materials shows planar facets on the fracture surface (figure 1.5B). TEM micrograph explains the planar facets to be the result of the intense shear localization of the voided microstructure (figure 1.5C).

4
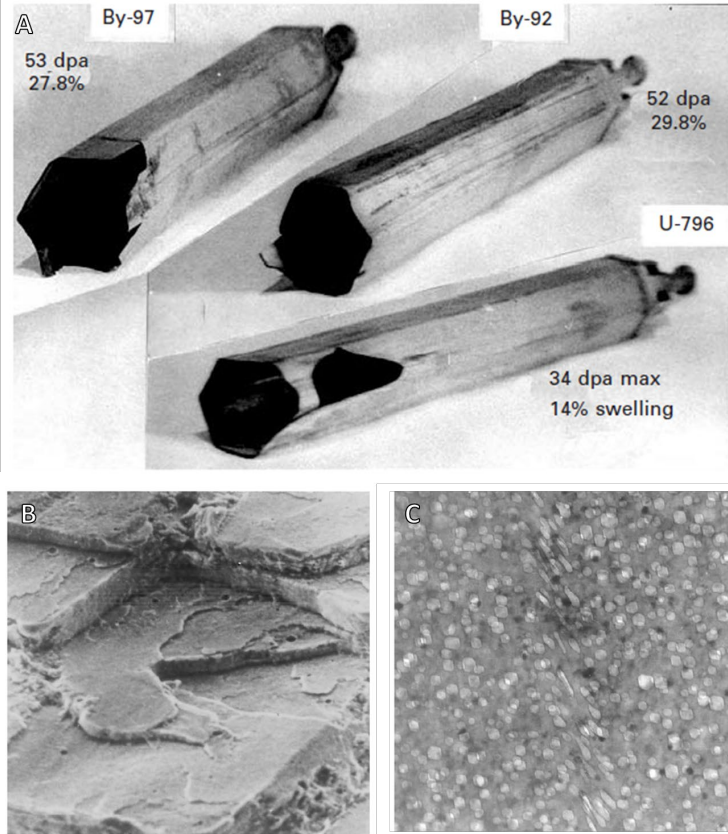
Figure 1-5 A) Void swelling of 12X18H9T fuel assembly wrappers in BOR-60 fast reactor experiencing severe brittle failure during refueling. B) Micrograph of the fracture surface of tensile test showing planar facets. C) TEM micrograph reveals intense shear localization of the voided microstructure [7]

For >0.5Tm and >10 dpa, high temperature helium embrittlement can take place within the structural materials, leading to intergranular cracking [10,12,13]. Figure 1.6 contrasts the fracture surface between the unirradiated and the Helium-implanted conditions. The unirradiated condition (Figure 1.6A) shows ductile and transgranular failure while the Helium-implanted condition exhibits brittle intergranular failure. Previous TEM results have been performed to confirm that bubbles filled with He gas decorating the grain boundaries, thus weakening the grain boundary strength of the materials [12,13].
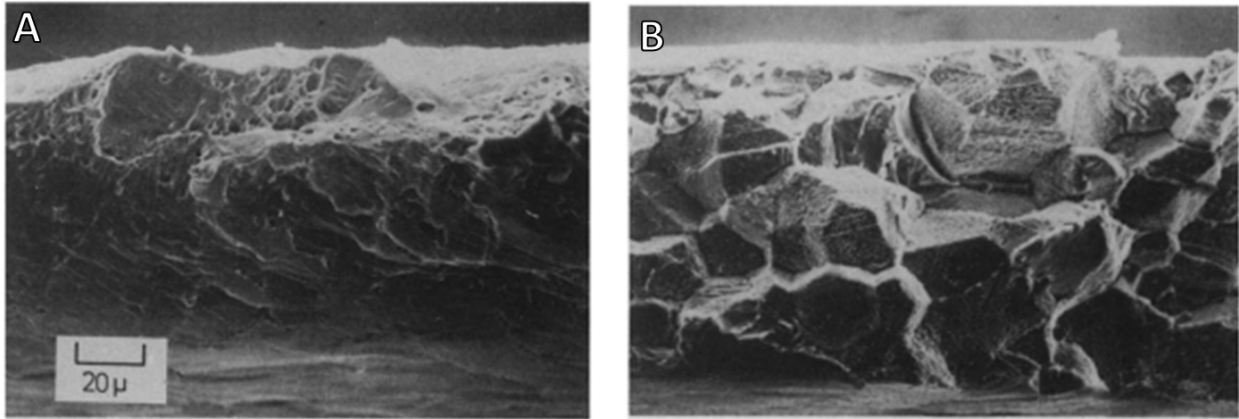
Figure 1-6 Fracture surface of a creep tube at 700 °C of A) the unirradiated and B) irradiated with 15 appm Helium [14]

These examples show that a multitude of radiation-induced changes in the microstructure can lead to embrittlement in materials observed at the macroscale. Therefore, to effectively mitigate the effect of radiation damage, it is crucial to understand how different types of defects influence the deformation and failure mechanisms within the materials. In the next section, the effect of irradiation on modifying existing defects and introducing different types of defects are discussed. Furthermore, the relevant defects for the thesis are introduced.

1.3. Defects and Radiation Damage

1.3.1. 0D Defects

Interstitial atoms and substitutional atoms strengthen the metals by solid solution hardening. The hardening is caused by the elastic interaction between the dislocations and the lattice misfit about the interstitial or substitutional impurities, as shown in Figure 1.7. For the interstitial effect, the dislocations can get locked up by the interstitial impurities, which is called the Cottrell atmosphere [15]; as a result, it requires higher stress to unpin the dislocations from their atmosphere, giving rise to the upper and lower yield points in the stress-strain curve. Schoeck and Seeger developed a model for interstitial solid solution hardening in which the yield stress is predicted to be linearly proportional to the interstitial concentration [16].
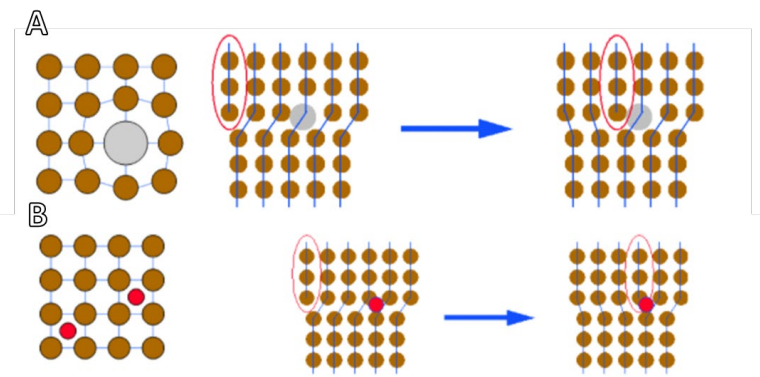
Figure 1-7 A) Representation of a substitutional atom in the matrix and its influence on the dislocation motion. B) Representation of interstitial atoms in the matrix and its influence on the dislocation motion [17]

Figure 1.8 presents the critical resolved shear stress (CRSS) versus interstitial atomic fraction of a FCC (Ni) and a BCC (Fe) metals as a function of temperature. In both metals, above a certain interstitial concentration, the CRSS is shown be linearly proportional with the interstitial atomic fraction, which is consistent with some of the previous interstitial hardening theories [16].
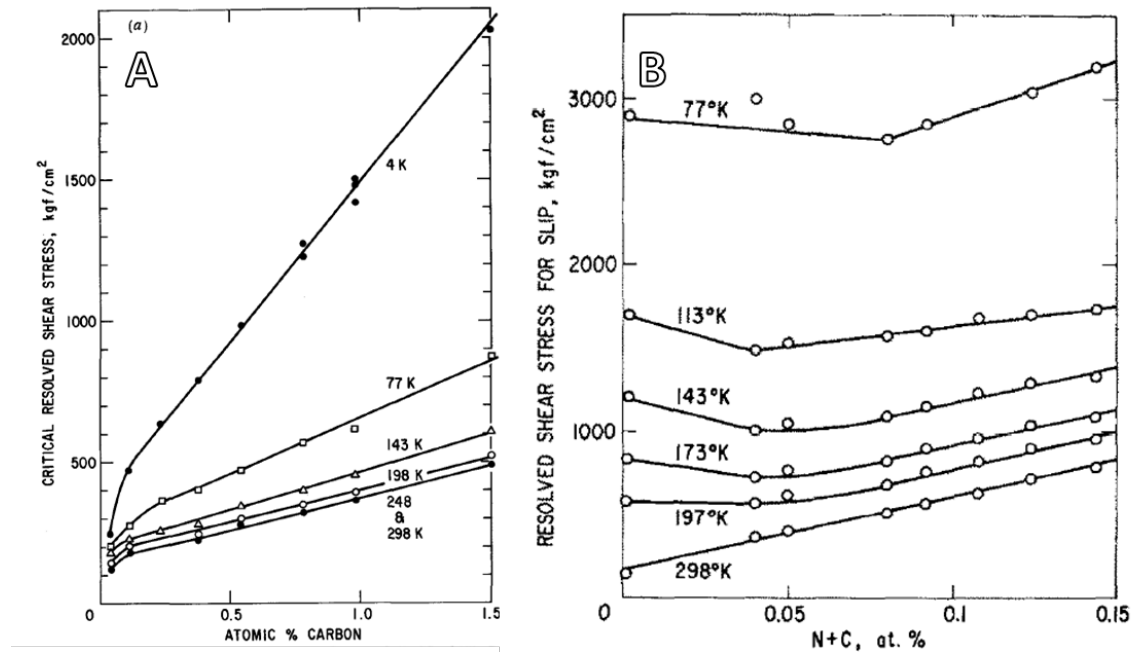
Figure 1-8 CRSS versus interstitial concentration of A) Ni metal and B) Fe metal [18,19]

Previous research has found that interstitial impurities modify the radiation-induced microstructure and consequently influence the mechanical deformation and failure of irradiated materials. Little and Harries showed that the neutron irradiated mild steel with lower Nitrogen content exhibits lower yield stress as compared to the one with higher nitrogen content across multiple dose values [20]. They suggest that the interstitial impurities are trapped by the point defect clusters and loops; thus, reducing the mobility of the point defects. Furthermore, the impurities reduce the effective self-interstitial jump rate, leading to finer distribution of vacancy and interstitial loops. Maloy et. al. [21] reported a similar observation from the tensile testing results of different tempered martensitic alloys irradiated to ~6.5 dpa in the Advanced Test Reactor, in which they suggest that there is a correlation between the post-irradiation ductility and the nitrogen concentration. Since interstitial impurity is a common defect in structural materials, it is critical to understand how the interstitial atoms modify the radiation-induced microstructures. In the thesis, the effect of nitrogen interstitial atoms on the irradiated microstructure and the resulting mechanical properties will be examined.

1.3.2. 1D Defects

In the context of irradiation damage, interstitial and vacancy loops are the primary 1D defects that significantly influence the mechanical properties of irradiated metals. As the neutron and ion particles bombard the materials, vacancies and interstitials are created as the result of displacement cascade. While the majority of the defects annihilate during the subsequent recombination process, the remaining defects form defect clusters (vacancy and interstitial clusters), migrate to defect sinks (e.g. defect clusters, grain boundaries, voids, precipitates). The formation of point defect cluster is preferred over free point defects. The binding energy of multiple interstitials is ~1 eV while the binding energy for multiple vacancies is ~0.1 eV [6]. Due the point defect clustering, extended defects such as interstitial and vacancy loops can form and grow as the irradiation continues. Figures 1.9A and 1.9B shows a schematic of a vacancy and an interstitial loop, respectively. Figure 1.9C presents the bright field (BF) TEM image of a proton-irradiated FeCr microstructure showing the presence of radiation-induced loops. These loops impede dislocation motions and give rise to the hardening and embrittlement of materials at the macroscale, as shown in figure 4 example.
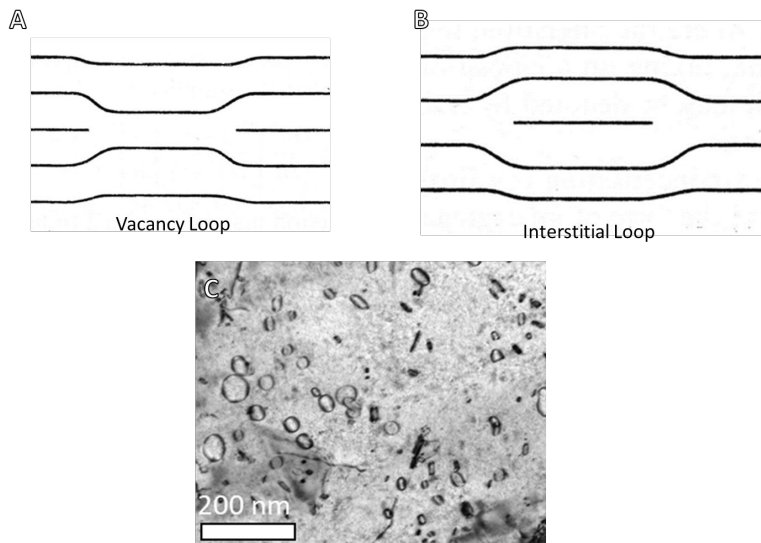
Figure 1-9. Schematics of A) a vacancy loop and B) an interstitial loop. C) BFTEM image of a proton-irradiated FeCr microstructure showing the radiation-induced loops.

1.3.3. 2D Defects
1.3.3.1. Lath and grain boundaries

Lath and grain boundaries increase the strength of the materials via dislocation pile-ups and help facilitate strain hardening. The boundaries can act as dislocation barriers during plastic deformation. For grain boundary hardening, the increase in strength follows the Hall-Petch relationship in which it is inversely proportional with the squared root of the grain size [22]. The intuitive explanation for the relationship is that as the grain size decreases, there is less space for dislocation pile-up so it requires higher stress in order for the dislocations to transmit and vice versa. The ability for a lath or grain boundary to act as an effective dislocation barrier depends

on the grain boundary characteristic and dislocation transmission ability. However, there are multiple different interactions that can occur between dislocations and grain boundaries. The interactions are detailed in [23]. When interacting with a grain boundary, the dislocations can either pile up, annihilate, dissociate, or transmit. Some of the interactions are characterized as follows:

1. The dislocation fully transmits without leaving a residual Burger vector (Figure 1.10A)
2. The dislocation partially transmits and leaves behind a residual dislocation at the grain boundary in order to account for the difference in Burger vector of the incoming and transmitted dislocations (Figure 1.10B)
3. The dislocation is absorbed at the grain boundary and emitted from a different location on a grain boundary (Figure 1.10C)
4. The dislocation is piled up at the grain boundary and no transmission takes place (Figure 1.11D)

A. Transmission without leaving residual Burger vector at GB

B. Direct transmission, leaving residual Burger vector at GB
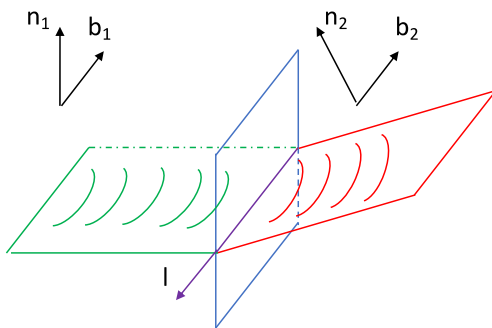
Screw dislocation – Transmission by climb

$b_1 \, // \, b_2 \, // \, l$, tilt boundary
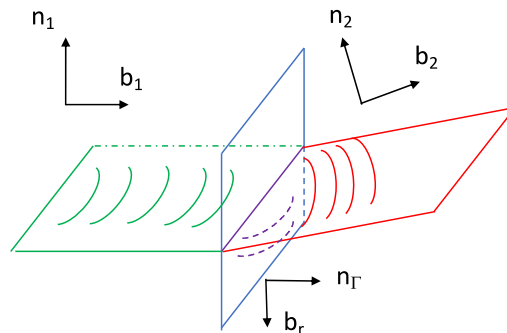
$b_1 \nparallel b_2$

C. Indirect transmission, leaving residual Burger vector at GB
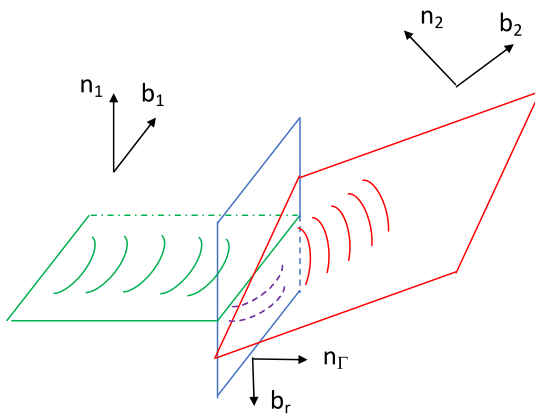
D. No transmission

Where $b_r = b_2 - b_1$, twist and mix boundary

9
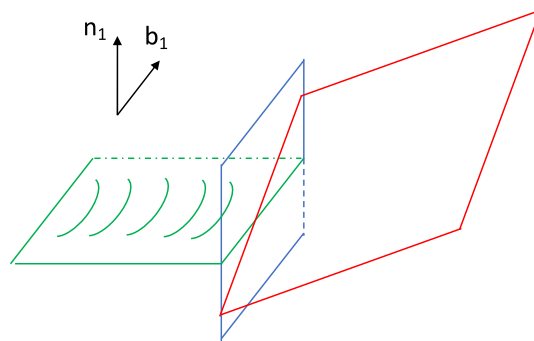
Figure 1-10 Schematics of different dislocaiton-boundary interacitions: A) Complete dislocation transmission with no residual Burger vector. B) Partial dislocation transmisison with residual Burger vector. C) Indirect transmission. D) No transmission

The cumulative slip transmission coefficient, λ, of a grain boundary is a simple approach to quantify the ability of a grain boundary to transmit dislocations [24]. The transmission coefficient λ is given as:

$$\lambda = \sum_A \sum_B \cos\left(\frac{90^o}{\omega_c} arcos(\bar{n}_A * \bar{n}_B)\right) \cos\left(\frac{90^o}{\kappa_c} arcos(\bar{d}_A * \bar{d}_B)\right) \quad Eq\ 1.1$$

$$= \sum_A \sum_B \cos\left(\frac{90^o}{\omega_c}\omega\right) \cos\left(\frac{90^o}{\kappa_c}\kappa\right) \quad Eq.\ 1.2$$

where ω, ω_c are the angle and critical angle, respectively, between the normal vectors of the incoming and outgoing slip planes, κ, κ_c are angle and critical angle, respectively, between the slip directions of the incoming and outgoing slip systems. Slip transmission is expected to occur if $\kappa < \kappa_c$ and $\omega < \omega_c$. For FCC grain boundaries, κ_c and ω_c are 45° and 15°, respectively [24]. A λ value of 12 means that the grain boundary is transparent to dislocation motion and a λ value of 0 means that the grain boundary is a perfect barrier. A schematic of slip transmission and the relevant parameters is shown in Figure 1.11.
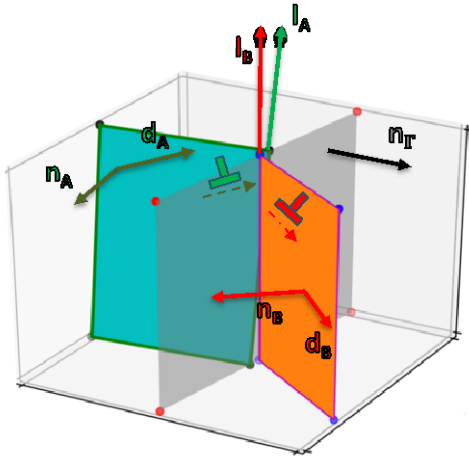
Figure 1-11 Schematic of two adjacent slip systems for transmission analysis. $\bar{n}_A$, $\bar{n}_B$ are the normal vectors of slip systems A and B; $\bar{d}_A$, $\bar{d}_B$ are the slip directions of slip systems A and B; $\bar{l}_A$, $\bar{l}_B$ are the intersection vectors between the slip planes A and B, respectively, with the grain boundary; $\bar{n}_\Gamma$ is the normal vector of the grain boundary.

Under reactor environments, the lath and grain boundaries can be compromised due to radiation damage and corrosion (e.g. corrosion due to primary light water reactor coolant [25,26]). The radiation damage can lead to radiation enhanced diffusion and further promote elemental segregation at the grain boundary [27]; additionally, the slip localization (dislocation free

channeling) caused by radiation hardening can increase the local stress intensity at the grain boundaries, leading to intergranular crack formation [28]. Intergranular oxidation of nickel-based alloys 600 and 690 in PWR water chemistry has been extensively reported to cause intergranular embrittlement [25,26]. From microscale perspective, the oxidation and radiation-enhanced diffusion modify the grain boundary by introducing a new brittle interface that is not transparent to dislocation motions. Thus, it modifies grain boundary cohesion strength and other mechanical properties of grain boundaries, which have an important effect on the intergranular failure of the structural components [26]. The deformation and failure related to oxidized grain boundaries in Ni alloy 600 and lath boundaries in proton-irradiated HT9 will be discussed in the thesis.

1.3.4. 3D Defects

The common 3D defects found in structural metals are disordered precipitates, ordered precipitates (intermetallics), voids, and He bubbles. Some are added in the metals via thermal treatment to provide low and high temperature strength, creep resistance, and fatigue resistance while others such as voids and bubbles are introduced as the result of radiation damage. Furthermore, radiation damage can also modify the existing 3D defects through disordering and dissolution. The prime example is the disordering and dissolution of long range ordered (LRO) precipitates in Nickel-based alloys. In the thesis, voids and LRO precipitates are examined as they are key 3D defects and they cover a wide range of plastic formation and failure.

1.3.4.1. Voids

At higher temperature, void nucleation and growth due to irradiation damage are common in structural materials. BFTEM image of neutron irradiated steel with microstructure consisting of voids is shown in Figure 1.12A. The void swelling curves versus neutron fluence of a neutron irradiated 316 stainless steel is shown in Figure 1.12B. The 1%/dpa void swelling rate is standard in austenitic stainless steels [7]. The materials first undergo an incubation period followed by a typically linear growth rate. The void swelling is depending on the irradiation temperature, the sink density (grain boundaries, dislocation density, precipitate density), and dose rate. As shown in Figure 1.12B, the void swelling increases from 400°C and peak at 510°C then decreases at higher temperature. By changing the dose rate, the peak void swelling temperature is shifted. The condition for void growth requires that there is a preferential absorption of interstitials over vacancies at defect sinks. One example of such defect sink is dislocation network. Dislocations preferentially absorb interstitials more than vacancies; thus, creating an excess in vacancy concentration during steady state. Furthermore, the mobility of interstitials is higher than that of vacancies so they can escape recombination and migrate to defect sinks. When vacancies form clusters, they can collapse into loops or faults; but if alpha particles (Helium gas) can stabilize the vacancy clusters and promote formation and growth of cavities. If the cavities are pressurized, they are considered as bubbles; otherwise, they are voids.
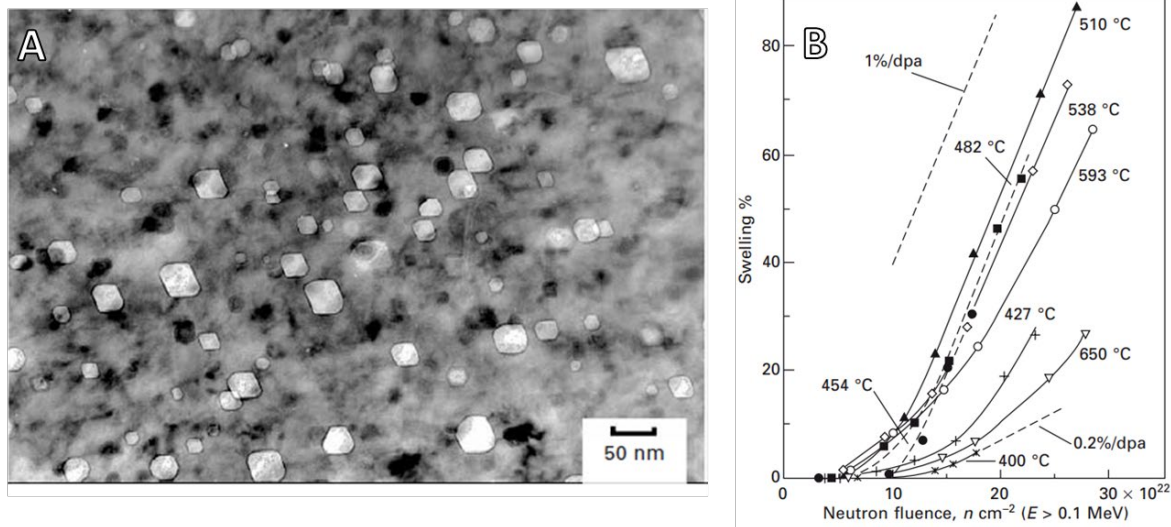
Figure 1-12 A) Voids observed in anneal AISI 304 irradiated in EBR-II fast reactor at 380 °C. B) Void swelling curve vs neutron fluence of 20% cold-worked AISI 316 irradiated in the EBR-II fast reactor [7]

Molecular dynamics simulations have been performed to investigate the dislocation-void interaction [29]. The dislocations can either shear or loop about the voids depending on the voids' size and spacing. The hardening model that best describes the hardening due to voids is Bacon-Kocks-Scattergood model [30]. Unlike radiation-induced loops, the voids are stable and not dissolvable. It might suggest that voids are more resistant to dislocation free channeling formation. At very high level of swelling of above 10% (Figure 1.5), there is no plasticity within materials. However, it is of interest to examine the influence of voids on the dislocation free channeling formation at low level of swelling (1-3%).

1.3.4.2. Long-ranged ordered (LRO) precipitates
1.3.4.2.1. L1$_2$ and DO$_{22}$ -structured precipitates and the radiation-induced disordering and dissolution

As mentioned in the previous section, nickel-based alloys are widely used for applications under radiation producing environments; as they offer exceptional mechanical properties at high temperatures and corrosion resistance. In particular, the complex dislocation and precipitate interactions are responsible for the high and low temperature strength of nickel-based alloys [31–33]. The precipitates are introduced into the alloys through the addition of Ti, Cr, Nb and Al elements and the appropriate thermal treatment [34–36]. The precipitates are intermetallics with different long-range ordered (LRO) structures; some of the common LRO structures are L1$_2$, DO$_{22}$, and Pt$_2$Mo [37–45]. L1$_2$ and DO$_{22}$ LRO precipitates are found in variety of nickel-based alloys used in nuclear accelerator applications [41,46]. In the thesis, we will focus on nickel-based alloy 718 but the deformation mechanism is similar to other nickel-based alloys containing the same LRO precipitates. The LRO precipitates in Inconel 718 are γ' Ni$_3$(Al,Ti) and γ'' Ni$_3$Nb with the LRO structures of L1$_2$ and DO$_{22}$, respectively. Figure 1.13A and 1.13B show the crystal structures of γ'

L1$_2$ and γ'' DO$_{22}$, respectively; and the diffraction pattern of inconel 718 taken along <100> zone showing the superlattice reflection of the LRO precipitates.
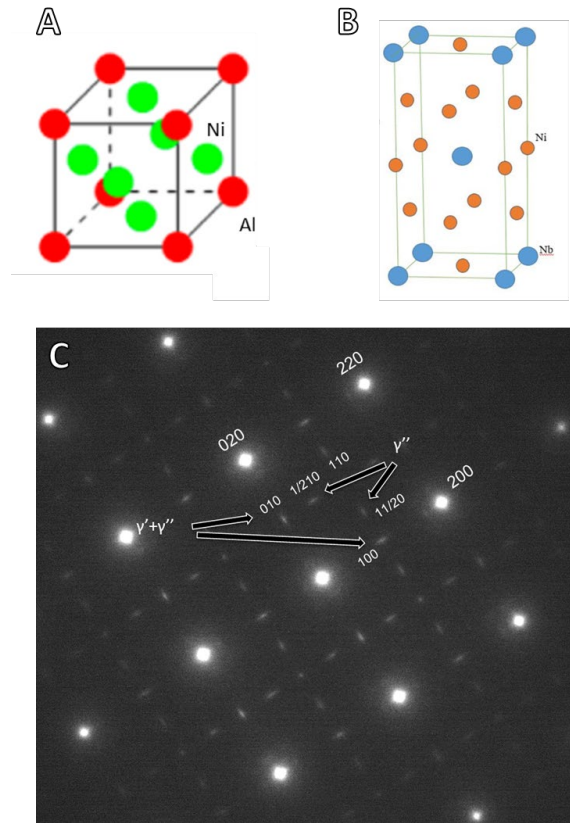
Figure 1-13 Crystal structure of A) L1$_2$ γ' and B) DO$_{22}$ γ'' [47]. C) Selected area diffraction pattern of Inconel 718 showing the precipitate superllatice reflection.

Extensive research established the strengthening mechanisms of L1$_2$- and DO$_{22}$-structured precipitates [37,39–42,45,48]. At low temperatures the strengthening originates from two main mechanisms: Orowan strengthening and anti-phase boundary (APB) strengthening [48–50]. Hardening laws such as dispersed barrier hardening (DBH) [51] and Bacon-Kocks-Scattergood (BKS) [52] laws have been developed to calculate the increase in flow stress for a given distribution of precipitates. In the scenario where the dislocations shear through the LRO precipitates, the APB strengthening becomes dominant as a result of the additional energy required to create and extend the APB. Previous studies have shown that the structure of the ordered precipitates dictates the dislocation behavior when interacting with the LRO precipitates [42,43,45] . For L1$_2$-structured precipitates, the dislocations travel in pairs to minimize the ABP created as the dislocations shear through the LRO precipitates, as shown in Figure 1.14.
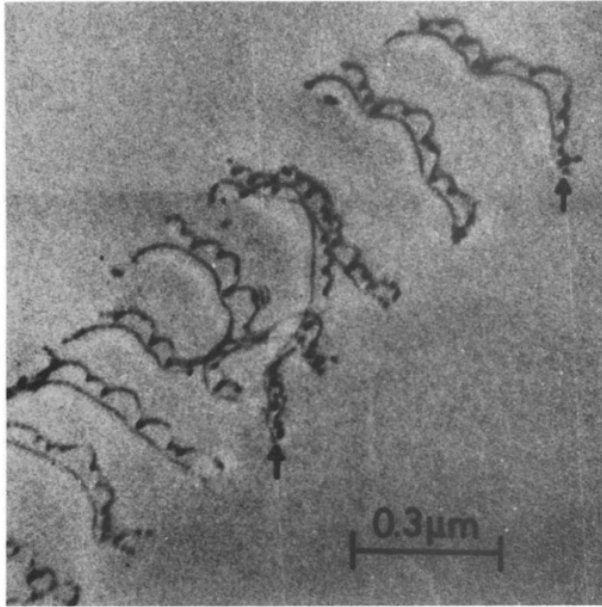
Figure 1-14 Transmission electron micrograph of the dislocation pairs gliding in Ni alloy containing L1$_2$ -structured precipitates. [42]

As the first dislocation shears the L1$_2$-structured precipitates, the order of the precipitate is disrupted and an APB is created. To minimize the energy cost for creating the APB, the second dislocation travels closely behind to restore the order of the precipitate and remove the APB. A similar mechanism is also reported for DO$_{22}$-structured precipitates [45]. This mechanism allows the LRO precipitates to maintain the superior strength of Inconel 718 Nickel-based alloy strengthened by γ' and γ'' LRO precipitates. However, the stability of the LRO precipitates can be compromised. As an example, the LRO precipitates can become locally disordered and dissolved due to extensive dislocation shearing [39,53–58]. As a consequence, dislocation motion takes place preferentially on the particular slip planes with lower slip resistance due to the local dissolution of LRO precipitates, leading to strain localization [18, 20–25]. The local loss in LRO-precipitate strengthening can lead to a severe effect on the ductility and toughness of the structural alloys as it can cause catastrophic failure of the components deployed, particularly in harsh environments such as radiation and corrosion.

14
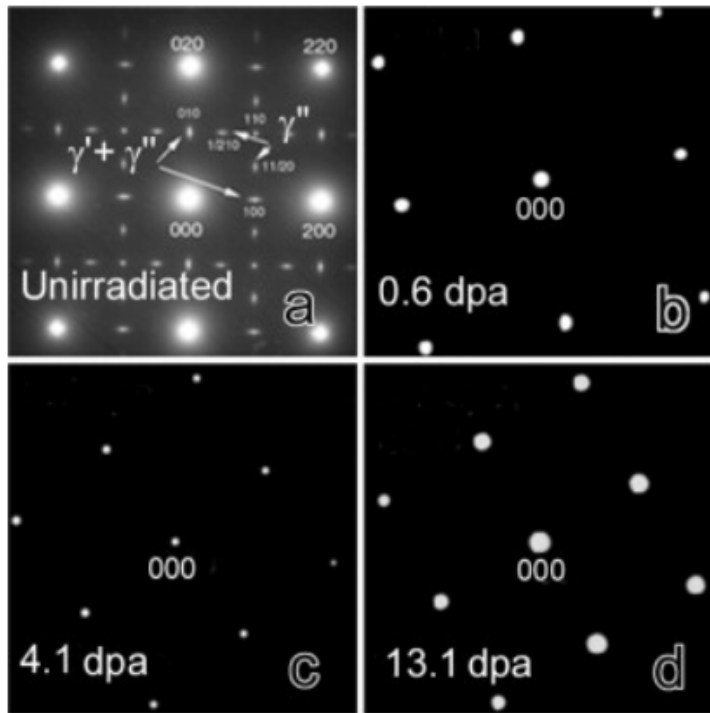
Figure 1-15 Selected area electron diffraction parrterns of Alloy 718 showing A) unirradiated, B) 0.6 dpa irradiated, C) 4.1 dpa irradiated, and D) 13.1 dpa irradiated [59]

In addition to introducing new defects into the materials, radiation damage can effectively disorder and dissolve the preexisting strengthening defects such as LRO precipitates, leading to significant degradation of the bulk mechanical properties [60–62]. Previous research [63–66] has established that LRO precipitate disordering process can be described by the thermal spike model and the dissolution process is described by ballistic mixing model. It was found that in high energy proton-irradiated Inconel 718, γ' and γ'' LRO precipitates become disordered at a very low dose (< 0.6 dpa) and gradually dissolved at a higher dose [59,62]. As shown in Figure 1.15, the superlattice reflection of the LRO precipitates in Inconel 718 quickly decrease in intensity and disappear as a function of dose. This indicates that the irradiation has fully disordered the LRO precipitates as low as 0.6 dpa . Additionally, Maloy et al. [62] showed that the uniform elongation drops below 2% at 0.5 dpa while the yield stress remains relatively unchanged and gradually decreases as the dose increases. More importantly, the fracture toughness also decreases rapidly which is similar to the UE trend. Figure 1.16 plots the uniform elongation (UE), total elongation, and yield strength of the proton-irradiated Inconel 718 as a function of dose [62]. The rapid disordering of LRO precipitates at low dose poses a question on the role of disordering on strain localization and embrittlement (reduction in uniform elongation and toughness) of Inconel 718 and other nickel-based alloys. Therefore, one of the objectives in our work is to investigate the effect of irradiation-induced disordering of the precipitates on the change in the deformation behavior of nickel-based alloys.
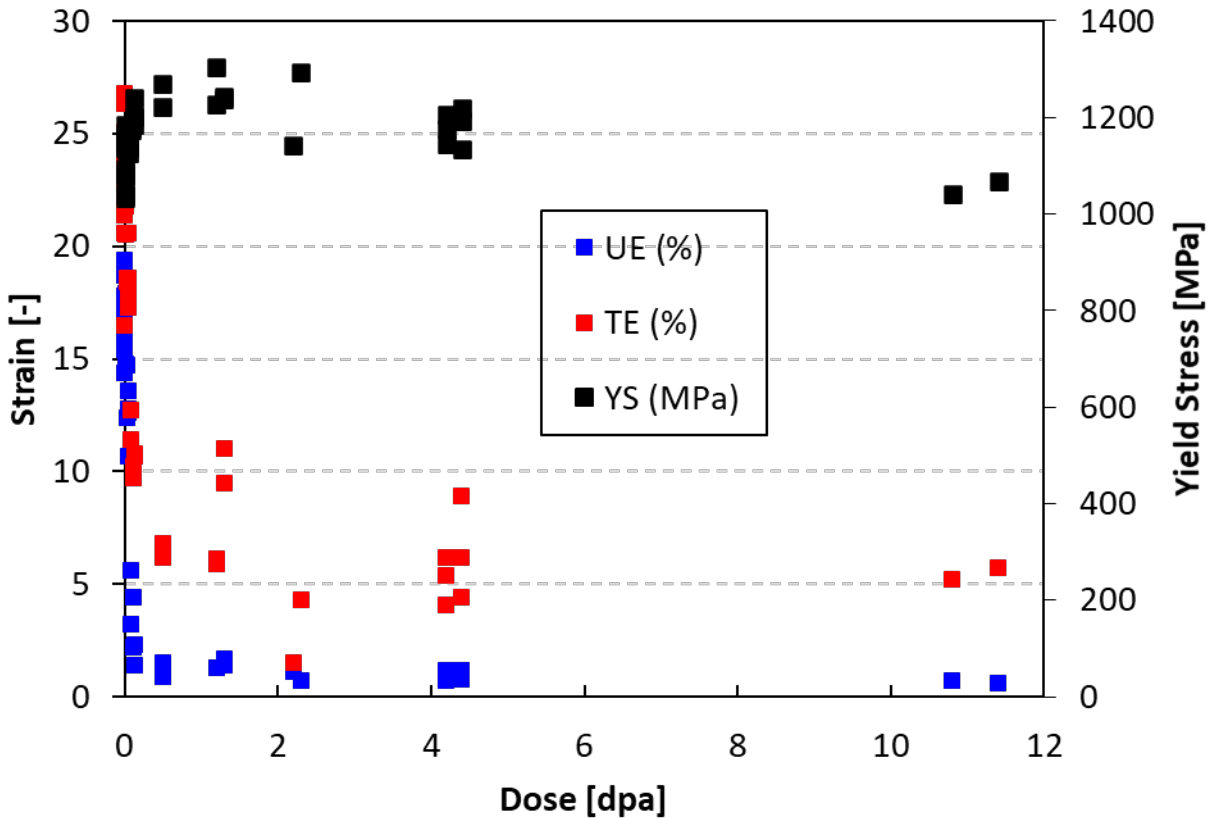
Figure 1-16. The UE and TE versus dose plot, with permission to replot from [62]

1.3.4.2.2. Pt₂Mo -structured precipitates and the radiation-induced precipitation

In addition to L1$_2$ and DO$_{22}$, Pt$_2$Mo-structured precipitate type is an important strengthening 3D defect in NiCr and NiCrMo alloys. These Ni based alloys are used in the current and the next generation of reactors [67]. The Pt$_2$Mo-structure precipitates (Ni$_2$Cr or Ni$_2$(Cr,Mo)) are introduced via either thermal aging or radiation-induced precipitation. In addition to the disordering and dissolution radiation damage introduces, radiation enhanced diffusion can lead to precipitation of disordered (e.g. Cr-rich precipitates or α' in FeCr alloy [68]) and ordered defects (e.g. intermetallic precipitates such as Pt$_2$Mo-structured precipitates in NiCrMo alloys [67]). Proton-irradiation has been systematically performed in various NiCr and NiCrMo alloys and the post-irradiation microstructures reveal radiation-induced precipitation of Pt$_2$Mo-structured precipitates [67]. Figure 1.17A shows the Pt$_2$Mo structure of Ni$_2$Cr precipitates in NiCr alloy and the orientation relationship between the LRO unit cell and the FCC matrix. The TEM diffraction pattern, in Figure 1.17B, shows the superlattice reflection of the Pt$_2$Mo-structured precipitates of a NiCrMo alloy irradiated with 2.5 dpa proton dose [67]; and Figure 1.17C provides the corresponding darkfield TEM image.

16
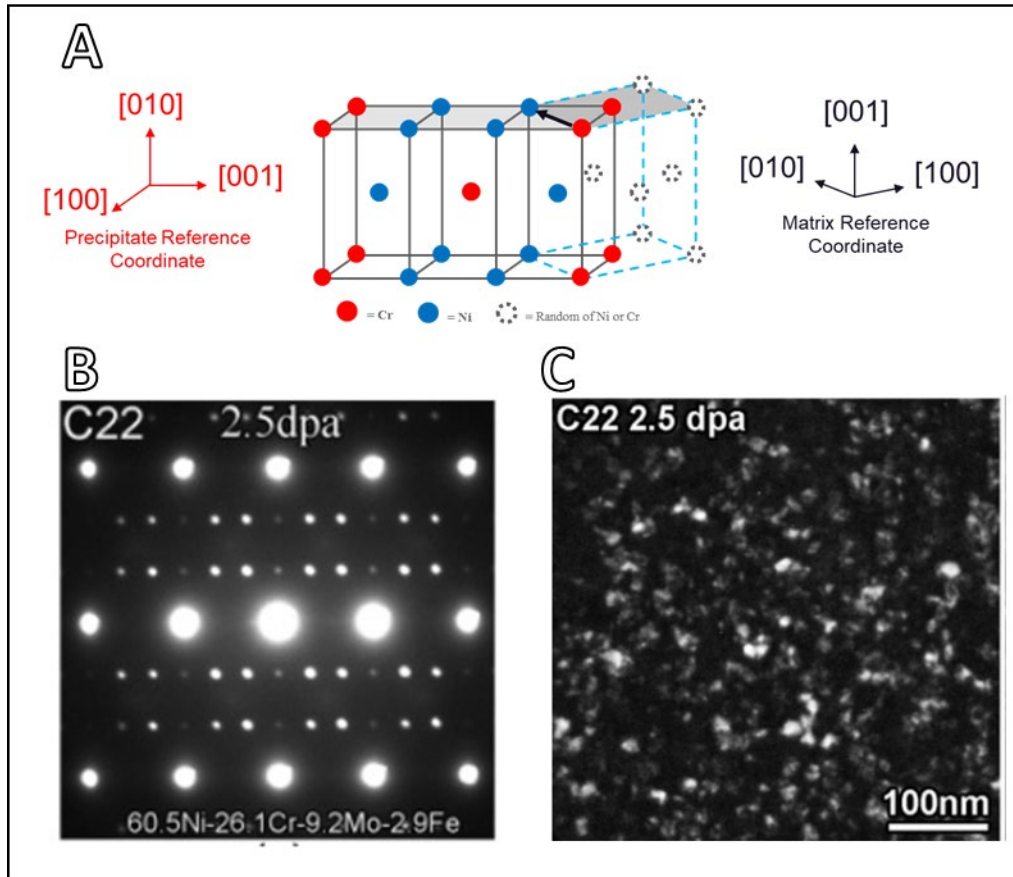
Figure 1-17 The crystallographic orientation relationship between the Ni$_2$Cr LRO unit cell and the Ni$_2$Cr disordered FCC matrix. The dash blue lines represent the unit cell of the FCC matrix and the black lines represent the unit cell of the Ni$_2$Cr ordered structure, B) the selected area diffraction pattern and C) the dark field TEM image of an irradiated Ni alloy indicating the precipitation of LRO Pt$_2$Mo-structured precipitates [67]

Aside to the usual dislocation shearing mechanism discussed in L1$_2$ and DO$_{22}$-structured precipitates above, deformation twinning plays a big role in Ni based alloys containing Pt$_2$Mo-structured precipitates. Deformation twinning in Ni based alloys have been extensively studied. Most notably, thermally-activated microtwinning in widely-used nickel-based alloys containing Ni$_3$Al-based, L1$_2$-structured precipitates, have been observed and extensively studied at the intermediate temperatures (650-800° C depending on the Ni-based alloys) [37,69]. However, the deformation twinning mechanism is much less understood in Ni-Cr and Ni-Cr-Mo type alloys containing Pt$_2$Mo-structured precipitates (such as Ni$_2$Cr, Ni$_2$Mo precipitates). Room temperature bulk mechanical testing of these alloys have shown strong hardening response as a function of aging time and temperature without substantial loss of ductility [43,44,70–73]. Transmission Electron Microscopy (TEM) studies reveal that deformation occurs predominantly via slip in the unaged alloys, while mechanical twinning is dominant in the aged alloys, containing Pt$_2$Mo-structured precipitates [44,70–73]. From these works, it was proposed that the Pt$_2$Mo-structured precipitates promote mechanical twinning; thus, enhancing the ductility of the Ni-based alloys. In general, the role of mechanical twinning in increasing ductility, fracture toughness, and

strength has been shown in many different classes of alloys [74,75], so it is not surprising to see similar strengthening mechanisms are activated in these Ni-based alloys. What remains unclear is the Pt_2Mo-structured precipitate-induced deformation twinning mechanism. Some previous bulk scale mechanical studies have provided a geometric-based rationale for the observation of deformation twinning [43,71,72]. These explanations stated that 10 out of the 12 slip systems interact with the precipitate by APB shearing while the remaining 2 slip systems do not disrupt the order of the precipitates. For those 10 slip systems, the corresponding twinning systems are preferred to be active as the formation of the dislocation stacking fault does not disrupt the order of the LRO precipitates. In order words, this suggests that there is a loading orientation dependence on the twin versus slip activations in the nickel-based alloys containing Pt_2Mo-structured precipitates in contrast to the $L1_2$- and DO_{22}- structured precipitates. Currently, there has not been a direct observation of the loading orientation effect on the resulting deformation modes (slip versus twin). Furthermore, the twin formation process (and twin thickening) due to Pt_2Mo-structured precipitates needs to be further explored. Given the technological importance of the Ni-Cr and Ni-Cr-Ni type alloys in the nuclear power industry and other applications [67,76], it is important to establish a comprehensive understanding of the loading orientation dependence on the deformation modes and the twin formation process for the nickel-based alloys containing Pt_2Mo-structured precipitates. In particular, the role of deformation twinning in stabilizing plastic flow and strain localization will be considered.

1.4.   Defects and plastic stability and failure

So far different macroscopic failures have been mentioned in section 1.2 and the different defects can be introduced or affected by radiation environments are discussed in section 1.3. In this section, the different causes of embrittlement are discussed to establish a connection between defects and macroscopic embrittlement. Two main causes of embrittlement in structural materials used in radiation producing environments are strain localization and grain boundary failure. The focus of the thesis is to examine how different defect types, introduced in section 1.3, contribute to these two types of failures. A well-known case study is the strain localization due to radiation-induced loops [77]. Figure 1.4 shows the result of the accumulation of radiation-induced loops on the stress-strain curves of proton irradiated stainless steels as a function of irradiation dose. As the dose increases, the uniform elongation, strain hardening ability, and fracture toughness decrease rapidly. Previous studies have revealed that strain localization is a dominant deformation mechanism resulted from the interactions between dislocations and radiation-induced loops [77]. Figure 1.18A represents a schematic of a macroscopic irradiated tensile specimen under tensile load. The specimen consists of multiple grains and under deformation, discrete localized slip form in contrast to the diffuse slip observed in unirradiated materials. For radiation-induced loops, formation of the localized slip is due to the effect of dislocation free channeling. Dislocation dynamics (Figure 1.18B) and post-deformation TEM characterization (Figure 1.18C) have confirmed that the dislocations clear out the radiation-induced loops as the dislocations interact with the loops, thus creating defect free channels. As the consequence, the dislocation resistance on these defect free channels is substantially lowered as compared to the rest of the material, allowing dislocations to preferentially glide in these channels. The preferentially dislocation motion on these channels

18

directly lead to the observation of localized slip or strain localization as shown in the schematic Figure 1.18A. Von Mises and Taylor have stated that it requires minimum of five independent slip systems in order for the test specimen to accommodate any plastic strain tensor. The full proof is included in [78]. When dislocation free channels are formed, plasticity is confined within those channels so it prevents the activation of multiple of independent slip systems. This constraint directly limits strain hardening (requires the interaction of different slip systems) and grain boundary rotation (limits the uniform elongation regimes). Therefore, strain localization within the grains has a direct effect on strain hardening, uniform elongation, and toughness. Additionally, strain localization has been reported to increase the stress intensity at the grain boundary and consequently initiate intergranular cracks in stress corrosion cracking experiments (Figure 1.18D) [28]. Given the importance of strain localization in causing embrittlement at the macroscale, one of the objectives of the thesis is to assess effect of the interactions between the dislocations and the different defect types discussed in section 1.3, on strain localization.
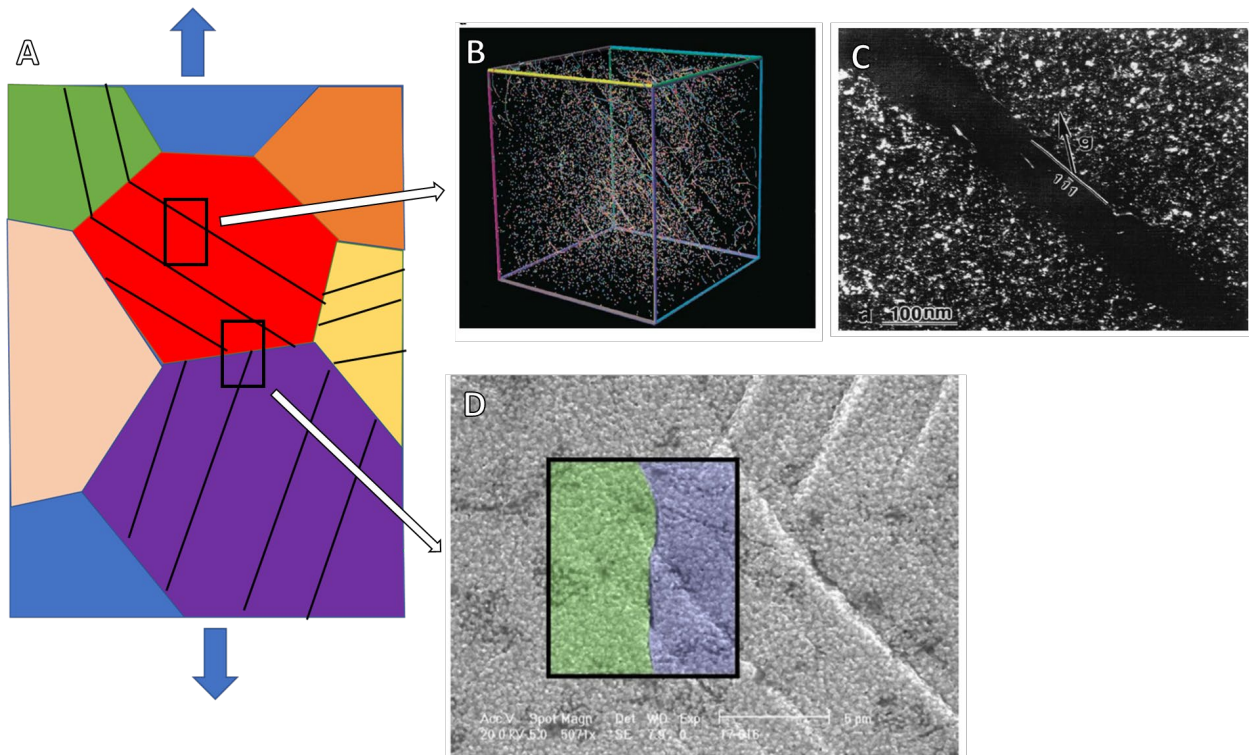
Figure 1-18. A) Schematic of an irradiated polycrystal metal specimen under tension load showing localize slip. B) Discrete dislocation dynamics simulation showing dislocation free channel formation after dislocation interaction with self-interstitial loops. C) Weak beam dark field TEM micrograph confirms the presence of defect free channel in deformed irradiated Cu sample. [28]

Second cause of brittle failure in structural materials is intergranular failure. From the schematic in Figure 1.18A, in addition to the deformation within the grains, the dislocation-grain boundary interaction and the grain boundary strength play a crucial role in influencing the macroscopic deformation and failure. The dislocation and grain boundary interaction can dictate the stress intensity seen at the grain boundaries, as shown in the example of strain localization.

Furthermore, the nuclear reactor environment can also modify the grain boundaries via corrosion and radiation-induced segregation [26,27], weakening the grain boundary strength. As the results, the grain boundaries are more susceptible to crack initiation and propagation. In the thesis, oxidized grain boundaries (induced by water corrosion) and grain boundaries of irradiated materials) will be examined to investigate their influence on intergranular failures at the microscale.

1.5.   Small scale mechanical testing

To isolate the effect of particular defect types on deformation mechanisms, we utilized small scale mechanical testing (SSMT) via in situ SEM microtensile and micropillar testing. The introduction of small-scale mechanical testing (SSMT) by M. Uchic et al.[79] has enabled a thorough understanding of mechanical properties of materials at small length scales, from nanoscale to microscale [80–85]. With the ability to probe specific microstructural features and infer qualitative bulk properties from microscale tests, SSMT offers unparalleled practical advantages over conventional macroscale testing in many important industries such as nuclear power, micro-electro-mechanical system (MEMS) devices [86], and advanced coating [87]. It has proven to be an effective technique to study various fundamental deformation mechanisms such as material size effects [79,80,83,84,88–94], plastic instabilities (strain burst) [79,95–99], grain size effects [93,100,101], and others.

SSMT is particularly useful in the nuclear materials community as it provides the ability to test ion-beam irradiated materials. Ion-beam irradiation has been more extensively used to study radiation damage of structural materials as a surrogate for neutron irradiation to save time and cost. It offers the advantage of high dose rate, little to no activation, and excellent control over the irradiation condition [102] but the limitation of the irradiation depth to tens of micrometers makes conventional. Since SSMT provides the ability to probe small volume, it can assess the mechanical properties of thin ion-irradiated layers. Figure 1.19 shows a schematic of an ion-irradiated materials and some of the different SSMT techniques including nanoindentation, micropillar testing, and microtensile testing [95,103]. With high precision, mechanical response of specific location corresponding to the dose profile can be measured.
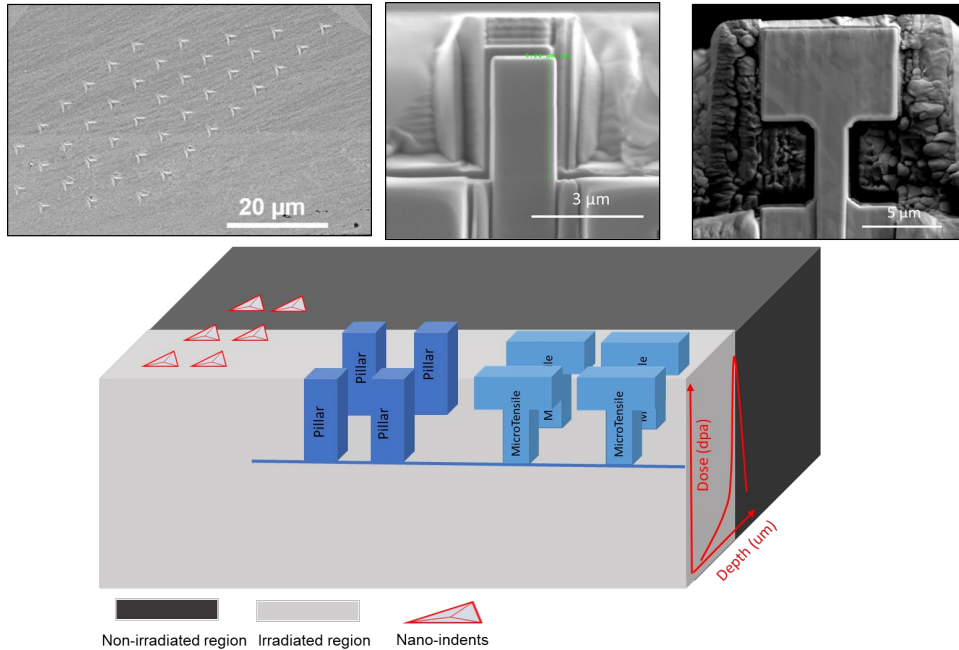
Figure 1-19. Schematic of an ion-irradiated sample with the different SSMT techniques including nanoindentation, micropillar, and microtensile testing

The second important advantage of SSMT is the ability to isolate specific microstructural features and select specific material parameters to evaluate their effects on the local deformation and failure mechanisms. For example, the effect of crystal orientation on the activation of different deformation behaviors as demonstrated in Figures 1.20A and BA in which activation of twinning is observed in one orientation but not the other. Furthermore, since microscale specimens can be made within the individual grains or multiple grains to include grain boundaries, we can isolate and assess individual deformation and failure mechanisms including strain localization and grain boundary failure. For instance, Figure 1.20C shows the selection of a specific grain boundary for microscale bicrystal tensile test. Coupled with electron backscatter diffraction (EBSD), information about the crystal orientations and grain boundary misorientations can fully identified before testing. Likewise, single grain microscale tests can be performed to study the influence of dislocation-defect interaction of individual defect type on strain localization and plasticity as a whole. Bi-crystal microscale specimens allow the investigation of dislocation and interface interaction as well as intergranular failure. The goal of the thesis is to demonstrate this versatility in examining the role of different defect types on individual grain and grain boundary behaviors.
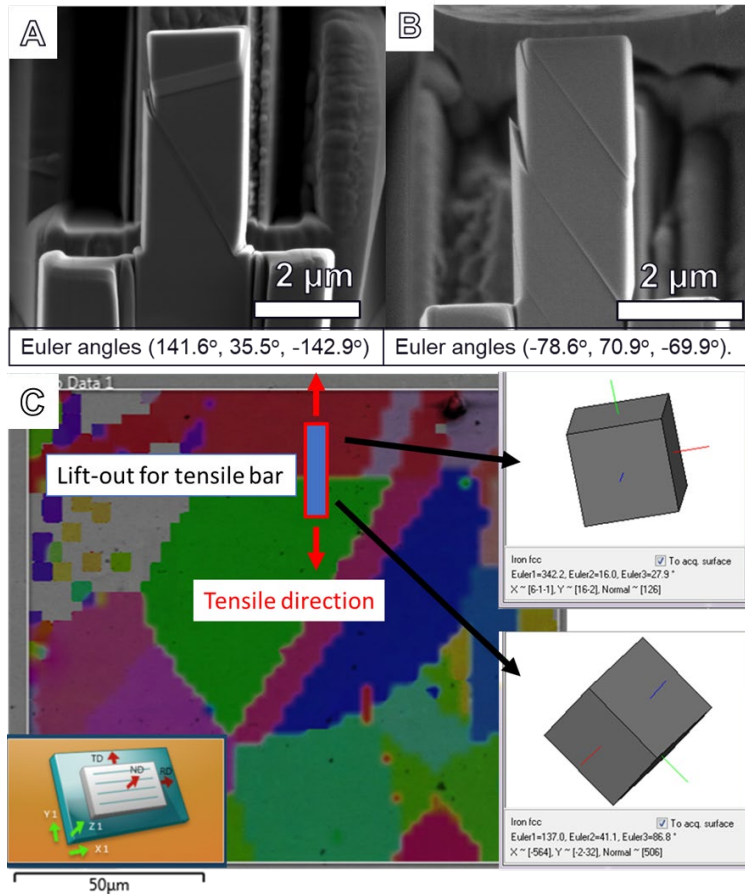
Figure 1-20 Micropillar compression testing of two showing A) deformation twinning and slip and B) slip. C) Electron backscatter diffraction map imposed on a scanning electron micrograph showing the selection of bicrystal tensile sample.

While SSMT offers significant advantages in studying microscale and nanoscale deformation mechanisms, size effect is an important issue that needs to be acknowledged and discussed before using these techniques to infer macroscopic behaviors. Numerous studies have established that the flow stress behavior is influenced strongly by the sample dimensions [94,96,104,105]. The theoretical size effect curves of well-anneal condition (containing very low defect density) and condition with a dense defect distribution are shown in Figure 1.21. In the well-annealed condition, the yield strength decreases the materials transition from polycrystal to single crystal because the effect grain boundary hardening is removed. In the single crystal regime, as the sample dimensions decrease, the yield strength of the material increases. This is because in the well-annealed condition, the dislocation source length is controlled by the size of the specimen. Since the stress required to operate the dislocation source is inversely proportional with the source length, the yield stress of the small scale specimen is inversely proportional with the dimension of the specimen. This regime is referred to as the size effect regime. The single-ended source model [106] has been proposed to calculate the change yield stress as a function of specimen size. As the sample dimension is reduced to hundreds and tens of nanometers, the materials enter the dislocation starvation regime, where the specimens are absent of dislocations

22

as the dislocations annihilate at the free surface. In this scenario, it requires a higher stress to nucleate dislocation from the free surface and the materials approach theoretical strength with decreasing sample dimensions. Because of the size effect, it is very challenging to obtain mechanical properties that are representative of the macroscale values. However, in the materials containing a dense distribution of defects (LRO precipitates, radiation-induced loops, voids), the size effect is significantly reduced [104]. In this case, the defect mean spacing is much smaller than that of the dimensions of the microscale specimens so the dislocation source length is controlled by the defect mean spacing instead of the sample dimensions. As the result, size effect is substantially reduced. The yield strength and the plastic flow behavior should therefore be representative of the macroscale single crystal values. For the thesis, the microscale specimens are appropriate as the different defect distributions are sufficient to minimize size effect.
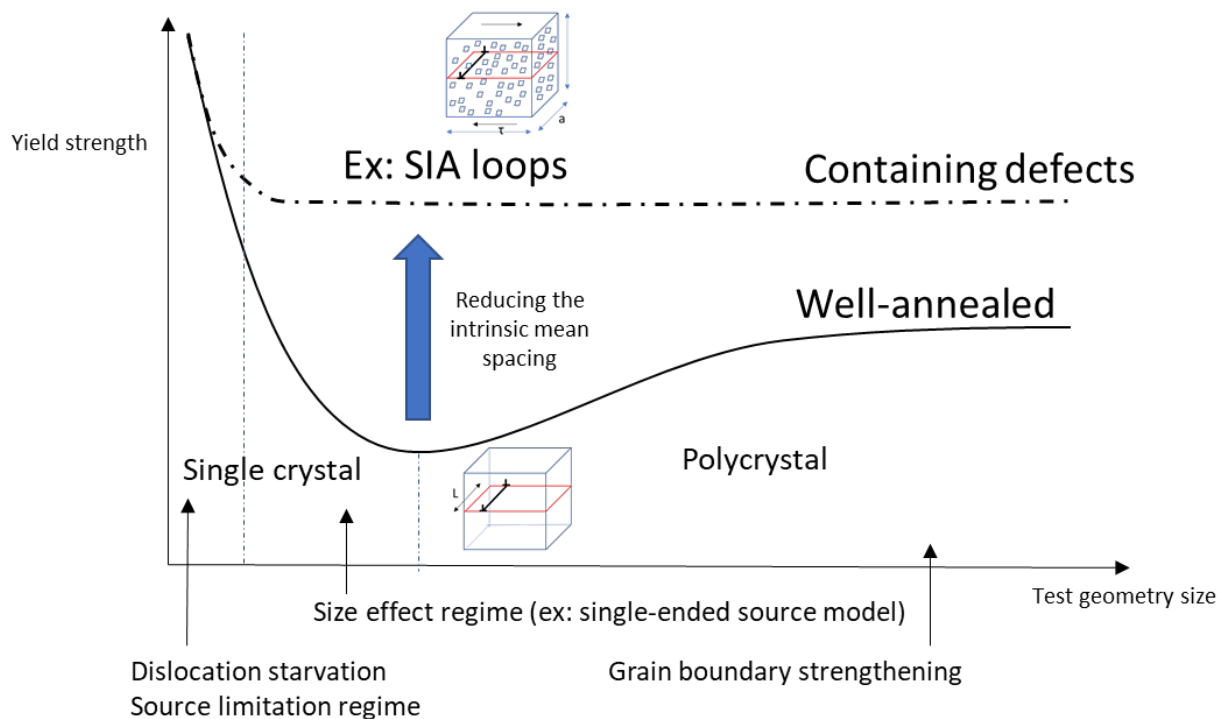
Figure 1-21 Theoretical size effect curves of the well-annealed condition and condition with a dense distribution of defects. The plot is replotted with permission from [81]

Chapter 2 – Thesis Scope and Objective

The motivation of the thesis is to develop and utilize small scale mechanical testing to investigate the influence of defects' mechanical stability on microscopic plasticity which in turn influences macroscopic deformation and failure relevant in nuclear reactor applications. In particular, the influence of defect stability on strain localization will be examined for different defect types including radiation-induced loops, LRO precipitates, voids, interfaces. Additionally, the effects of radiation damage (including void swelling, disordering and dissolution, radiation-enhanced precipitation, and radiation-induced loop accumulation) on various pre-existing defects in structural materials will investigated. Another smaller aspect of the thesis is to extend the capability of SSMT and develop microscale understanding beyond single grain deformation. Therefore, role of corrosion and radiation damage on grain boundary strength will be investigated using microscale bicrystal testing. Due to the breath of scope and wide variety of defects, different structural materials relevant for nuclear applications are studied. The contexts and material details are provided in each chapter. Schematic shown in Figure 2.1, provides a holistic picture of the scope of the thesis. The different defects are characterized into 0D, 1D, 2D, and 3D defects. The different defects are summarized as follows:

Strain Localization:

- Effect of interstitial nitrogen on radiation-induced microstructure evolution and change in mechanical properties – 0D defect
- Effect of radiation-induced loops on strain localization – 1D defect
- Effect of interface (coating and grain boundary) on plastic deformation and strain localization – 2D defect
- Effect of void on plastic deformation and strain localization – 3D defect
- Effect of Pt_2Mo-structured precipitates on plastic deformation – 3D defect
- Effect of $L1_2$- and DO_{22}-structured precipitates (before and after irradiation) on plastic deformation – 3D defect

Intergranular Failure:

- Effect of lath boundaries post irradiation on intergranular failure
- Effect of oxidized grain boundaries (exposed in PWR primary water condition) on intergranular failure
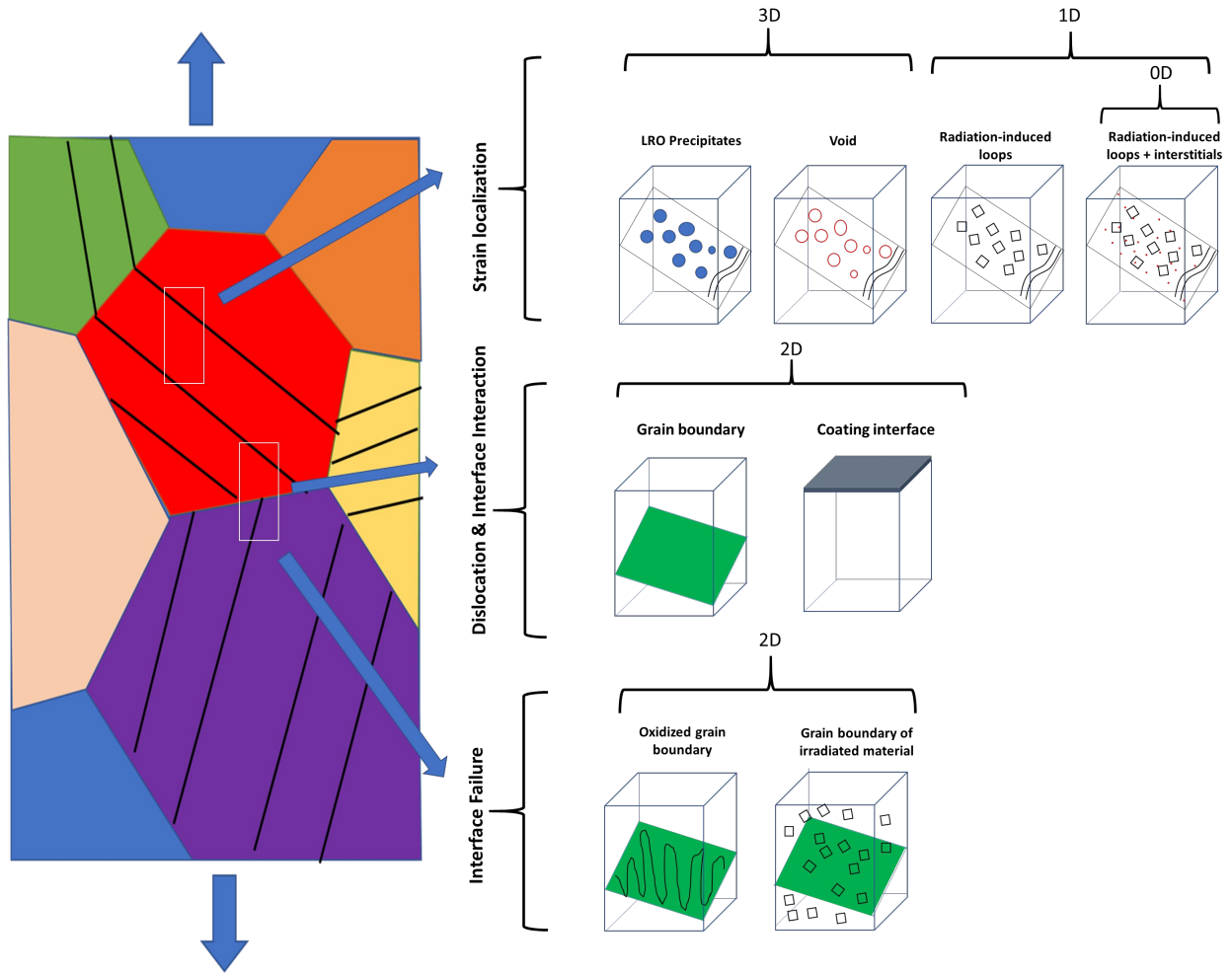
Figure 2-1. Schematic shows the different defect types being examined

3.1. Effect of Interstitial Nitrogen on the evolution of radiation-induced microstructure

3.1.1. Background

Cladding and fuel are exposed to the highest dose in a given reactor and therefore are expected to see significant changes depending on the type of reactor and material chosen [107]. One of the candidate materials for next generation of sodium cooled fast reactors' cladding tubes, which can demand radiation resistance up to hundreds of displacements-per-atom (dpa), is the tempered martensitic alloy HT-9 [21]. It is well documented that HT-9 and other tempered martensitic steels (TMS) exhibit strong resistance to void swelling [108–110]. Extensive mechanical test data, especially tensile properties, on irradiated HT-9 and other TMS have been published in the literature [21,111–113]. In particular, Maloy et. al. [21] reported an interesting observation from the tensile testing results of different tempered martensitic alloys irradiated to ~6.5 dpa in the Advanced Test Reactor, in which they suggest that there is a correlation between the post-irradiation ductility and the nitrogen concentration. The alloy with the lowest nitrogen concentration exhibits highest ductility after the irradiation. Similar trend was also reported in mild steels [20], in which higher nitrogen concentration increases the radiation-induced hardening. This effect has an important implication to the alloy design of next generation reactors; therefore, we have performed a systematic study on the influence of nitrogen content on the mechanical properties of a model alloy FeCr0.2C containing two different nitrogen concentrations.

3.1.2. Methods

Fe12Cr0.2C alloy, containing a low nitrogen content (0.001 wt%) and a high nitrogen content (0.035 wt.%), were provided by Los Alamos National Laboratory (LANL). The alloys were irradiated at the Ion Beam Materials Laboratory at LANL with 1.5 MeV protons at 300°C to the plateau dose regime of 1 dpa. Figure 3.1 displays the calculated Kinchin-Pease (K-P) DPA vs. depth profile of the irradiation condition. The dose profile is calculated from the SRIM software [114] with the threshold displacement energy of 40 eV. The temperature was monitored using a thermocouple on the sample directly. The average dose rate of the plateau dose regime is ~0.0215 dpa/hour.
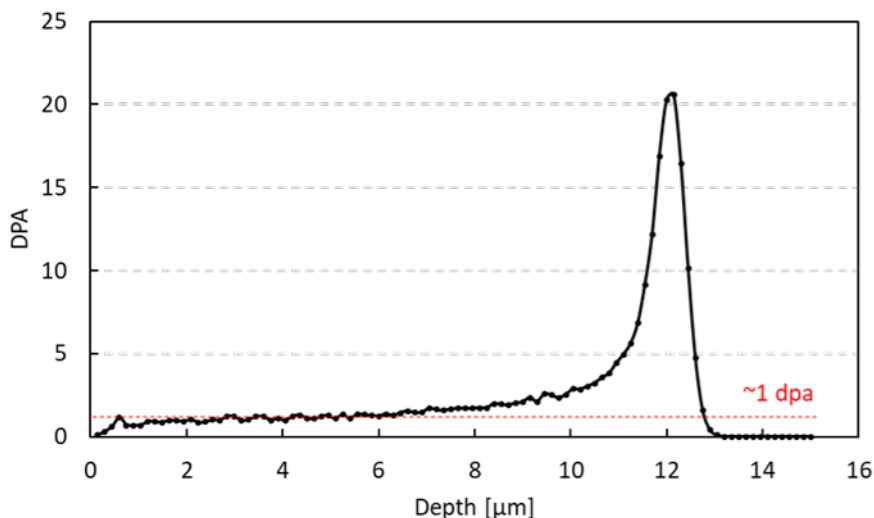
Figure 3-1 Dose versus depth profile

3.1.2.1. Transmission electron microscopy

TEM lamellae were fabricated using the FIB of the 1 dpa irradiated region of the high and low nitrogen samples. Bright-field (BF) TEM was performed to record the radiation-induced microstructures in the two nitrogen conditions. A FEI Tecnai F30, operated at accelerating voltage of 300 kV, were employed to record the microstructures. The work was previously performed at LANL and the results are included here to complement the mechanical testing results performed in our study.

3.1.2.2. Micropillar fabrication and testing

A gallium focused ion beam (FIB) was used to fabricate the micropillars. Rough milling was conducted at 30 keV with currents of 1-3 nA and the final cleaning was performed at 0.3 nA. The detailed fabrication procedure for microtensile bars using FIB is outlined in [103]. The aspect ratio (width:height) of the pillars is around 1:2. The width of the pillar is ~4 μm and the length of the pillar ~8 μm. The exact dimensions of each sample were measured using the SEM to calculate yield stress after testing. Ion channeling contrast imaging was used to reveal the microstructures of the samples. For the in situ SEM micropillar testing, the Hysitron PI-88 Picoindenter was utilized. The tests were performed in situ SEM under displacement control at a constant displacement rate of 10 nm/s.

3.1.3. Results and analysis
3.1.3.1. Radiation-induced microstructure of the high and low N conditions

Figure 3.2 shows the BF TEM images of the irradiated low nitrogen (Figure 3.2A) and irradiated high nitrogen (Figure 3.2B) conditions. Interestingly, in the low dose rate sample, the loops are smaller in size and higher in density compared to those observed in the high dose rate sample. The density and size of the loops are quantified for both conditions and shown in Table 3.1.
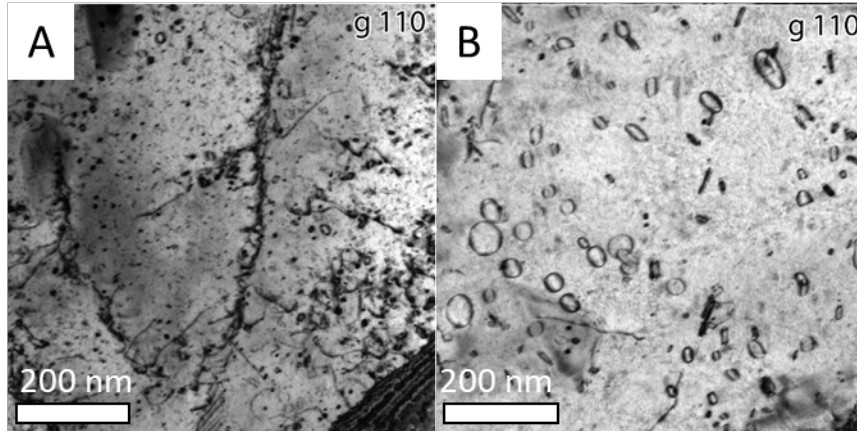
Figure 3-2 BF TEM images of the (A) irradiated low nitrogen and (B) irradiated high nitrogen

Table 3.1 Loop number density and the average size of the 1 dpa irradiated low N and high N conditions

Condition	Loop number density	Average size (nm)
Low N	6.16×10^{21} m^{-3}	7.2
High N	1.74×10^{21} m^{-3}	21.5

3.1.3.2. Micropillar compression

Three micropillars of the unirradiated-high N condition, one micropillar of the unirradiated-low N condition, three micropillars of the irradiated-high N, and two micropillars of the irradiated-low N conditions are tested. The stress-strain curves for all tests are shown in Figure 3.3. Figure 3.3A shows the stress-strain curves of the unirradiated condition and Figure 3.3B presents the stress-strain curves of the irradiated condition of the high and low nitrogen samples. The plastic flow is very stable and no strain burst is observed across all the tests. There are no major differences of the stress-strain curves between the low nitrogen and high nitrogen samples in both unirradiated and irradiated samples. There are non-neglectable variation in the plastic regime within each condition. The 1% yield strength values are extracted for all tests and plotted in Figure 3.4. In general, we observed an increase in YS after the irradiation in both N contents. Interestingly, the irradiated low N condition exhibits higher YS values as compared to the irradiated high N condition. Due to the limitation of the data collected, no meaningful statistics can be drawn at the moment.
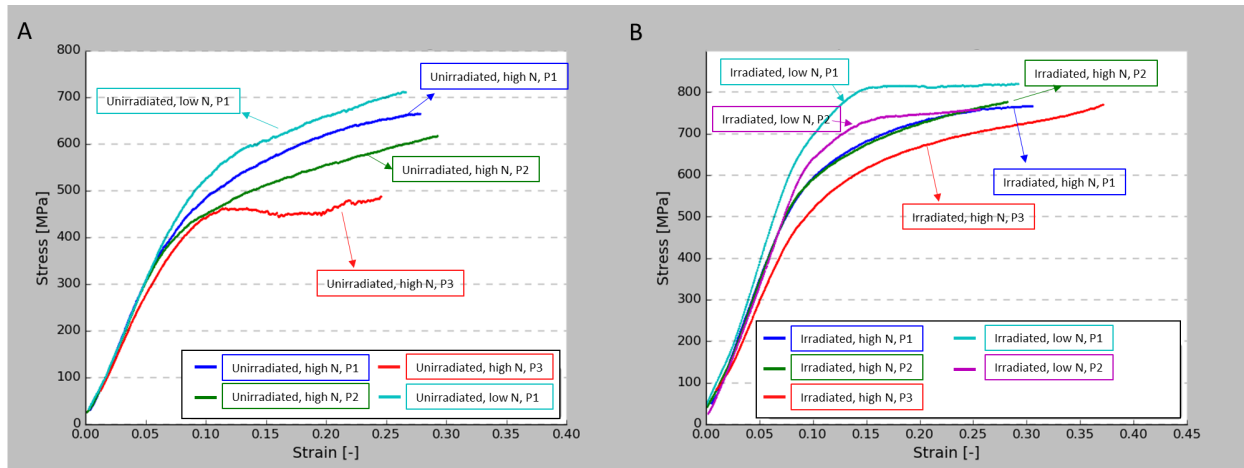
Figure 3-3. A) stress-strain curves of the unirradiated high N and low N conditions. B) stress-strain curves of the irradiated high N and low N conditions
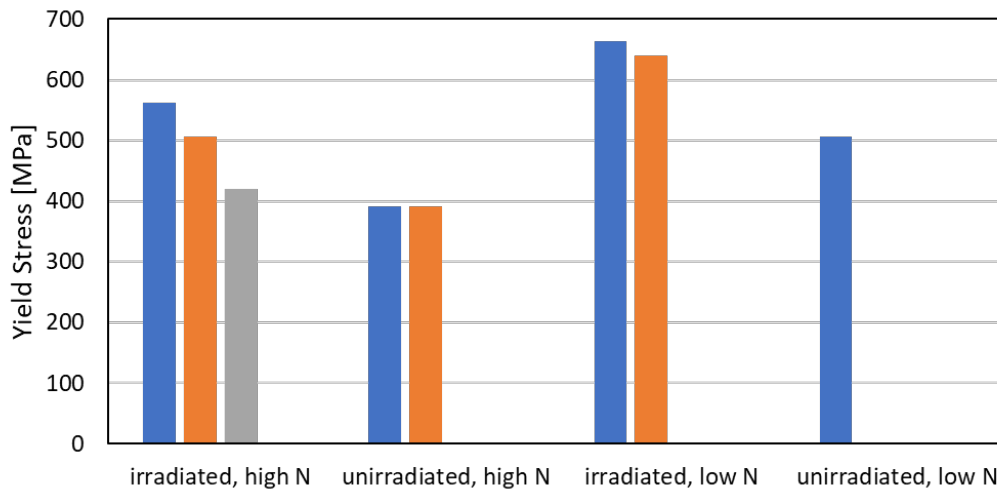
Figure 3-4 1% YS values of all tests performed

The stabilized plastic flow behavior in the irradiated conditions is interesting and usually not expected for irradiated micropillar tests [103]. However, the stable plastic flow behavior and the variation in the plastic regime can be explained by examining the microstructure of each micropillar. Figures 3.5 and 3.6 show FIB Images of the micropillars revealing the surface microstructures and the post-deformation SEM images of the unirradiated high N condition and irradiated high N. As seen in the FIB images of the micropillars, the pillars contain many boundaries (grain and lath); thus, the dislocations are piled-up and pinned by the interfaces. Dislocation avalanche process is significantly suppressed, leading to a stabilized plastic flow. The variation in the flow stress measured among the different tests within the same condition can be due to the difference in the morphology of the microstructure of each pillar. For instance, the different unirradiated high N pillars have very different microstructures in terms of the direction, spacing, and size of the grains within the pillars (as shown in Figure 3.5A). As a consequence, the post-deformation SEM images show that the slip behaviors are very different and strongly

resemble the original microstructures. Due to the small dimension of the micropillar, the microstructure being sampled varies from one pillar to the next; and this precise difference is reflected on the plastic flow regime.
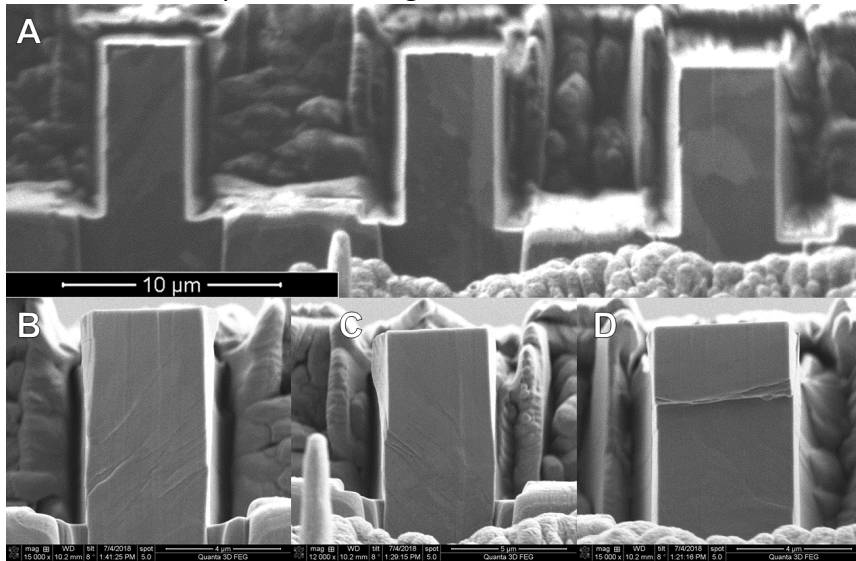
Figure 3-5. (A) FIB image of the unirradiated high N condition showing pillars 1-3 from left to right. Post-deformation SEM images of the unirradiated high N (B) pillar 1, (C) pillar 2, (D) pillar 3.
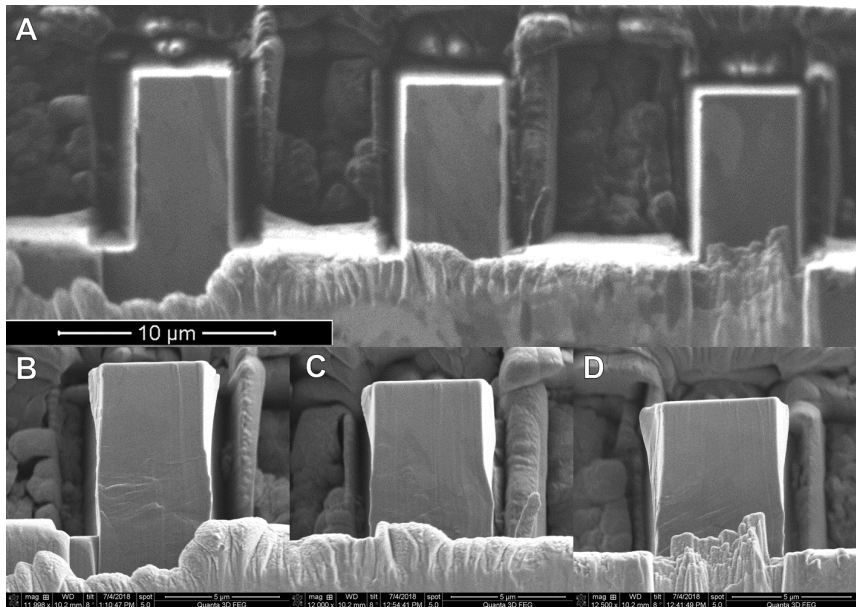
Figure 3-6 A) FIB image of the irradiated low N condition showing pillars 1-3 from left to right. Post-deformation SEM images of the irradiated low N B) pillar 1, C) pillar 2, D) pillar 3.

3.1.4. Discussion

The TEM results suggest that the free nitrogen atoms help stabilize the defect clusters and allow them to further grow in size of the SIA loops. In the high N condition, the loops are larger and lower in density as compared to the low N condition. When comparing the slip behavior via micropillar testing, the effect of N content is not observed. We believe that the effect of interfaces causing dislocation pile-ups are far more dominant compared to the effect of the nitrogen content so the difference in the plastic flow behavior is attributed to the variation in the pillars' microstructures. Interestingly, the yield stress of the irradiated low N condition is higher than that of the irradiated high N condition. If we assumed that the radiation-induced loops are the mainly responsible for the hardening, we can estimate the difference in the increase in hardening between the low N and high N conditions. The Dispersed Barrier Hardening model that gives the increase in shear strength, $\Delta\tau_{DPH}$ due to obstacles with a given number density N and average diameter D as :

$$\Delta\tau_{DPH} = \alpha_{DBH}\mu b\sqrt{ND}$$

Where α_{DBH}: hardening parameter depending on the defect strength, μ: shear modulus, b: Burger vector

The ratio between the hardening in the high nitrogen and the low nitrogen is given as:

$$\frac{\Delta\tau_{DPH,lowN}}{\Delta\tau_{DPH,highN}} = \frac{\alpha_{DBH,lowN}}{\alpha_{DBH,highN}}\sqrt{\frac{N_{lowN}D_{lowN}}{N_{highN}D_{highN}}}$$

If we assumed the hardening parameter is a constant (as it should be for a given defect type), using the number density and size information in Table 3.1, the hardening contribution from the radiation induced loops in the low N condition is about 8.8% more than that of the high N condition. Interestingly, micropillar data suggest that the hardening contribution difference should be higher (~40%). Due to limited statistics, no conclusion can be made; however, this large difference might suggest that other processes have taken place that decrease the strength of the defects in the high N content (e.q. decreasing $\alpha_{DBH,highN}$). The role of interstitial content on increasing strain localization is discussed in the thesis discussion chapter.

3.1.5. Future work

To gain further insight into the role of N content on the change in the mechanical properties and strain localization, we want to evaluate the effect of N after irradiation in pure single crystal iron materials. This allows us to isolate the effect of the nitrogen content from other effects such as grain boundary/ lath hardening, radiation-induced segregation, and radiation-induced precipitation. Furthermore, it will allow us to provide more valuable data for model calibration. Due to the effect of the Covid-19, we were not able to explore the irradiated single crystal with different N contents.

4.1. Radiation induced loops in 10 dpa proton-irradiated 304 stainless steel

4.1.1. Background

304 stainless steel (304SS) is widely used for the core internal components of light-water reactors due to its resistance against aqueous corrosion and availability at the time of deployment [11]. Research has shown that radiation damage significantly increases the flow stress and reduces the ductility, work hardenability, and toughness of 304SS [62]. This chapter presents some of the microscale tensile testing as well as microscale compression results performed previously on 304SS to show the mechanical stability of radiation-induced loops. I performed this work at UC Berkeley during my undergraduate study. Therefore, the full details of the work is presented in Ref [95,115]. Here, I present a quick summary of the finding on the mechanical stability of radiation-induced loops at the microscale. The inclusion of this summary is necessary to complete the theme/story of the thesis.

4.1.2. Methods

Two 304SS specimens were irradiated with protons to 10 dpa at a dose rate of ~8 x 10^{-6} dpa/s and a temperature of 360° ± 10°C by the Michigan Ion Beam Laboratory (MIBL) using a Tandetron accelerator. The fabrication of microtensiles was performed using a FEI Quanta 3D FEG dual beam FIB/SEM. A customized tensile gripper assembly was designed, manufactured, and attached to the Hysitron PI-85 Picoindenter system for the microtensile testing. The micropillar testing was performed ex situ using a nanoindenter. The full details of the fabrication and testing procedures are found in [95,115].

4.1.3. Result summary

Figure 4.1A compares the stress-strain curves of the irradiated and unirradiated tensile bars. The irradiated microtensiles show a significant reduction in total elongation (from ~47% to ~11%) and significant increase in YS (~213 MPa to ~438 MPa). The irradiated condition exhibits strong strain bursts as compared to the unirradiated condition.
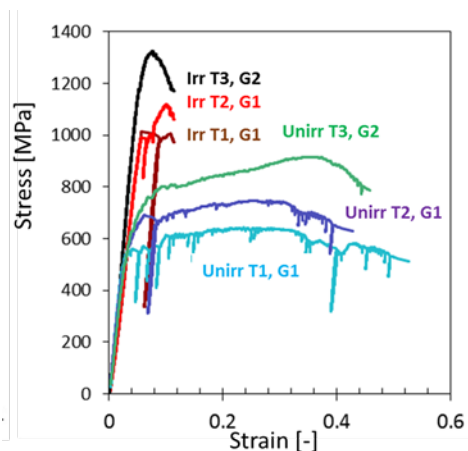
Figure 4-1 Stress-strain curves of unirradiated and as-irradiated tensile bars [95].

The post-deformation images are shown in Figure 4.2. The unirradiated condition (Figure 4.2.A) deformed via multiple slip bands as compared to the irradiated condition, where brittle behavior was observed (Figure 4.2B)
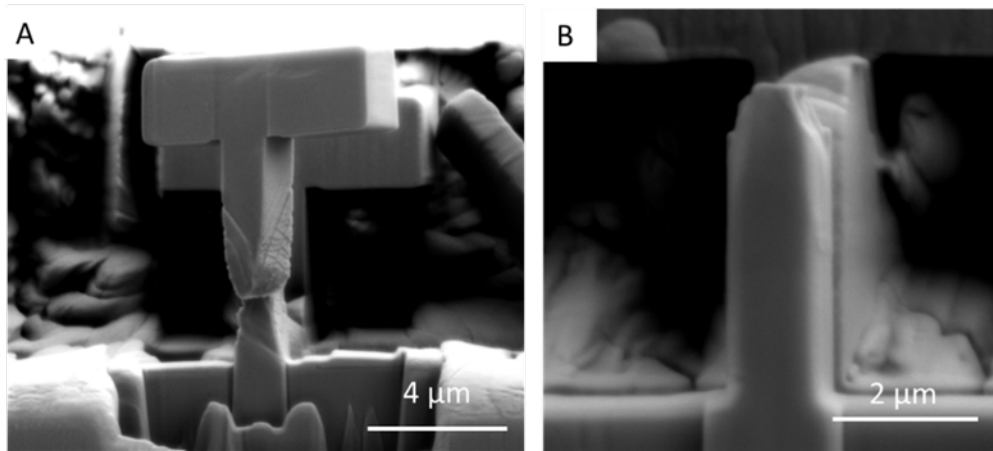
Figure 4-2 Comparison of deformation behavior among micro-tensile tests. (a) Many slip bands and significant necking are observed in an unirradiated tensile bar. (b) Brittle fracture surface of an as-irradiated tensile bar [95].

Figure 4.3 shows the ex-situ micropillar compression tests performed previously on the same 304SS specimens as a function of temperature from room temperature to 300 °C [116]. Consistent with the microtensile results, the unirradiated micropillars deformed via multiple slip steps (Figure 4.3A) and the irradiated micropillars deformed via localized slip (Figure 4.3B). Important to note that for both compression and tensile tests, the strain bursts (plastic instability) took place at low strain level. This suggests the low mechanical stability nature of radiation-induced loops, as explored via molecular dynamics in [77]. Figures 4.3C and 4.3D show the yield stress versus temperature and critical resolved shear stress (CRSS) versus temperature, respectively.
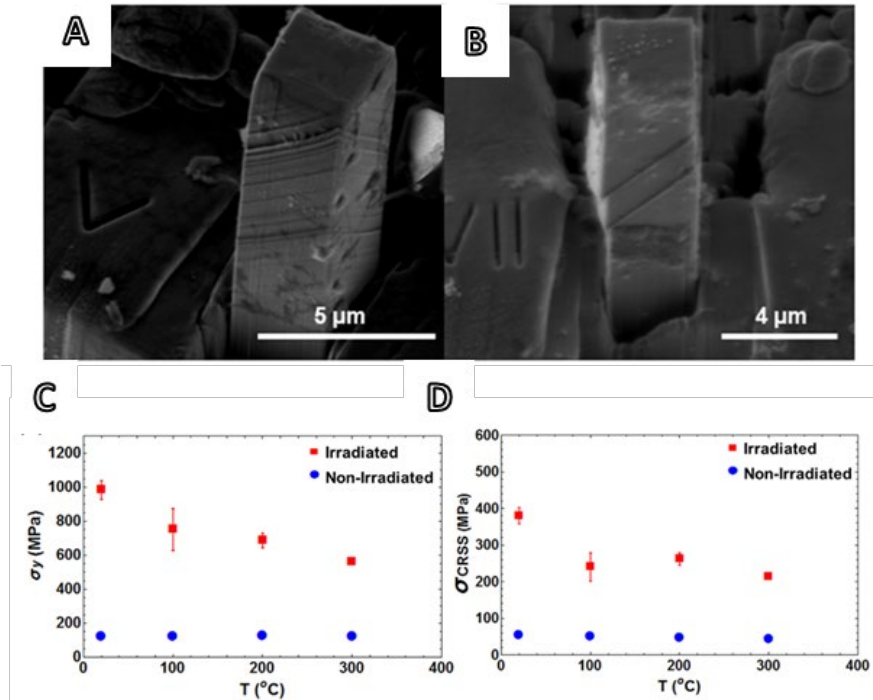
Figure 4-3. Microcompression properties of irradiated and non-irradiated 304 SS between RT and 300 °C. SEM images of a representative compressed. B) non-irradiated pillar and C) irradiated pillar at 100 °C. D) YS and E) CRSS versus temperature [115]

4.1.4. Conclusion

This brief summary of my previous work on 1D defect (radiation-induced loops in particular) applies microtensile and microcompression testing on ion-beam-irradiated 304SS to examine the role of radiation-induced loops on strain localization. Consistent with macroscopic and modeling results, the microscale single crystal tests show that the radiation-induced loops can be mechanically destabilized at low plastic strain level.

5.1 Unirradiated and Unoxidized Interface (Grain Boundaries and Coating Interface)

In this section, the role of hard interface (nontransparent to dislocation motions) with high interfacial strength on the microscale plastic deformation is investigated.

5.1.1 Background

While these SSMT studies [79–93] have extended our understanding of the complexity of the mechanical response at the nano-to-micron length scale, they have also raised various questions that must be addressed in order to expand the capability of SSMT for engineering applications. In particular, numerous experimental and theoretical studies have revealed that strain bursts or plastic intermittency, caused by dislocation avalanches, are characteristic of the plastic flow behavior of microscale and nanoscale crystals [79,96–98]. These dislocation avalanche processes effectively suppress dislocation multiplication and strain hardening in small single crystal tests; in contrast, the large sample volume of the macroscale polycrystalline and single crystal experiments prevents dislocation starvation and allow sufficient dislocation interactions for strain hardening [117]. Furthermore, macroscopic-like necking [117] is not observed in microscale samples. With the exception of nanocrystalline or nanostructured materials, SSMT almost exclusively samples single crystal properties, and thus measurements such as work hardening, total elongation, and ultimate tensile strength cannot be extrapolated to the bulk scale, hindering access plasticity related properties such as fracture mechanics on ductile materials at the small length scale. From the standpoint of the development of miniaturization of devices, strain bursts at the microscale can also lead to problems for the plastic forming of micro-size crystals [97]. Additionally, the plastic instability can increase the likelihood of sudden failure of miniaturized devices.

Recognizing the importance and the negative effects associated with strain busts, different research groups have investigated different strategies to suppress the strain burst behaviors [118–121] . The majority of these studies looks at the effect of passivation layers on thin films and microscale/nanoscale pillars. The common findings among these studies are that (1) the strain bursts can be suppressed by trapping dislocations using passivated layers, (2) the Bauschinger effect is present for passivated pillars and thin films, (3) the yield stress is higher for the passivated samples compared to the non-passivated samples. The major drawback of fully passivating the samples is that catastrophic failure, associated with large strain bursts, occurs when the passivated layer breaks during the deformation process [122] ; thus, it is not possible to suppress strain bursts in microscale tensile samples because the passivated layers (often an oxide layer or a ceramic coating) will break in tension loading. Additionally, fully coating the samples is problematic even when the coating does not break, for it impedes plastic deformation because the sample and the coating are in a parallel loading configuration (i.e. in order for the sample to plastically deform, the coated layer has to also deform to maintain geometric continuity).

This study proposes and validates a new experimental method to effectively suppress strain bursts in FCC nickel-based microtensile samples throughout the entire deformation

process until failure. Furthermore, we have developed a new conceptual framework to validate our new experimental methodology. In this work, we have uniquely incorporated the coupled effects of deformation by dislocation glide, crystal loading orientation, sample crystallinity, and sample dimensions into a single parameter, the blocked volume ratio (BVR), to describe the interfacial constraints on the plastic deformation behavior of FCC nickel-based microtensile samples. Our proposed framework aims to provide a new methodology to investigate the influence of interfacial constraints on microscale slip-dominated plastic deformation.

5.1.2. Blocked Volume Theory

In the case of FCC, there are 12 independent slip systems that can contribute to dislocation-mediated plasticity. Generally, a slip system is activated when its resolved shear stress (RSS) overcomes the critical resolved shear stress (CRSS) required to initiate dislocation motion. Schmid's law is used to calculate the resolved shear stress along any given slip system as the product between the uniaxial applied stress and the slip system's Schmid factor

$\tau_\alpha = \sigma_{applied} * m_\alpha$ Eq. 5.1

$m_\alpha = cos(\phi) * cos(\lambda)$ Eq. 5.2

Where τ_α : the resolved shear stress along slip system α, $\sigma_{applied}$: uniaxial applied stress, m_α : Schmid factor of slip system α, ϕ : the angle between the loading direction and normal vector of the slip system, λ : the angle between the load direction and slip direction of the slip system.

To quantify the degree of constraint due to an interface for a given slip system, the concept of the *"blocked volume"* is introduced. The blocked volume of a slip system is defined as the volume where the slip planes intersect the constraining surface, so the dislocations are effectively pinned by the constraining surface. A numerical method using Python Scipy library [123] is used to calculate the blocked volume of a given slip system. The method uses the Quickhull algorithm [124] to calculate the convex hull of the set of points belong in the blocked volume region. The method of introducing the set of points encapsulating the blocked volume region is detailed in section 5.1.3. The calculated convex hull of the set of points gives the volume of the blocked region.

The blocked volume ratio (BVR) is defined as the ratio between the blocked volume over the total volume of a given sample. Different from the previous studies, the interfacial constraints in our study are partial constraints, as shown in Figure 5.1, hence the need for the BVR parameter. The two requirements for the external constraints are that the interface must be impermeable to dislocations and it also must remain intact during the deformation process until failure. The both requirements can be satisfied by selecting a strongly adhering coating of a different material or a grain boundary with a low cumulative transmission coefficient [23]. In general, the cumulative transmission coefficient can be used to estimate whether the grain boundary is a strong barrier to dislocation motion [24].

For a given crystal orientation and sample dimension, the general BVR analysis of FCC single crystal is demonstrated in Figure 1 and outlined as follows:

36

- Calculate the Schmid factors of all 12 slip systems using Schmid's law.
- Determine the corresponding BVR values by quantifying the blocked volume of the 12 slip systems, as illustrated in Figure 1 and explained in the Method section.
- If the BVR value of the slip system(s) of the highest Schmid factors is low (< 0.5), then strain burst is expected to take place along those systems regardless of the BVR of the other slip systems. The influence of the BVR value on the degree of constraint is elaborated in Section 2.2.
- If the BVR value of the primary slip systems is high (> 0.5), then the BVR values of the other slip systems are considered. The sample is effectively constrained when the BVR values are high for all slip systems except for those of very low RSS values compared to the primary system(s), In other words, slip systems of very low RSS values are not expected to activate regardless of BVR values. For example, slip systems 4-6 have low BVR value of 0.191 and low Schmid factor values (0.127 and 0.253) so these slip systems are not expected to take place during the formation (Figure 1). The influence of the BVR value on the degree of constraint is elaborated in Section 5.1.2.

System	Slip Direction	Slip Plane	Schmid factor	BVR
1	$[\bar{1},1,0]$	(1,1,1)	0.014	0.988
2	$[\bar{1},0,1]$	(1,1,1)	0.099	0.988
3	$[0,\bar{1},1]$	(1,1,1)	0.084	0.988
4	$[\bar{1},1,0]$	$(1,1,\bar{1})$	0.127	0.191
5	$[1,0,1]$	$(1,1,\bar{1})$	0.127	0.191
6	$[0,1,1]$	$(1,1,\bar{1})$	0.253	0.191
7	$[1,1,0]$	$(1,\bar{1},1)$	0.211	0.957
8	$[\bar{1},0,1]$	$(1,\bar{1},1)$	0.296	0.957
9	$[0,1,1]$	$(1,\bar{1},1)$	0.084	0.957
10	$[1,1,0]$	$(\bar{1},1,1)$	0.352	0.805
11	$[1,0,1]$	$(\bar{1},1,1)$	0.070	0.805
12	$[0,\bar{1},1]$	$(\bar{1},1,1)$	0.422	0.805

Loading direction (Z-axis) : $[\bar{3},\bar{2},4]$
X-axis : $[\bar{2},3,0]$
Y-axis : $[\overline{12},\overline{8},\overline{13}]$
Representative Sample Dimension (unitless):
X-dimension = 1
Y-dimension = 1
Z-dimension = 1

Slip plane   Blocked volume   Free volume   Interface

Figure 5-1. A BVR analysis for a representative FCC sample at given crystal orientation and dimension. The blocked volume visualization of all slip planes is shown. The blocked volume indicates the region where the slip plane intersects the constraining interface. The method of denoting the blocked volume is shown in Section 5.1.3. In similar fashion, the free volume indicates the region where the slip plane does not intersect the constraining interface. The slip planes presented in the visualization are the slip planes that separate the free and the blocked volumes. The BVR values and Schmid factors of all slip systems are calculated.

5.1.3. Expected Influence of BVR on Dislocation-Mediated Plasticity in FCC metals

It is important to note at the outset that the following theory is developed for FCC single-crystal metals in which the major deformation mode is slip (i.e. deformation twinning is not considered.) By introducing the concept of the blocked volume, the single-crystal microtensile sample can be viewed as a bi-layer composite consisting of free and blocked volumes. Since the dislocation slip is constrained in the blocked volume while it is permitted in the free volume, the BVR value strongly influences the deformation behavior of the single crystal samples. Using this approach, a single-crystal-sample's flow behavior can be categorized into three distinctly different regimes. Figure 5.2 outlines the three deformation modes corresponding to the three BVR value regimes. In Figure 5.2A,B,C, the blocked and free volume regions are indicated by the blue and the yellow areas, respectively. As introduced in Section 5.1.1, the blue region is where the slip planes intersect the constraining interface and the yellow region is where the slip planes do not intersect the constraining interface. The construction of the blocked and free volumes is shown in Section 5.1.3. In the blocked volume region, dislocations are pinned by the interface so no slip is permitted. In the free volume region, dislocations can escape to the free surfaces so slip is permitted. The first deformation regime, active at low BVR, is termed "*discrete slip band failure mode*". The definition of the blocked volume guarantees that at a lower BVR, the active slip systems are relatively parallel to the constraining surface; therefore, the free volume and the blocked volume can be thought to be in a serial loading configuration, as shown in Figure 2A. This loading configuration implies that the free volume can deform by forming slip bands, independent from the blocked volume.

Increasing the BVR leads to the fact that the blocked volume is in a parallel loading configuration relative to the free volume, as seen in Figure 2B. This configuration is analogous to a bi-layer composite in parallel configuration. In this configuration, the free volume cannot deform independently from the blocked volume, and both have to accommodate the same strain in order to allow plastic deformation. Therefore, mixed mode deformation, characterized by simultaneous slip band formation in the free volume and necking behavior in the blocked volume, occurs in the parallel loading configuration. This deformation and failure regime at intermediate BVR is termed "*mixed mode*." A simple way to determine the loading configuration of the microtensile bar is if the boundary plane separating the free and blocked volumes intersects the base of the microtensile bar, then the sample is in a parallel loading configuration; otherwise, the sample is in a serial loading configuration. The transition between two loading configurations is expected to be around a BVR of 0.5, which is illustrated by the schematic of Figure 2B.

As the BVR of the active slip systems increase to a very high value, the tensile bar enters a mostly blocked configuration in which the blocked volume comprises the majority of the micro-tensile bar; thereby, only the blocked volume governs the deformation, as shown in Figure 2C. As a consequence, slip band formation is significantly suppressed. During the deformation process, the dislocations of the slip systems with the highest Schmid factor become mobile within the sample volumes, but they cannot escape the sample volume due to the constraining surface. As the stress increases, the other slip systems with sufficient RSS values also become active, leading to dislocation interaction among the different slip systems, which ultimately gives rise to strain hardening. After the work hardening stages, macroscopic-like necking is expected to set in,

leading to failure. This deformation and failure mode is termed "*necking and strain hardening mode*". The BVR value that marks the transition between "*mixed mode*" regime and "*necking and strain hardening mode*" regime is experimentally estimated in the Result section.
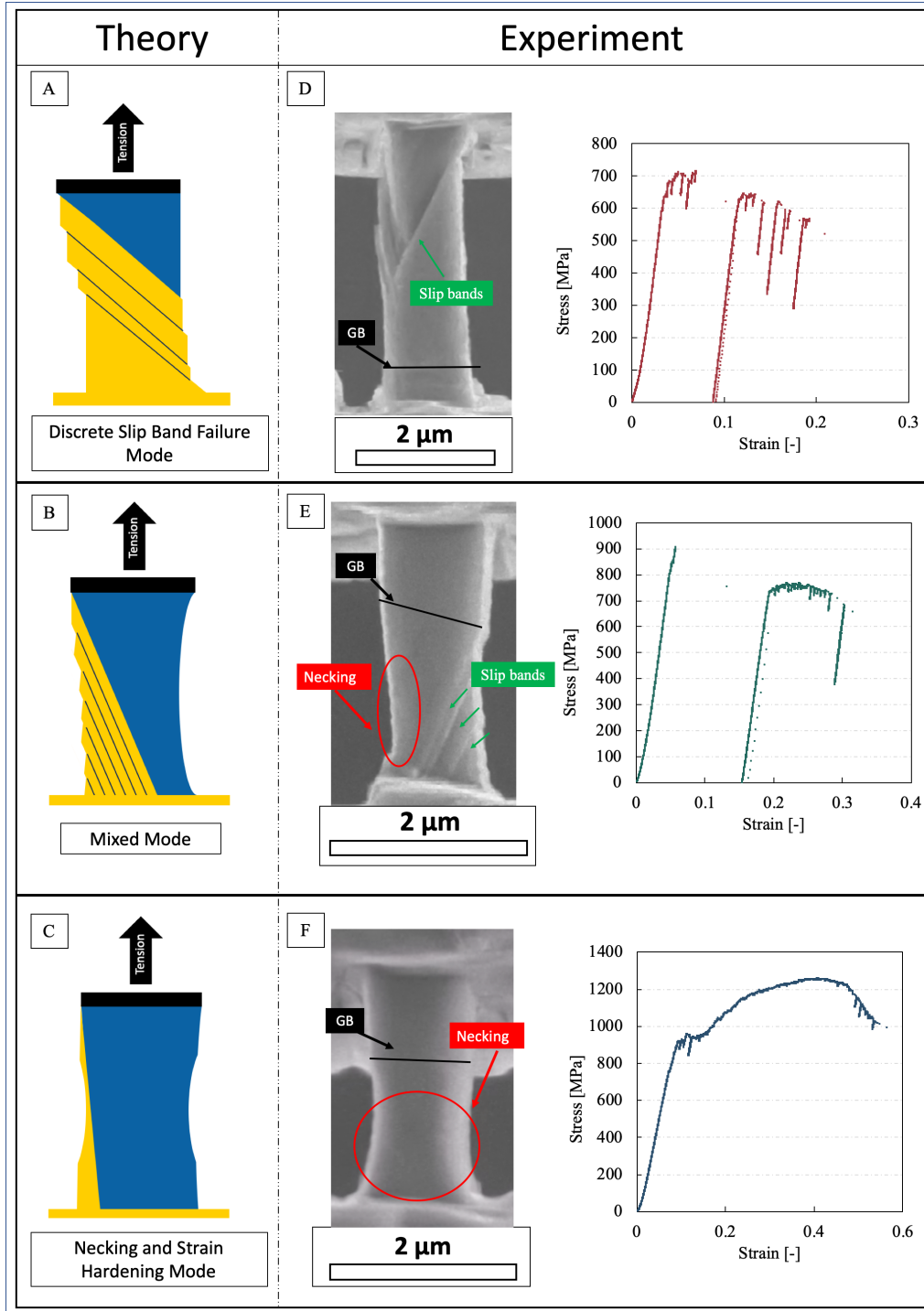
Figure 5-2. Schematics of (A) discrete slip band failure mode, (B) mixed mode, and (C) necking and strain hardening mode. Representative SEM images of the deformed samples and representative experimentally measured stress-strain curves measured experimentally are shown in (D) discrete slip band failure mode, (E) mixed mode, and (F) necking and strain hardening mode. The free (unblocked) and blocked volumes of the primary slip system are denoted by yellow shading and blue shading, respectively.

5.1.4. Methods
5.1.4.1. Material Preparation

Pure Ni and Ni-based Alloy 600 are selected in our study. Pure Ni samples (99.99% purity) were mechanically polished to S_a=50 nm. The hard coating was deposited using a cathodic arc deposition system (Kobelco AIPocket). Prior to the deposition samples were heated to 400 °C and then ion etched in order to remove surface contamination. A power of 3 kW was used on each of four targets (Ti:Al = 50:50) at -70 V of bias voltage and a deposition pressure of 4 Pa. Pure N_2 gas was used to produce a nitride coating. The deposition time was set to 45 min, which resulted in 4 μm thick coatings on Ni samples mounted on a double rotation stage. The deposited TiAlN coating exhibits cubic structure and 32 GPa hardness. Afterwards several 500 μm long areas on the sample's side were ion cleaned with FIB (Helios Nanolab 650) in order to expose large Ni grains at the coating-substrate interface. For Nickel-based alloy 600, three thermal histories of the same heat were evaluated: solution annealed (SA), solution annealed and thermally treated (SATT), and mill annealed and cold-forged (MACF). The heat was received from the supplier in the mill-annealed (MA) condition (heat treated at 927 °C for 3.5 hours, water-quenched) and was subsequently cold forged (CF) to 15% deformation to produce the MACF condition. To produce the SA condition, the MA material was solution annealed at 1100 °C for a 0.5 h, followed by a water quench. Further thermal treatment of the SA material at 704 °C for 12 hours with a subsequent air quench produced the SATT condition. The materials were part of a larger effort to study the issue of intergranular stress corrosion cracking (IGSCC) of Ni-base Alloy 600 in the primary water loop of pressurized water reactors. In this paper, only non-oxidized materials are discussed.

5.1.4.2. Microtensile Sample Fabrication

To understand the role of interfacial constraints on the plastic deformation behavior in FCC metals, we performed a series of microscale tensile tests as a function of the BVR parameter. Ni alloys with three distinct thermal treatments — solution-annealed (SA), solution-annealed thermally treated (SATT), and mill-annealed 15%-coldforged (MACF)— and pure Ni were tested with the constraining interface being grain boundaries and a ceramic coating, respectively. For ease of fabrication and testing, we used two different testing setups for the two constraint types.

A FEI Quanta 3D FEG SEM/FIB dual beam was utilized for the fabrication of microtensile specimens and for their subsequent testing. First, Electron Backscatter Diffraction (EBSD) was used to obtain crystal orientation information for grains of interest. The EBSD data allowed us to perform the BVR analysis in order to fabricate the microtensile samples with the desirable BVR. The microtensile tensile T-bone setup was used for the pure Ni samples with ceramic coating. The microtensile bars were fabricated using the focused Ga$^+$-ion beam according to the schematic

in Figure 5.3. The sample width dimensions were between 1-2 µm and the sample's dimensional aspect-ratio was chosen based on the selected BVR. The rough milling was conducted at 30 keV with currents of 1-3 nA, and the final cleaning was performed at 0.3 nA. The same fabrication procedure was reported in [125].
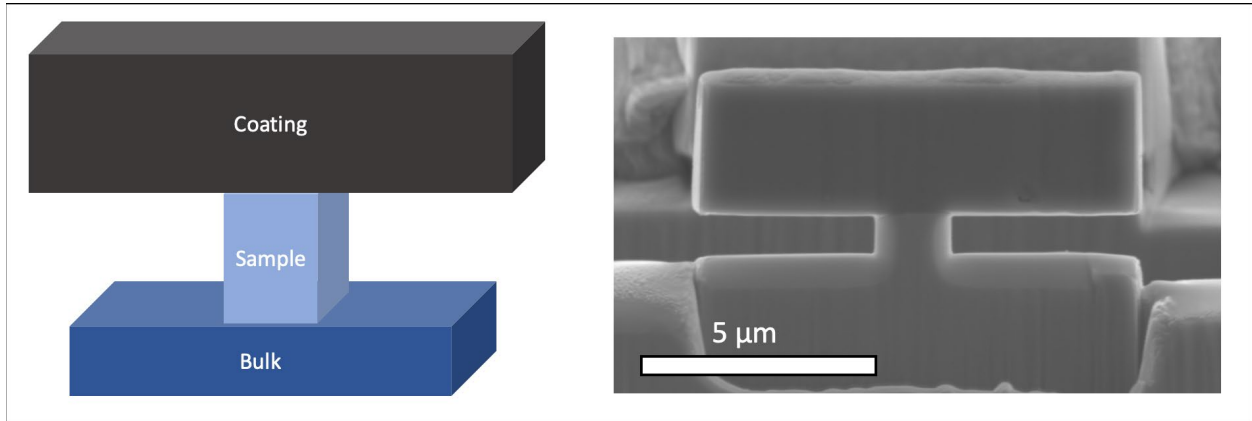
Figure 5-3. T-shape microtensile schematic and the SEM image of a representative tensile bar after fabrication.

A bicrystal tensile testing setup was used when a grain boundary was the constraining surface. Grain boundaries of low dislocation transmission probability were identified from the EBSD orientation map. The tensile bars containing such grain boundaries were then mounted on the Push-to-Pull device, manufactured by Bruker. Further thinning and cleaning of the tensile bar was done to obtain the final tensile dimensions, as shown in Figure 5.4. The detailed fabrication was reported in [126]. Since the grain of the lower BVR deforms while the other grain remains undeformed, the placement of the grain boundary in the tensile bar is carefully selected to obtain the desirable BVR values. Table 5.1 lists the grain boundary angles, the corresponding cumulative transmission coefficients (λ), and the BVR values of the individual grains of the bicrystal samples. The λ values are calculated using the formulation proposed in [24]. A λ value of 12 means that the grain boundary is transparent to dislocation motion and a λ value of 0 means that the grain boundary is a perfect barrier.
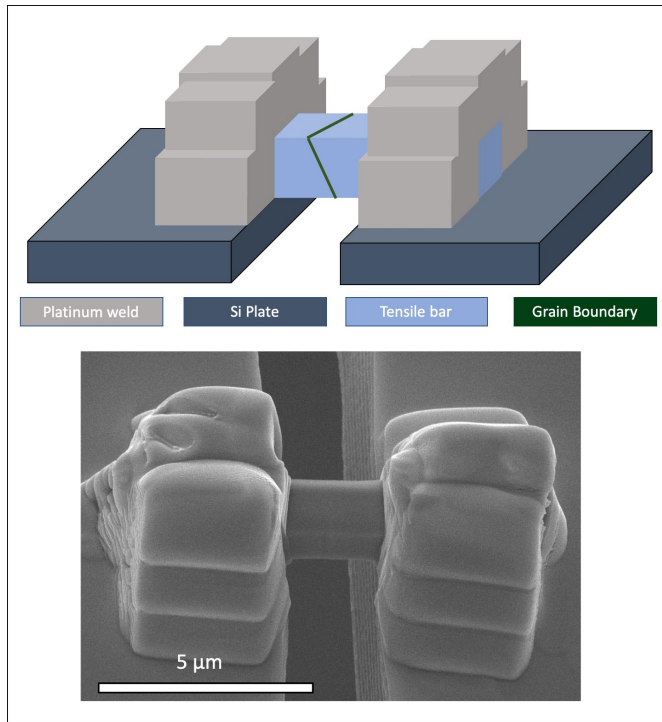
Figure 5-4. Bicrystal microscale tensile schematic and the SEM image of a representative tensile bar after fabrication.

Table 5.1. The misorientation angles, cumulative transmission coefficients λ, BVR values of the grains, and observed deformed grains.

Samples	Misorientation Angle (°)	λ	Grain 1 BVR	Grain 2 BVR	Deformed Grain
Ni Alloy, SA 1	59.7	2.951	0.0285	0.917	Grain 1
Ni Alloy, SA 2	54.4	0.641	0.808	0.666	Grain 2
Ni Alloy, SA 3	59.7	2.682	0.8334	0.776	Grain 2
Ni Alloy, SATT 1	42.1	1.027	0.218	0.95	Grain 1
Ni Alloy, SATT 2	43	0	0.932	0.841	Grain 2
Ni Alloy, MACF 1	48.2	1.087	0.667	0.298	Grain 2
Ni Alloy, MACF 2	38	0	0.921	0.867	Grain 2

Tensile tests were performed *in situ* in the SEM (Quanta 3D FEG) using the PI-88 Picoindenter, purchased from Bruker. The tests were conducted at a constant displacement rate of 10 nm/s, and the tensile bars were tested to failure.

5.1.4.3. Blocked Volume Calculation

While there are several ways to calculate the blocked volume, we present a simple yet versatile method. Given a list of vertex points defining the constraining surface and a 3D volume defined by a list of planar surfaces $[s_1, s_2, \ldots]$, where each planar surface is a list of points defining the vertices of the surface $s_i = [(x_0, y_0, z_0), (x_1, y_1, z_1), \ldots]$, the blocked volume is calculated by finding the set of points on the blocked volume and calculating the convex hull volume of those points. For each surface s_i, a grid of points G_i on the surface is calculated (Figure 5.5A). For a point p_i on the grid G_i, a slip plane L_i of the given slip system is defined by the tuple (p_i, v_n), where v_n is the normal vector of the slip plane (Figure 5.5B). If the plane L_i intersects the constraining surface, point p_i can be classified as "blocked" as it belongs to the blocked volume. The procedure is repeated for all points on all the free surfaces of the sample (Figure 5.5C). The convex hull volume of the set of these blocked points is the blocked volume for the slip system (Figure 5.5D). The developed method can also be applied to samples of cylindrical shapes.
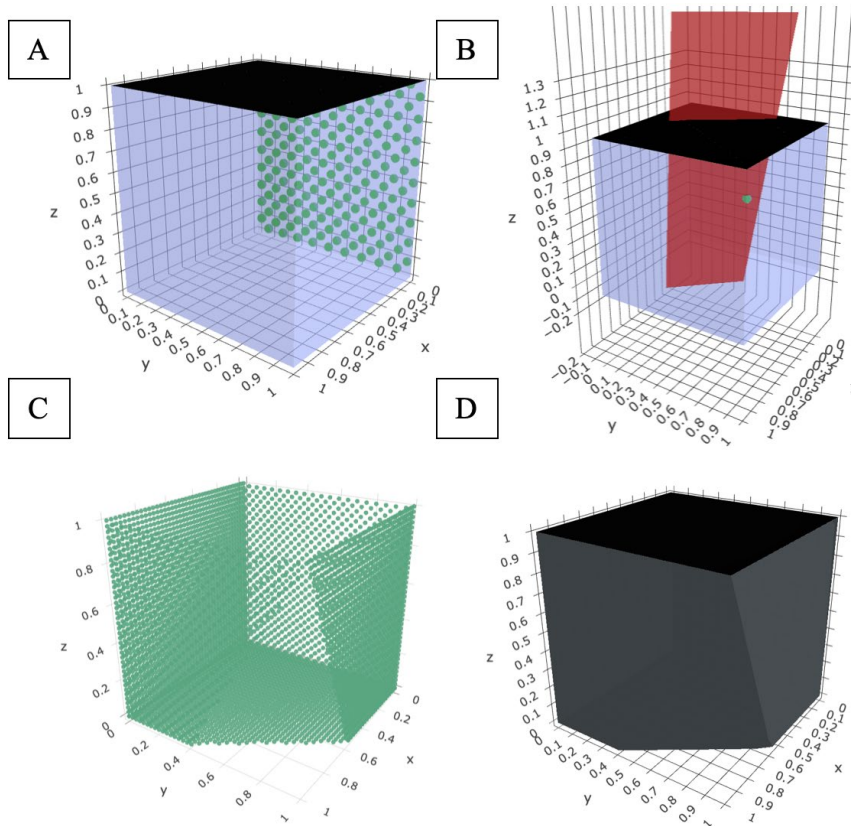
Figure 5-5. Visualization of the blocked volume calculation of the slip systems with slip plane $(1, \bar{1}, 1)$ from Figure 1. A) A grid of points G_i (green circles) is calculated for each free surface s_i. B) For a point p_i (green circle) on the grid G_i, a slip plane L_i of the given slip plane (red plane) is defined by the tuple (p_i, v_n), where v_n is the normal vector of the slip plane. If the plane L_i intersects the constraining surface (black plane), point p_i is classified as "blocked" as it belongs to the blocked volume. C) The procedure is repeated for all points on all the free surfaces of the sample to generate a full set of "blocked" points (green circles) on the free surfaces. D) The convex

hull volume of the set of these blocked points is the blocked volume for the slip system (gray volume).

5.1.5. Results and Analysis
5.1.5.1. Experimental Validation for the FCC case

In order to correctly calculate the BVR value of each sample, the crystal orientation of the sample is selected such that the BVR value of the primary slip systems(s) is the lowest compared to all other slip systems with the exception of the very low RSS slip systems to ensure that the BVR of the primary slip system(s) is the limiting BVR value. An example of a sample with such crystal orientation is shown in Figure 5.1.

At low BVR values, "*discrete slip band failure mode*" was observed, as shown in Figure 5.2D. The deformation video shows that the representative tensile bar of low BVR deforms by forming multiple bands until failure. The representative stress-strain curve (Figure 5.2D) shows multiple strain burst events, indicated by the large stain jumps, and no presence of work hardening after yielding. At intermediate BVR values, the tensile bars show "*mixed mode*" during deformation until failure, as shown in Figure 2E. During the deformation, slip bands formed in the free volume while necking took place in the blocked volume. The representative stress-strain curve (Figure 5.2E) shows a large strain jump, corresponding to simultaneous slip band formation and necking in the free and blocked volumes, respectively. At the very high BVR values, the tensile bars deform uniformly, followed by necking until failure, as shown in Figure 5.2F. The representative stress-strain curve of a high BVR test (Figure 5.2F) shows significant strain hardening and strong suppression of strain bursts in the stress-strain curve.

The deformation failure modes of all the tests are plotted against the BVR of the primary slip system(s) as shown in Figure 6. "*Mixed* mode" was observed for intermediate BVR values (0.67 and 0.78). At BVR values above 0.81, "*necking and strain hardening mode*" mode was observed. Experimentally, we set the estimate of the transition BVR value from "*mixed mode*" mode to "*necking and strain hardening mode*" to be 0.81 as it is the lowest BVR value measured here which shows "*necking and strain hardening mode.*" However, one expects variabilities with the effectiveness of different constraint types for blocking slip. Also, it is important to note that there remain uncertainties associated with the measurements of the sample dimension and the crystal orientation, which affect the BVR calculation. Because of these uncertainties, the key takeaway from Figure 5.6 is that macroscopic deformation and failure mode can be obtained in FCC micro-tensile samples when the BVR values of the active slip systems are high.
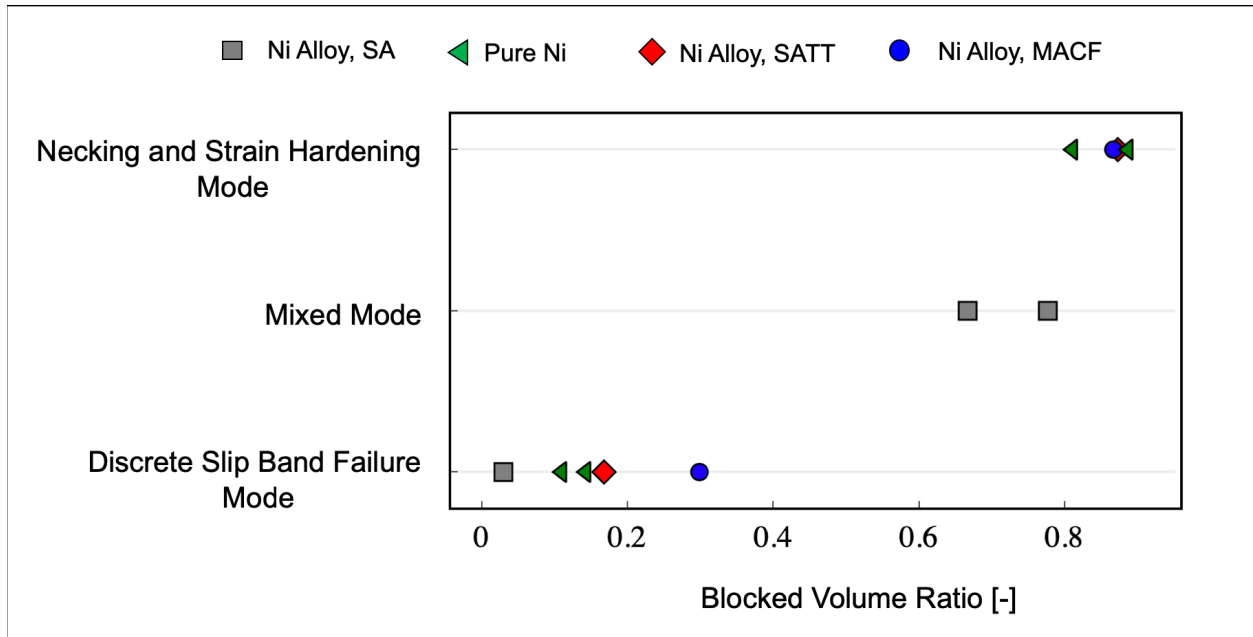
Figure 5-6. The deformation mode plotted versus the BVR of the primary slip systems

The experiments also demonstrated the flexibility of constraint type required to achieve macroscopic deformation. Figure 5.7 shows that the "*necking and strain hardening mode*" was observed in both microtensile testing of a T-shape tensile bar (Figure 5.7A) and a bicrystal tensile bars (Figure 75.B) with the constraining interfaces to be the coating interface and grain boundary, respectively.
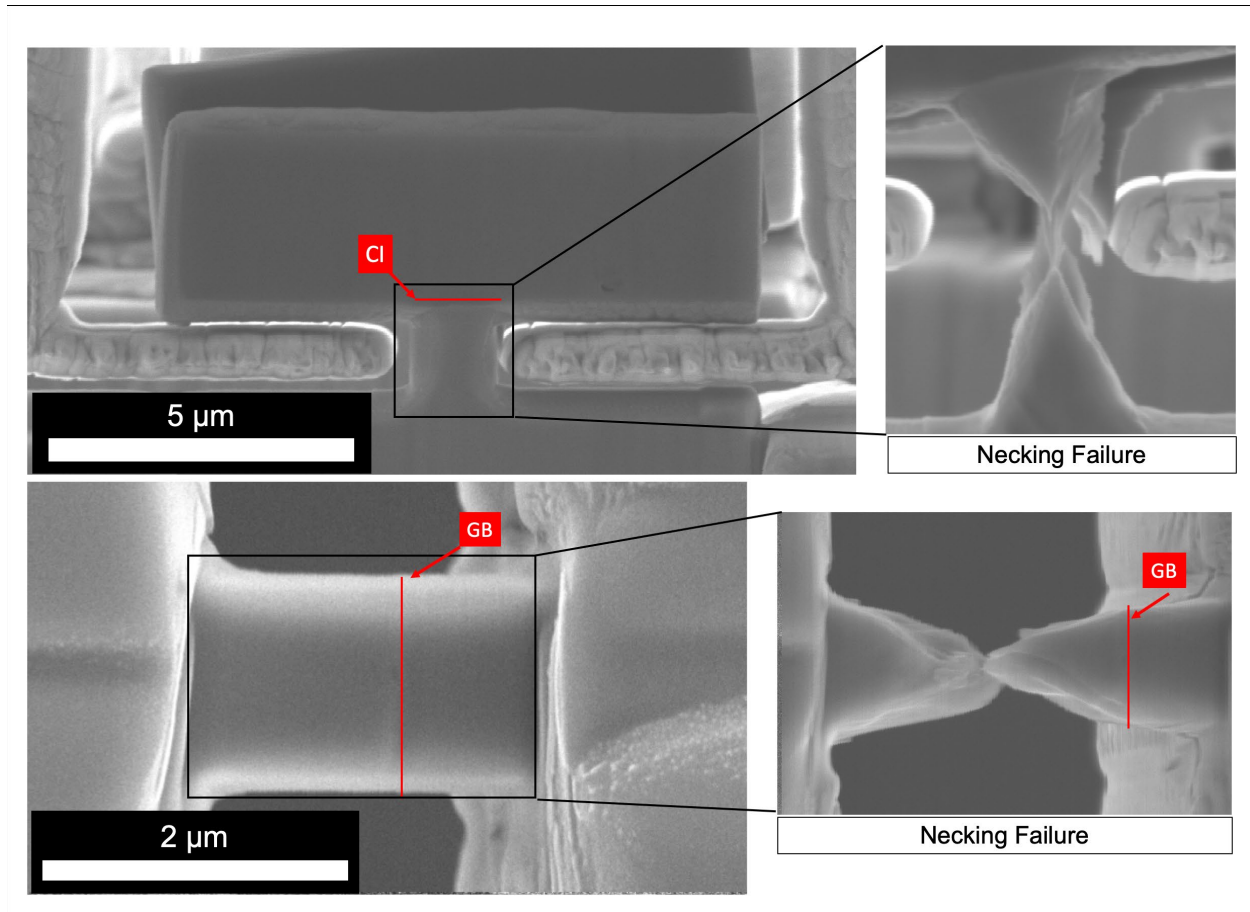
Figure 5-7. SEM images showing "necking and strain hardening mode" was observed for (A) the T-shape tensile testing setup and (B) the bicrystal tensile testing setup with the constraining interfaces being a coating interface (CI) and grain boundary (GB), respectively.

5.1.6. Study Discussion

Since the BVR of a sample depends on the crystal orientation and the height-to-width aspect ratio, the developed geometric criteria can be applied to create prediction maps for slip-dominated plastic deformation behavior in FCC crystals as a function of crystal orientation and aspect ratio. To demonstrate the usefulness of such a map, the multi-slip loading orientations – [001], [011], and [111] – are selected. Figure 5.8A, 5.8B, and 5.8C show the BVR considering a rectangular pillar in a FCC metal, whose top surface is the constraining surface, and the normal orientations of that top surface are taken to be [001], [110], and [111] respectively (determined by Euler angles ϕ_2 and Φ), over a range of Euler angle ϕ_1 ($0^o - 90^o$) and height-to-width aspect ratio ($0.5 - 5$). The different deformation regimes ("*discrete slip band failure mode*", "*mixed mode*", and "*necking and strain hardening mode*") vary drastically for the three normal orientations. The color coding represents the lowest BVR values of the active slip systems for a given aspect ratio and crystal orientation. This type of mapping informs us about the potential influence of an interfacial interface on the plastic deformation behavior for any given crystal orientation and an aspect ratio. As shown in the figure, the microtensile samples of the crystal orientations and aspect ratios in the red and dark red regions (BVR > 0.811) are expected to

undergo "*necking and strain hardening*" mode with mostly suppressed strain burst behavior. For the region whose BVR is below 0.5, "*discrete slip band formation*" mode and strain burst behaviors are expected. For FCC system whose major deformation mode is slip, the maps can inform on the expected deformation behavior in presence of an interfacial constraint. Additionally, compared to the previous studies [127–129], the BVR mapping over crystal orientations offers a new perspective on the influence of aspect ratio on the deformation behavior of the microscale experiments
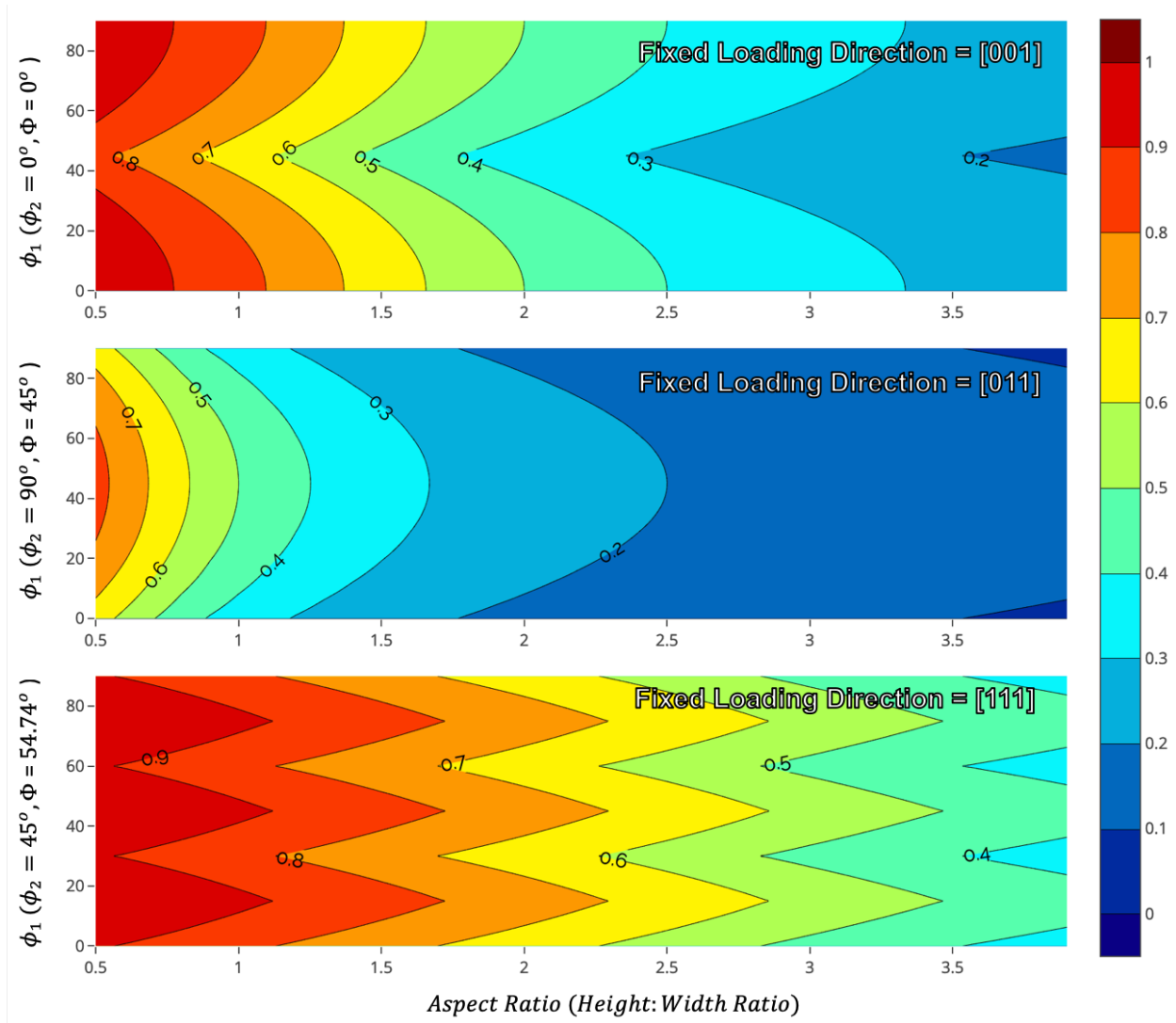
Figure 5-8. Mapping of the blocked volume ratio of FCC rectangular pillars for A) [001], B) [011], and C) [111] normal loading orientations over a range of Euler angle ϕ_1 ($0^o - 90^o$) and height-to-width aspect ratio (0.5 − 4). The color coding represents the lowest BVR values of the active slip systems for a given aspect ratio and crystal orientation.

Furthermore, the proposed theory motivates two research directions that deserve further exploration. The first direction is to examine whether the "necking and strain hardening"

mode of high BVR samples is comparable with the plastic deformation of the same crystals at the macroscale. If it can be shown to be comparable with that of macroscopic deformation, it would enable the ability to locally probe the macroscopic-like properties of individually build layers and identify the weak spots in additively manufactured metals and other advanced alloy designs across multiple disciplines. In addition, the nuclear industry can lower the cost of testing and reduce dose concerns by using microscale samples to obtain measurements that are relevant to large neutron-irradiated structural components as well as micrometer-thick ion-irradiated layers. However, several questions need to be addressed before we can realize this potential. Notably, the microstructural evolution and the dislocation density evolution between the microscale and macroscale tests must be compared. For instance, it is known that single crystal Ni forms dislocation cell structure [130] during macroscopic uniaxial testing. Therefore, one can see if the high BVR pure Ni samples would also form dislocation cell structure during microscale tensile testing. The second research direction is to use the proposed theory to enable future quantitative studies on grain boundaries and interfaces using small-scale testing. Important interfacial failure modes in alloys such as stress corrosion cracking [131], helium embrittlement [12], and hydrogen embrittlement [132] could be investigated and observed directly. One strategy is to manufacture microscale bicrystal tensile samples in which both grains have very high BVR values in order to suppress early plastic deformation of the matrix and encourage grain boundary failure.

5.1.6. Conclusion and future work

The study investigated the influence of interfacial constraint on the dislocation-mediated plasticity of FCC crystals in microscale tensile tests. We have introduced a simple yet effective parameter, BVR (blocked volume ratio), to quantify the degree of constraint for a given slip system due to an interface. Experimentally, we have shown that the plastic flow behavior is highly dependent on the BVR of the sample. Under the proposed framework, other important parameters (e.g. other slip systems, stacking fault energy, propensity for slip, dislocation cross-slip, and strain rate) can be investigated to explore new phenomena and complexity. In our view, the BVR map provides a new and useful framework to understand and predict the active plastic deformation mode in microscopic samples. Additionally, the study provides future research directions which are important in further maturing SSMT. First, it introduces a new opportunity for research in extracting representative macroscopic properties of site-specific microstructural features of materials. Secondly, the blocked volume concept can be utilized to encourage interfacial failure by suppressing "discrete slip band failure mode" in the material adjacent to the interface. Therefore, it enables a direct examination of interfacial strength, such as grain boundaries, at the microscale. Important interfacial failure modes in alloys such as stress corrosion cracking, helium embrittlement, and hydrogen embrittlement can then be investigated through small scale testing. Furthermore, the study provides a new framework to understand the influence on hard (impenetrable) interfaces in dislocation motion and strain localization at the microscale. We see that the high BVR or highly constrained condition effectively suppresses strain burst (plastic instability) and allows for work hardening and necking-like failure at the microscale. Another insight is the microscale plasticity is highly dependent on interfacial constraint. For future work, it is of interest to investigate the effect of interfacial constraint on ion-irradiated

materials. It would be interesting to see how dislocation free channels interact with hard interfaces such as protective coating and non-transparent interfaces.

5.2 Effect of Irradiation and Corrosion on Interface Strength and Failure

In this section, the role of compromised interfaces (oxidized and irradiated) on plastic deformation is investigated.

5.2.1. The Effects of Martensitic Laths and Radiation Damage on the Deformation Behavior of a HT-9 Alloy using Microtensile Testing

5.2.1.1. Background

While the radiation effects on the bulk mechanical properties in Ferritic/Martensitic (F/M) steels have been extensively studied, there have not been direct observations or measurements on radiation effects on the strength of the martensitic boundaries. Given the high volume fraction and the important role of martensitic boundaries in trapping point defects during the irradiation, it is important to explore the deformation and failure behaviors of those boundaries in the presence of irradiation damage.

To probe particular martensitic boundaries, we utilized small scale mechanical testing (SSMT) via *in situ* scanning electron microscopy (SEM) microtensile testing. In this study, we utilized *in situ* SEM microscale tensile testing to assess the influence of microstructures on the deformation behaviors of a HT-9 alloy in unirradiated and 1 dpa proton-irradiated conditions.

5.2.1.2. Methods
5.2.1.2.1. Materials Preparation

To complement and compare to recent research on the effects of neutron irradiation in HT-9 on mechanical properties, we selected the HT9 material of the heat 84425 that was also used in ACO-3 duct [133]. The HT-9 heat has the composition of Fe-11.8Cr-0.2C-0.2Si-0.5Mn-0.5W-0.3V-1.0Mn-0.5Ni. The material underwent a heat treatment of normalizing at 1065 °C for 0.5 h/air cooling followed by tempering at 750 °C for 1 h/air cooling [107]. The HT-9 material was irradiated with 1.5 MeV protons at 300 °C to achieve the plateau dose regime of 1 dpa at the Ion Beam Materials Laboratory at Los Alamos National Laboratory. Although the 1 dpa dose is very low compared to the target dose in which HT9 alloys are designed to achieve in the nuclear reactors, it introduces a considerable accumulation of irradiation-induced defects (interstitial and vacancy loops in particular) at low temperatures, which strongly influence the hardening response of HT9 and other TMS alloys. Due to the limitation of irradiation time, 1 dpa was used to provide a comparative assessment of the mechanical response of grain boundaries influenced primarily by radiation-induced hardening. The selected dose in this study is also consistent with previous literature studying proton irradiation in HT9 and T91 alloys [134,135].

Figure 9A displays the calculated Kinchin-Pease (K-P) DPA vs. depth profile of the irradiation condition. The dose profile is calculated from the SRIM software [114] with the threshold displacement energy of 40 eV. The temperature was monitored using a thermocouple on the sample directly. The average dose rate of the plateau dose regime is ~0.0215 dpa/hour. The four

microtensiles (two microtensiles in each condition) were then fabricated in the unirradiated and the 1 dpa plateau dose regime. The schematic of the sample is shown in Figure 9B.
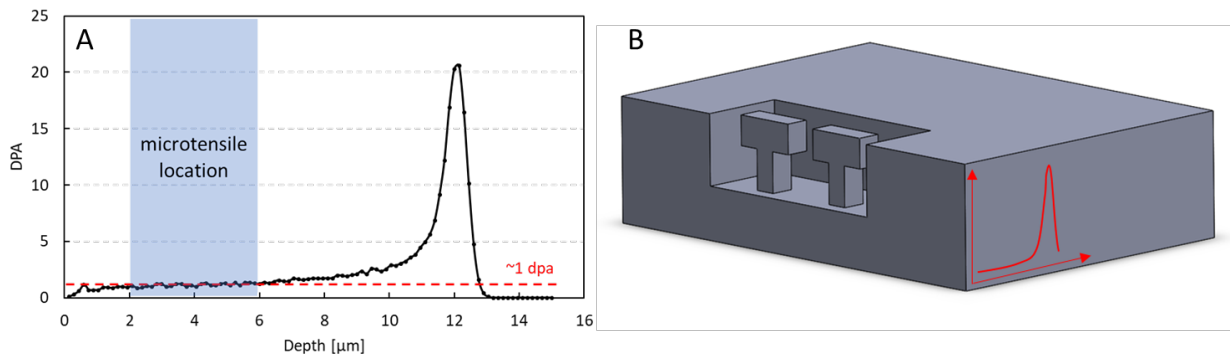
Figure 5-9. A) Kinchin-Pease DPA vs. depth profile. B) Schematic of the sample. The general fabrication location for the microtensiles is indicated in Figure 5.9A.

5.2.1.2.2. FIB preparation of microscale bicrystal tensile bars

A gallium focused ion beam (FIB) was used to fabricate the microtensile bars, as shown in Figure 5.10A. Rough milling was conducted at 30 keV with currents of 1-3 nA and the final cleaning was performed at 0.3 nA. The detailed fabrication procedure for microtensile bars using FIB is outlined in [95]. The aspect ratio (width:height) of the gauge length is between 1:2.5 and 1:4. The width of the gauge is ~1-1.5 µm and the length of the gauge ~3.5-4.5 µm. The exact dimensions of each sample were measured using the SEM to calculate yield stress after testing.

Ion channeling contrast imaging was used to reveal the microstructures of the samples to map out the interfaces within the material. The microtensile samples were fabricated to contain one or a couple of interfaces across the gauge length, as shown in Figure 5.10B. Electron Back Scattered Diffraction (EBSD) was done on the gauge section of the tensile bars to obtain the detailed crystallographic information and the interface characteristics (Figure 5.10C). The EBSD was done at 20 keV, ~0.1 µm step size. The crystal orientations and misorientation angels were then extracted using the Oxford EBSD software.

The crystal orientations can be used to calculate the values of resolved shear stress for the individual grains, using Schmid's law. The Schmid factors of the different slip systems can be often used to determine the probable active slip systems. The misorientation angle between two adjacent grains at any given interface was recorded using the Oxford EBSD software, as shown in Figure 5.10D. In this work, we classified the boundaries as either high or low angle boundaries. Experimental data suggests that the delineation between the low and high angle grain boundaries to be near 15° [136,137]. In this study, the low and high angle boundaries considered are ~4.3° and ~53° respectively, which are far from the approximate 15° transition angle.
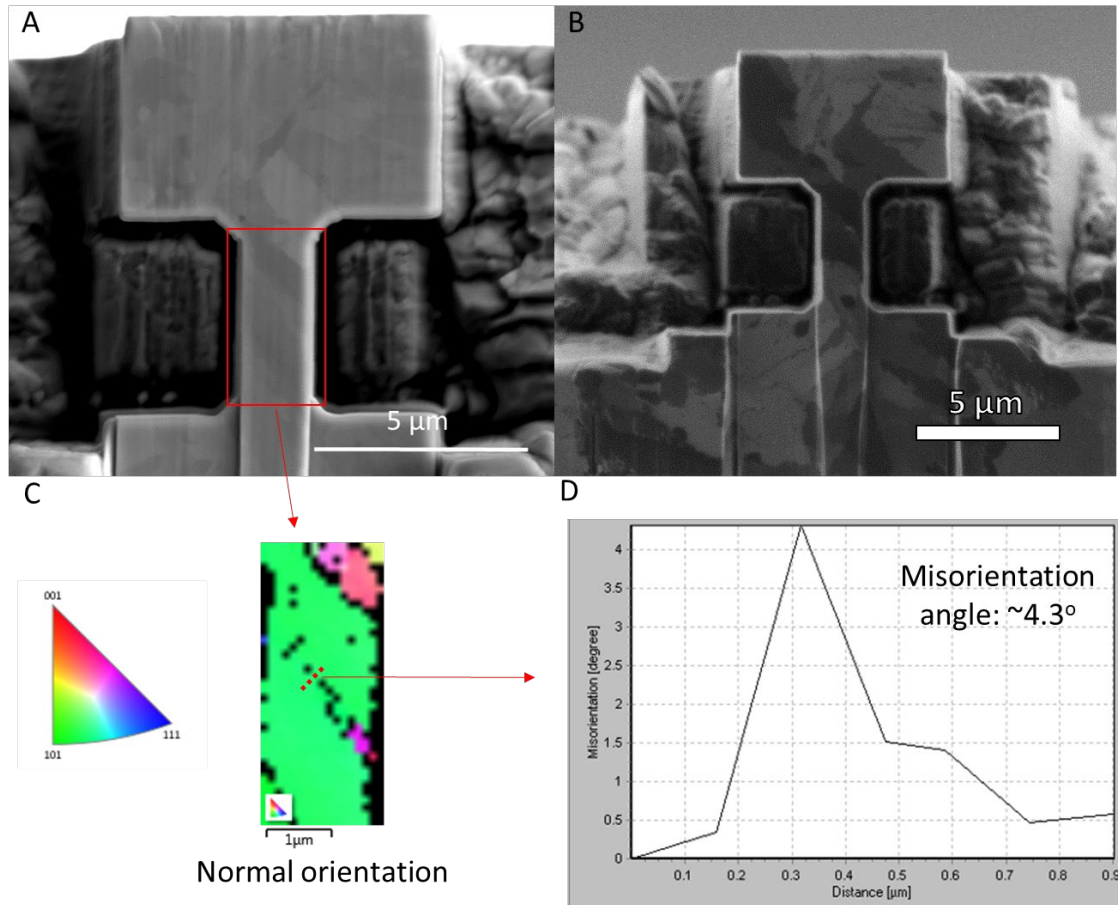
Figure 5-10. (A) The SEM image of a representative microtensile bar. (B) the Focus-Ion Beam (FIB) image shows the microstructures, corresponding to the microtensile bar. (C) The EBSD scan of the gauge length. (D) The plot of the misorientation vs distance from the EBSD Oxford software

5.2.1.2.3. Microtensile Testing

For this research, the Hysitron PI-85 Picoindenter with a custom-made tensile gripper was used [95]. The tests were performed in situ SEM under displacement control at a rate of 10 nm/s. The videos of the representative unirradiated and irradiated tests are included in the Supplementary section of this publication.

5.2.1.3. Results and Analysis

In this section, the deformation behavior of the four HT9 microtensile specimens containing martensitic boundaries before and after the irradiation are compared. The unirradiated microtensile 1 contains a high angle martensitic boundary; the unirradiated microtensile 2 is expected to contain multiple boundaries; the irradiated microtensile 1 contains a high angle martensitic boundary; and the irradiated microtensile 2 contains a low angle martensitic boundary. The stress-strain curves are reported and analyzed with respect to the microstructures of the tensile bars.

5.2.1.3.1. Deformation behavior of HT9 unirradiated tensile bar containing a high angle martensitic boundary.

Figure 5.11A shows the FIB image of the side view of the unirradiated microtensile 1. The FIB-etched image clearly reveals a boundary running across the gauge length. The EBSD scan of the gauge length provides the crystal orientations of the grains and the misorientation angle of the boundary (Figure 5.11B). The loading orientations of the two grains are $[1\bar{6}0]$ and $[\bar{5}\bar{3}6]$ with the corresponding SF values of 0.463 and 0.420, respectively. The misorientation angle for the boundary is ~53° (high angle grain boundary). The microtensile bar was tested to failure. As shown in Figure 5.11C, the plastic deformation takes place within the upper grain in the form of multiple slip band formation. The higher SF value of the upper grain means that the grain sees a higher resolved shear stress as compared to the lower grain; therefore, it is more likely for the deformation to initiate and progress in the upper grain. The location of failure is compared to the location of the high angle boundary to confirm that the failure does not occur at the martensitic boundary (Figure 5.11D). The finding is consistent with the mechanical properties of bulk scale HT9 samples where the deformation is ductile [21]. Additionally, we tested another unirradiated microtensile that contains multiple grain boundaries, and we observed stable plastic deformation and necking failure.
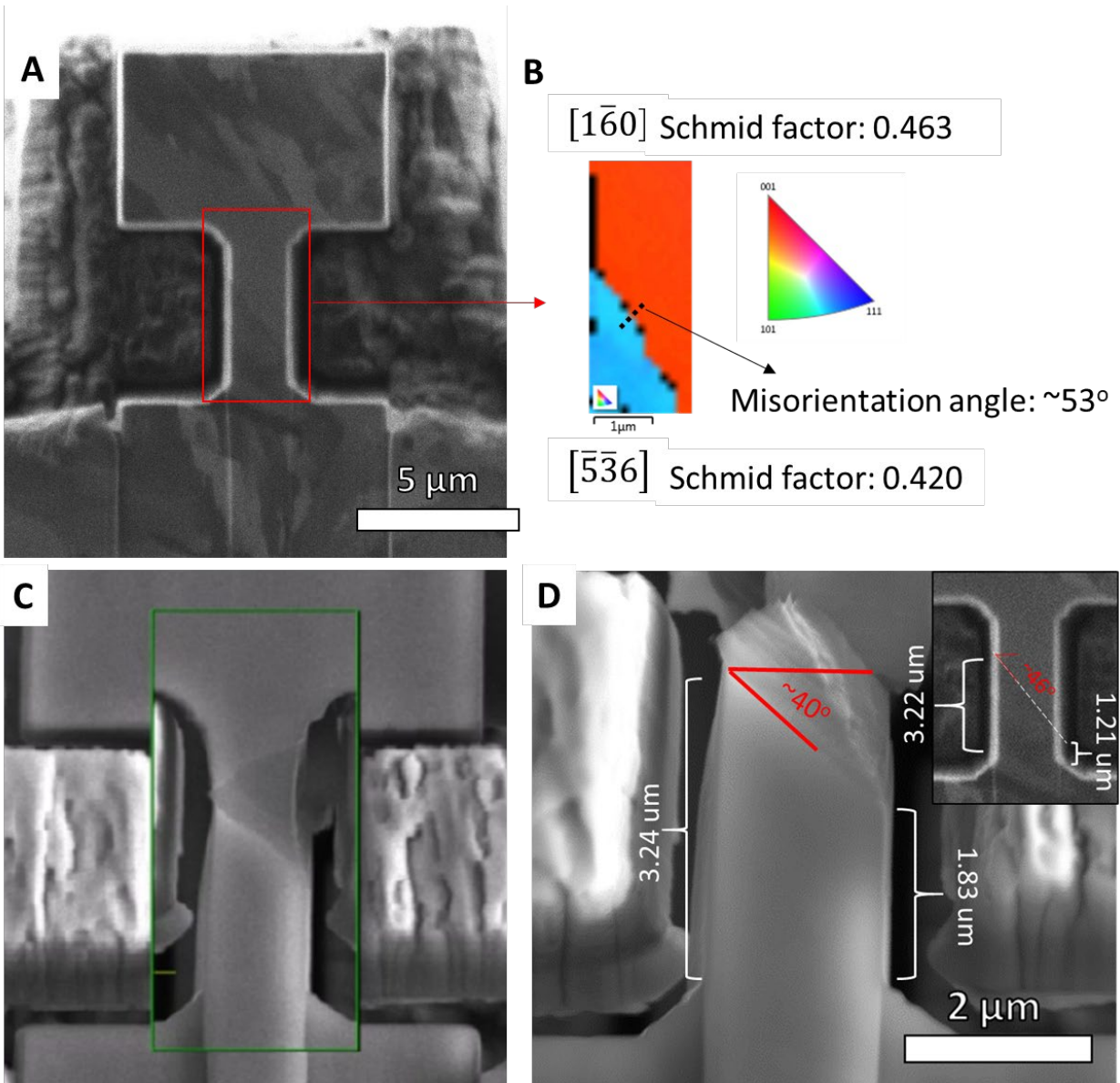
Figure 5-11. (A) The FIB image of the unirradiated microtensile 1, showing the etched microstructure along the surface of the gauge length. (B) The corresponding EBSD scan shows that the martensitic boundary of interest is a high angle grain boundary. (C) The snapshot of the test video during the deformation. (D) SEM images showing the comparison between the location of the martensitic boundary and the failure location.

5.2.1.3.2. Deformation behavior of HT9 irradiated tensile bar containing a high angle martensitic boundary.

Figure 5.12A depicts the SEM image of the irradiated microtensile sample 1, containing high angle martensitic boundaries. The EBSD maps out the multiple boundaries in the gauge length (Figure 5.12B). From the EBSD mapping, the misorientation angle of the martensitic boundary with the dotted line is measured to be ~53°. Important to note that, there is some amount of image drift

during collecting the EBSD map of the gauge length. To confirm the location of the boundaries, FIB etching was performed to reveal the interfaces (Figure 4C). FIB cleaning of the microtensile was performed at 10 keV after the FIB etching to remove the FIB damage before the mechanical testing. During the testing, the deformation took place at the high angle boundary, which leads to failure at the martensitic boundary. No deformation was observed within the individual grains, as shown in Figure 4D.
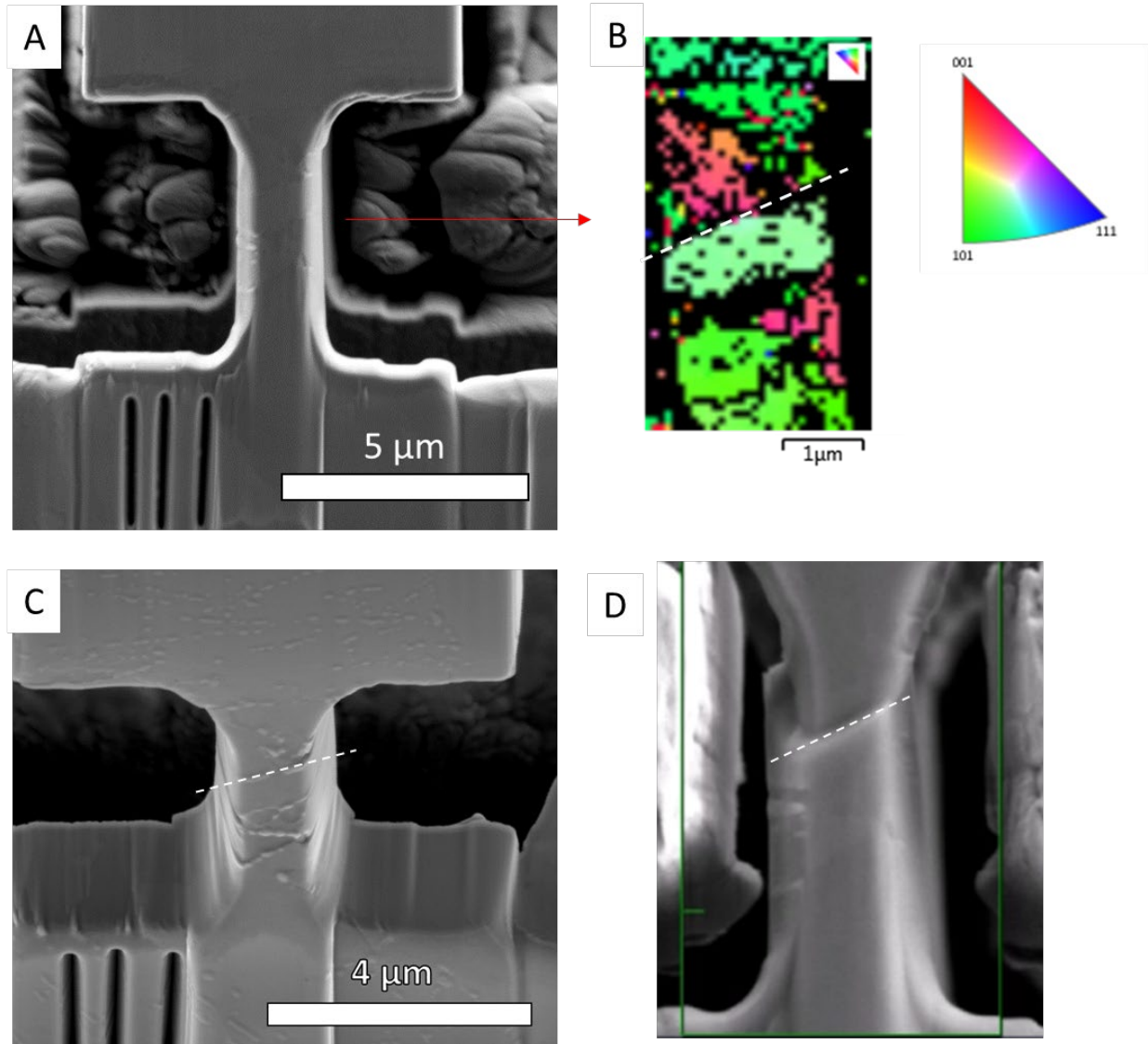
Figure 5-12. (A) The SEM image of the irradiated microtensile 1. (B) The corresponding EBSD scan of the surface of the gauge tensile bar, showing the microstructure. The misorientation of the boundary with the dotted line is measured to be ~53º. (C) The SEM image of the etched microtensile from a top down viewing angle, revealing the different boundaries decorated with carbides, which are consistent with the EBSD scans. (D) The snapshot of the test video during deformation, showing the deformation and failure took place at the martensitic boundary.

5.2.1.3.3. Deformation behavior of HT9 irradiated tensile bar containing a low angle martensitic boundary

Figure 5.10 and Figure 5.13A show the irradiated microtensile 2 containing a low angle grain boundary. The misorientation angle is measured to be ~4.3°. Interestingly, the deformation and failure do not take place at the low angle martensitic boundary. The microtensile failed in a brittle manner. Figure 5.13B shows the snapshot before the brittle failure taking place. The brittle behavior is consistent with the macroscopic tensile tests of the irradiated samples. The comparisons in the stress-strain curves among all the conditions are shown in the following section.
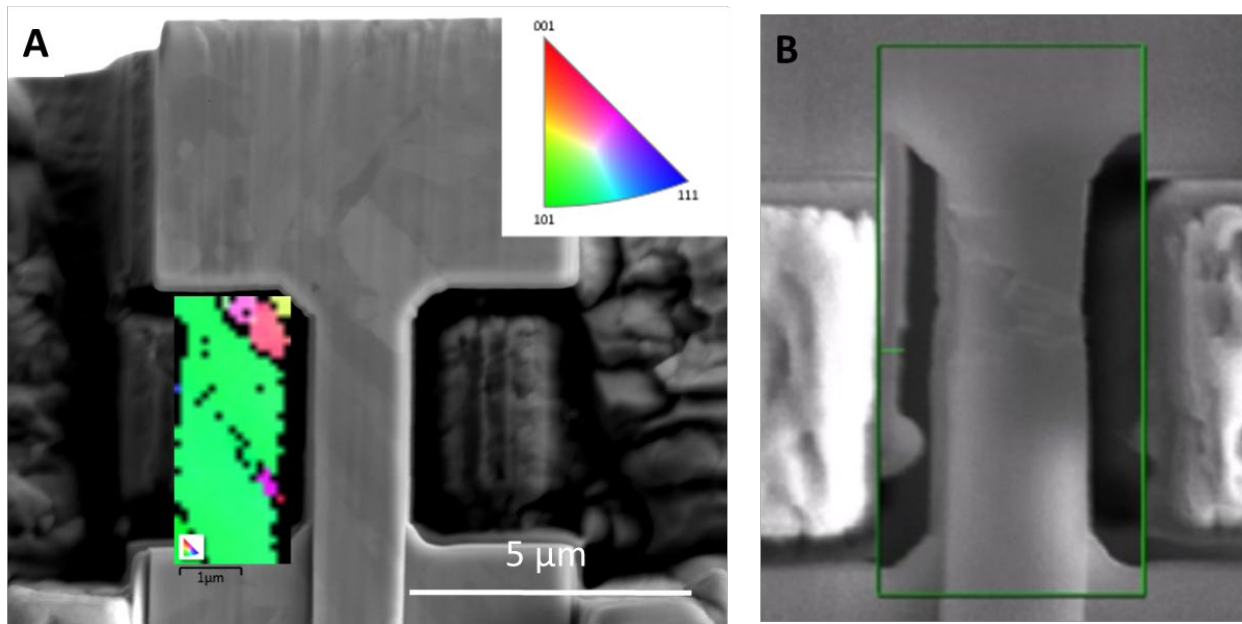
Figure 5-13. (A) The SEM image of the irradiated microtensile 2 containing a low angle martensitic boundary (as shown in Figure 1). (B) A snapshot of the test video, showing the deformation before brittle fracture.

5.2.1.4. Discussion

5.2.1.4.1. Comparison between the stress-strain curves between the unirradiated and irradiated conditions

Figure 5.14 shows the stress-strain curves of the individual microtensile bars. Although both unirradiated microtensile bars deformed in a ductile mannner, their corresponding stress-strain curves show different features especially taking the microstructure in account. The unirradiated microtensile 2 exhibits a higher flow stress and more stabilized plastic flow as compared to the unirradiated microtensile 1. In the unirradiated microtensile 1, the deformation takes place within a single grain via multiple slip band formation. As discussed in Ref [138], the dislocation avalanche at the microscale can lead to strain burst behaviors and limit the ability to work harden. Therefore, the stress-strain curve shows a lack of strain hardening and intermittent load drops as a consequence of the strain burst events. In the unirradiated microtensile 2, one possible explanation for the suppression of the discrete slip band formation is because the dislocations

pile up at the boundaries within the tensile bar. Those pile-ups increase the flow stress and suppress the dislocation avalanche events. As a consequence, the dislocations of different slip systems can interact and contribute to strain hardening in that condition. Ref [138] demonstrates that when the microtensile specimens are highly constrained by interfaces (grain boundaries or coating), the strain bursts can be suppressed, and strain hardening followed by necking can take place.

In the irradiated condition, the irradiated microtensile 2 shows significantly higher flow stress as compared to the irradiated microtensile 1. The difference in flow stress originates from the difference in the observed failure modes. In the irradiated microtensile 1, the failure occurred at the high angle martensitic boundary before the yielding of the matrix material. In contrast, the failure did not take place at the low angle martensitic boundary in the irradiated microtensile 2; therefore, deformation take places within the grains. As a result, the flow stress increases significantly as compared to the unirradiated condition because of the irradiation-induced loops. Figure 5.14 points out the complexity of the HT9 microstructures and the sensitivity of the stress-strain response with respect to the microstructures. Because the HT9 and other TMS microstructures consist of many closely-spaced interfaces, it is crucial to obtain the microstructure information of the test samples in order to correctly interpret the stress-strain results. Although we were not able to obtain 3D microstructure information of the test samples, the observed deformation behaviors are consistent with the 2D microstructures obtained from the gauge surface.
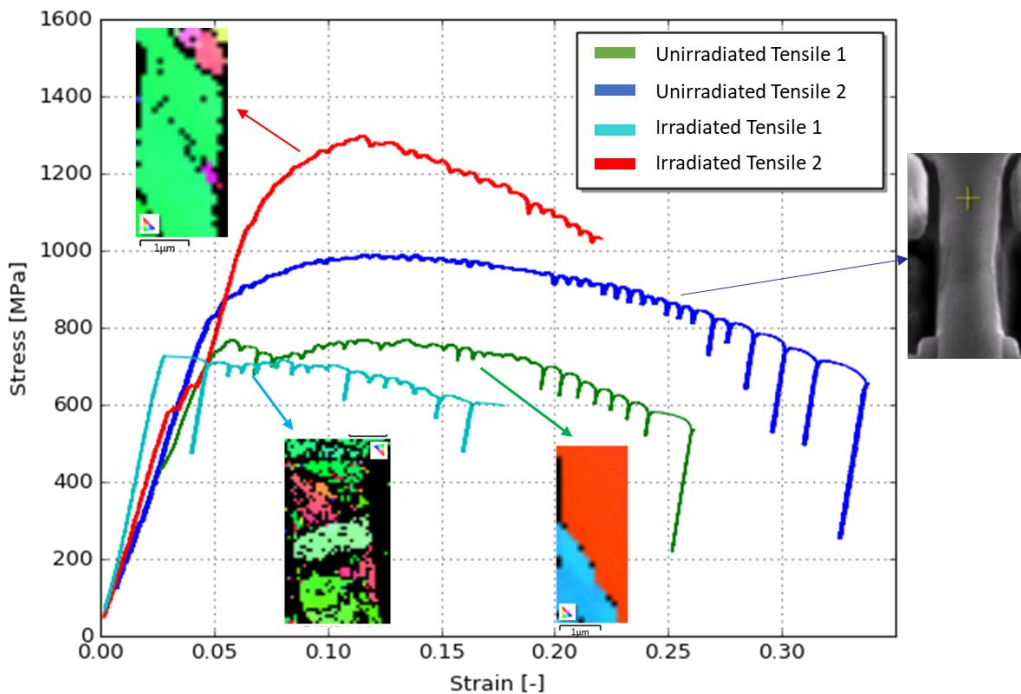
Figure 5-14. The strain-strain curves of the microntensiles, accompanied by the corresponding EBSD maps or SEM image during deformation.

56

The differences in the failure modes between the microtensiles containing high and low angle boundaries suggest that high angle martensitic boundaries are more susceptible to irradiation-induced failure as compared to the low angle martensitic boundaries. Based on the grain boundary characteristics, there are some potential explanations on the observed difference between low angle and high angle grain boundaries. Since the low angle grain boundaries exhibit higher structural order and lower free volume, it has been reported that grain boundary segregation (via thermal treatment and irradiation) is prominent in high angle grain boundaries as compared to low angle grain boundaries [139,140]. The preferential precipitate coverage via thermal treatment in the high angle grain boundaries have been shown in ferritic steels, including tempered martensitic alloys [141]. In general, the intergranular precipitates are thought to increase the stress intensity at the high angle grain boundaries [26]. In the unirradiated condition, the intergranular precipitates can enhance plasticity near the precipitates due to the higher stress concentration. However, as the plasticity in the grain interior is severely limited in the irradiated condition, the intergranular precipitates can promote crack initiation at the grain boundary. Furthermore, radiation-induced segregation can preferentially take place at the high angle grain boundaries in the tempered-martensitic alloys [139,142]. The segregated layer can further embrittle the grain boundaries, promoting grain boundary failure. The third important aspect is the dislocation transmission ability of the grain boundaries. Due to the low misorientation angle, the low angle grain boundaries are more transparent to dislocation motion as compared to high angle grain boundaries [143]. Therefore, the low angle grain boundaries experience less stress intensity resulted from dislocation pile-up as the dislocations can get absorbed or transmit through the grain boundaries. More in-depth experimental examination of the stress intensity at the high and low angle grain boundaries is needed to confirm the exact mechanisms responsible for the differences in failure modes.

5.2.1.4.2. Summary of the YS and CRSS values of the unirradiated and irradiated conditions

Table 5.2 summarizes the yield stress values of the individual stress-strain curves. The critical resolved shear stress values are calculated for the unirradiated tensile 1 and irradiated tensile 2 where the deformation took place within the grains. The CRSS values are calculated as the product between the maximum Schmid factors and the measured yield stress. The SF values are also listed in Table 5.2. The YS values of the unirradiated tests (~706 and ~840) are slightly higher than the macroscopic YS reported in [21]. It is expected because of the extrinsic size effect [105,138] in which the microscale dimensions of the tensile gauge limit the maximum length of the dislocation sources. This effect is described by the single-arm source model [144]. Interestingly, the yield strength of the irradiated microtensile 2 (~1100) is consistent with the macroscopic YS [21]. The consistency in the YS values between the microscale and the macroscale tests in irradiated samples is particularly discussed in [104,145]. The dense distribution of irradiation-induced loops reduces the mean obstacle spacing well below the dimensions of the samples. Therefore, the stress required to move the dislocations are determined by the obstacle spacing, instead of the dimension of the samples. In other words, the size effect is significantly reduced in the irradiated condition. Since CRSS value is independent of the grain orientations, we can estimate the yield stress values for grains G1 and G2 by dividing the CRSS value by the corresponding maximum Schmid factor values (Table 1). If the CRSS of the irradiated microtensile

57

2 is used to calculate the YS of the grains in irradiated microtensile 1 it can be seen that the estimated YS values for G1 and G2 are 995 MPa and 882 MPa, respectively. Therefore, we confirmed that the stress seen by the irradiated microtensile 2 is lower the YS required to initial deformations within the grains.

Table 5.2. Summary of the YS, CRSS, and the microstructures of the microtensiles

	Unirradiated 1	Unirradiated 2	Irradiated 1	Irradiated 2
YS [MPa]	~706	~840	~724* (G1: 995*, G2: ~882*)	~1100
CRSS [MPA]	~327	N/A	N/A	~428

5.2.1.5. Conclusion

Understanding the effect of irradiation on the mechanical properties of HT-9 and other tempered martensitic steels is crucial for the deployment of the next generation of reactors. In this study, we utilized the novel microtensile testing to examine the influence of microstructures on the deformation behavior and flow stress response before and after the irradiation. The finding of this study can be summarized as followed:

- In the unirradiated condition, the deformation is ductile and no martensitic boundary failure is observed.
- After proton irradiation to 1 dpa at 300C, the high angle martensitic boundary is more susceptible to failure than the low angle martensitic boundary. The irradiated sample with the high angle martensitic boundary failed below the estimated yield stress values of the adjacent grains. On the other hand, after irradiation to 1 dpa, no failure of the low angle martensitic boundary is observed and the deformation is brittle.
- The YS values of the irradiated condition are consistent with the macroscopic tensile test data. Due to the expected size effect, the YS values of the unirradiated condition are higher than those of the macroscopic data

Although we were able to demonstrate the influence of the microstructures on the deformation behavior in the presence of irradiation damage in a HT9 alloy, it is important in future work to investigate a range of high angle and low angle martensitic boundaries in order to draw more quantitative insights on the influence of irradiation on the strength of the martensitic boundaries.

5.2.2. Development of Microscale Bicrystal Tensile Testing for Strength Measurement of Oxidized Grain Boundaries of Alloy 600 Exposed to PWR Environments

5.2.2.1. Background

Ni-based alloy 600 has been used as steam generator tubes in many pressurized water reactors (PWR). The compositional ranges of Alloy 600 are in the range 14.0-17.0 wt% Cr, 6.00-10.00 wt% Fe, and 70.0 wt% min Ni (plus Co). Many studies have reported that alloy 600 is susceptible to intergranular corrosion and intergranular stress corrosion cracking (IGSCC) when exposed in the primary water loop of the PWRs [146–153]. Although the alternative Ni-based alloy of higher chromium content (~30% Cr [154]), alloy 690, has been shown to exhibit higher resistance to

IGSCC in primary water environments [25,155], it remains important to understand the IGSCC mechanism for the currently deployed alloy 600 components in PWRs.

Previous studies have looked at the relationship among alloy 600 microstructures, operating environment, and stress corrosion cracking (SCC) susceptibility [148,151,156–159]. The IGSCC susceptibility varies strongly with the thermal history of alloy 600 [148,151]. In particular, the thermally-treated (TT) alloy 600 shows higher resistance to IGSCC as compared to the solution annealed (SA) condition [152,159]. For the TT condition, a thermal treatment was performed to nucleate intergranular carbides (IC) ($M_{23}C_6$ and M_7C_3) [160]. The presence of IC have shown a positive effect in delaying crack initiation and reducing the crack growth rate [161]. Two main mechanisms have been proposed to explain the positive role of IC. From the perspective of fracture mechanics, the IC are thought to promote crack tip blunting by enhancing dislocation emission [26]. Additionally, the hard intergranular precipitates can lengthen the crack path by deflecting the crack trajectory around the precipitates. These two effects contribute to a lower crack growth rate. From the corrosion perspective, the IC enable the formation of stable Cr_2O_3 oxides [162] along the grain boundaries. The stable oxides limit further inward diffusion of oxygen along the grain boundaries, thus limiting the oxidation rate. The effect of cold work (CW) on the IGSCC susceptibility was also investigated [157,158]. Studies have found that SCC behavior varies with the direction of cold rolling and the local strain field [157].

In addition to the experimental efforts, stress corrosion cracking models have been developed to predict the IGSCC behaviors for nickel-based alloys and austenitic stainless steels [163–165]. The challenge with a number of empirical models is the inability to capture the physical mechanism. With these models, the input parameters such as crack initiation stress are macroscopic parameters which cannot fully capture the local mechanisms. Efforts have been invested to develop a local model to predict IGSCC that aim to take into account the physical mechanisms (incubation, initiation, crack growth) and the microstructures of the materials [164]. One of the main challenges is developing new testing procedures to experimentally obtain local parameters such as oxidized grain boundary strength.

In this study, we developed a novel in situ SEM microtensile testing procedure for measuring oxidized grain boundary strength. Important factors such as interfacial constraint, slip transmission, and grain boundary orientation are discussed. Alloy 600 of three thermal histories - solution annealed (SA), solution annealed + thermally treated (SATT), and mill annealed and cold-forged (MACF) – were investigated. The findings reveal that the oxidized grain boundary shear strength plays a larger role than that of the normal strength in introducing grain boundary failure. The general procedure for oxidized grain boundary measurement via in situ SEM microtensile testing is outlined.

5.2.2.2. Methods
5.2.2.2.1. Sample preparation

Alloy 600 samples from Heat NX610XK-11 (0.06 wt% C, 83 appm B) with three different thermal histories were used: mill annealed and cold-forged (MACF), solution annealed (SA), and solution annealed + thermally treated (SATT). The heat was received from the supplier in the mill-annealed (MA) condition (heat treated at 927 °C for 3.5 hours, water-quenched). The MA

material was cold forged (CF) to 15% deformation to produce the MACF condition. To produce the SA condition, the MA material was solution annealed at 1100 °C for a 0.5 h, followed by a water quench. Further heat treatment of the SA material at 704 °C for 12 hours with subsequent air cooling produced the SATT condition.

Coupons/Specimens (approximately 15 mm diameter by 5 mm thickness) were prepared using electric discharge machining (EDM). The specimens were ground with successively finer SiC paper, up to 600 grit; one side was further polished to produce a surface for electron backscatter diffraction (EBSD), with a final step that used 50 nm colloidal silica. They were subsequently suspended within a stainless-steel autoclave for oxidation in simulated PWR primary water chemistry (1000 ppm B and 2 ppm Li, 360 °C, 25 cc H_2 / kg H_2O) for 4400 hours at Pacific Northwest National Laboratory. Once removed from the autoclave, the coupons were cross sectioned and polished. The samples were then examined using SEM to measure the intergranular attack (IGA) and the average oxidation depth for the three different conditions. Representative images of the IGA are shown for the SA, SATT, and MACF conditions in Figure 5.15A,5.15B, and 5.15C respectively. The average IGA depths are shown in Figure 5.15D.
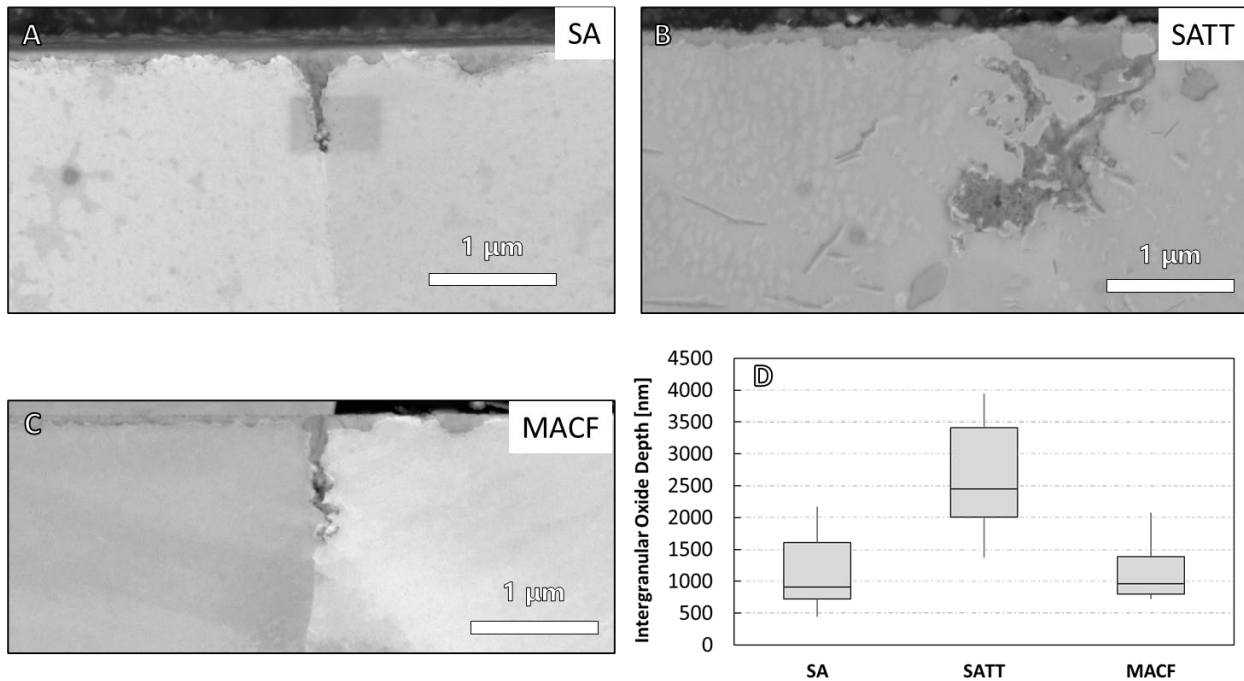
Figure 5-15. Representative SEM images showing the intergranular attack of (A) the SA condition, (B) the SATT condition, (C) the MACF condition; (D) box and whisker plot showing the intergranular oxide depth for the three conditions. The box represents the inner two quartiles of the distribution and the central line represents the median value.

5.2.2.2.2. Grain boundary selection

The FEI Quanta FIB (30 keV, 7 nA electron beam) was utilized to perform EBSD mapping of the surface near the sample edge. The EBSD maps identified the locations of grain boundaries, the grain boundary orientation angles, and the crystal orientations of the adjacent grains. The crystal orientations of the adjacent grains were used to calculate their maximum Schmid factors

and the corresponding highest resolved shear stress values seen within the grains. In general, the grain boundaries for testing were selected based on the following considerations.

1. Low and similar Schmid factors for adjacent grains in respect to the loading direction. This consideration takes into account the competition between the grain interior and the grain boundary. It was applied to help ensure that the grain boundary would reach a sufficiently high stress for failure prior to the deformation of the grain interior.

2. Twin grain boundaries are avoided. The consideration was applied because experimental observations have established that twin boundaries are highly resistant to IGSCC [166]. Important to note, this consideration was developed after a few microtensile tests (of unoxidized grain boundaries), so this condition was not satisfied for all microtensile samples.

5.2.2.2.3. Fabrication procedure of microtensile for grain boundary testing

Similar to the FIB preparation procedure for TEM lamellae, a protective platinum layer was placed over the selected grain boundaries for the trenching process, as indicated in Figure 5.16A. FIB trenches were made both in front and behind the platinum region. The FIB lamellae were lifted out using the Omniprobe SEM micro-manipulator onto Cu grids. At this stage, fine FIB cutting was performed to shape the lamellae into microtensile bars with an approximate cross section of 1.5 μm x 1.5 μm using a 0.3-0.5 nA and 30 keV Ga ion beam, as shown in Figure 5.16B. Energy Dispersed Spectroscopy (EDS) was performed to confirm the presence of the grain-boundary oxide. The incline angles of the grain boundaries were then measured, which were later used to visualize the test geometry and calculate the resolved stresses, both normal and shear, acting on the grain boundaries. To have the flexibility to test any grain boundary of interest, the Push-to-Pull (PTP) device from Bruker was used for the tensile testing, as shown in Figure 5.16C. The tensile bars were lifted off its Cu grid and mounted on to the PTP device. The setup requires the tensile sample to be mounted over the gap, as indicated by the red circle in Figures 5.16C and 5.16D. The samples were welded to the PTP device using Pt deposition with a Ga ion beam at 50 pA and 30 keV (Figure 2D). Pt deposits also accumulated on the microtensile samples, so a final FIB cleaning using 0.1-0.3 nA at 15 keV was performed to remove them.
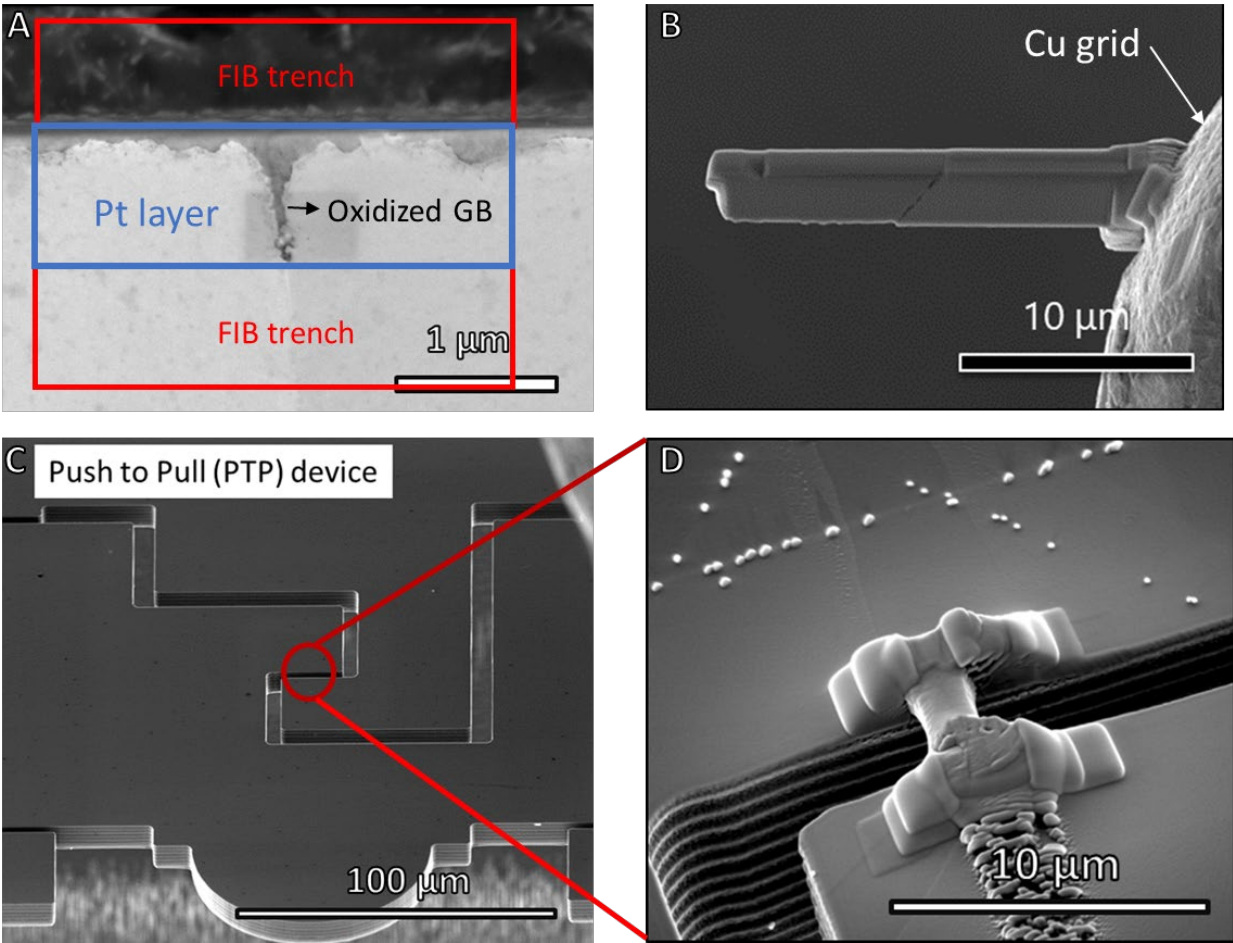
Figure 5-16. (A) A representative top-down SEM image, containing an oxidized grain boundary, on which regions of trenching and Pt deposition has been outlined.; (B) SEM image of the microtensile bar mounted to the Cu grid; (C) SEM image of the top view of the Push-to-Pull device; (D) A close-up view of the microtensile bar mounted on the PTP device.

5.2.2.2.4. Push-to-pull microtensile testing

The PTP device consists of a mobile and immobile section as shown in Figure 5.17A. When the micro-indenter pushes on the mobile section, the width of the gap under the microtensile sample increases; therefore, the "push" provided by the micro-indenter is translated into a "pull" on the sample. The schematic of the sample geometry with respect to the PTP device is shown in Figure 5.17B. For the rest of the paper, grain 1 and grain 2 in Figure 5.17B are referred as left and right grains, respectively. The Picoindenter 88, from Bruker, was used for the micro-indentation of the PTP device, performed in compression mode at a constant displacement rate of 10 nm per second. A video was recorded for each test.
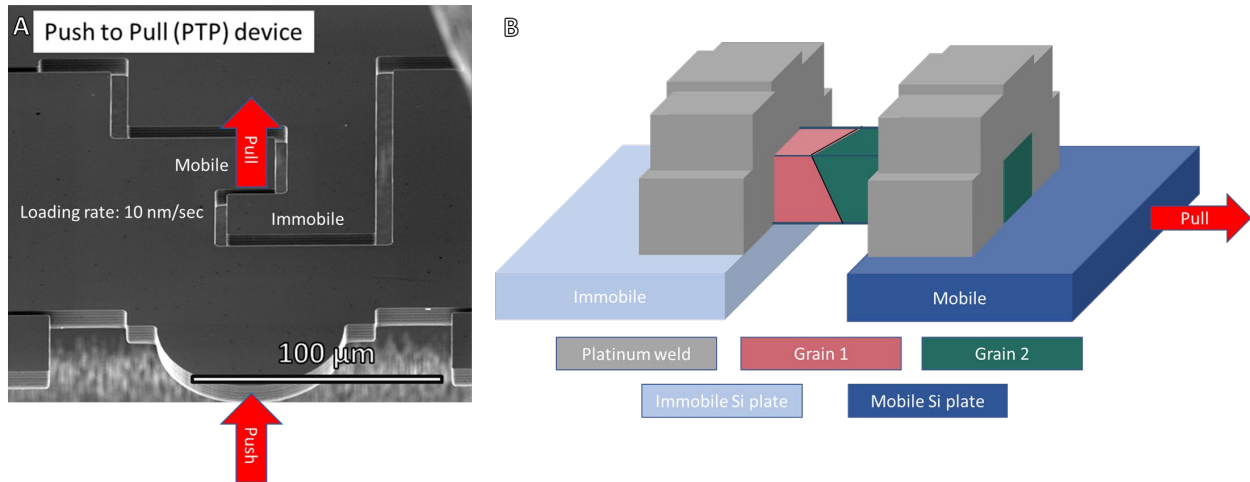
Figure 5-17. (A) A SEM image of the PTP device, labeled to show the "push" and "pull" mechanism; (B) a schematic of the microtensile bar setup

5.2.2.3. Results

A total of 8 microtensile bi-crystal tests (2 in SA condition, 4 in SATT condition, and 2 in MACF condition) containing oxidized grain boundaries were tested and reported here. The grain boundary normal and shear stresses were calculated from the maximum applied stress. The resolved shear stresses of the slip systems with the highest Schmid factors within the grains were also calculated. The definitions of the stresses are shown in the Supplementary section. All values are reported in Table 5.3.

Table 5.3. The resolved shear stress values of the left and right grains and the grain boundary shear stress and normal stress values are reported.

Test	RSS 1 [MPa]	RSS 2 [Mpa]	GB normal stress [Mpa]	GB shear stress [Mpa]	Failure at GB
SA bar 1	273	283	427	310	No
SA bar 2	334	201	526	362	No
SATT bar 1	253	243	221	342	Yes
SATT bar 2	239	232	544	156	No
SATT bar 3	149	154	323	226	No
SATT bar 4	393	358	618	371	Yes
MACF bar 1	333	294	336	336	Yes
MACF bar 2	419	470	593	475	Yes

The deformations behaviors observed during oxidized grain boundary testing

63

Figure 5.18 shows the SEM images of the deformed microtensile bars after being tested to failure. A range of different deformation and failure mechanisms were observed in the tests. It is important to note that the grain boundaries of the SA tests were not completely oxidized, and the oxide depth is shallow. As a consequence, grain boundary failure in the SA condition was not observed; however, the observed deformation did provide important insight. From the test videos and the post-deformation SEM images, the deformation mechanism of each test is described as follows:
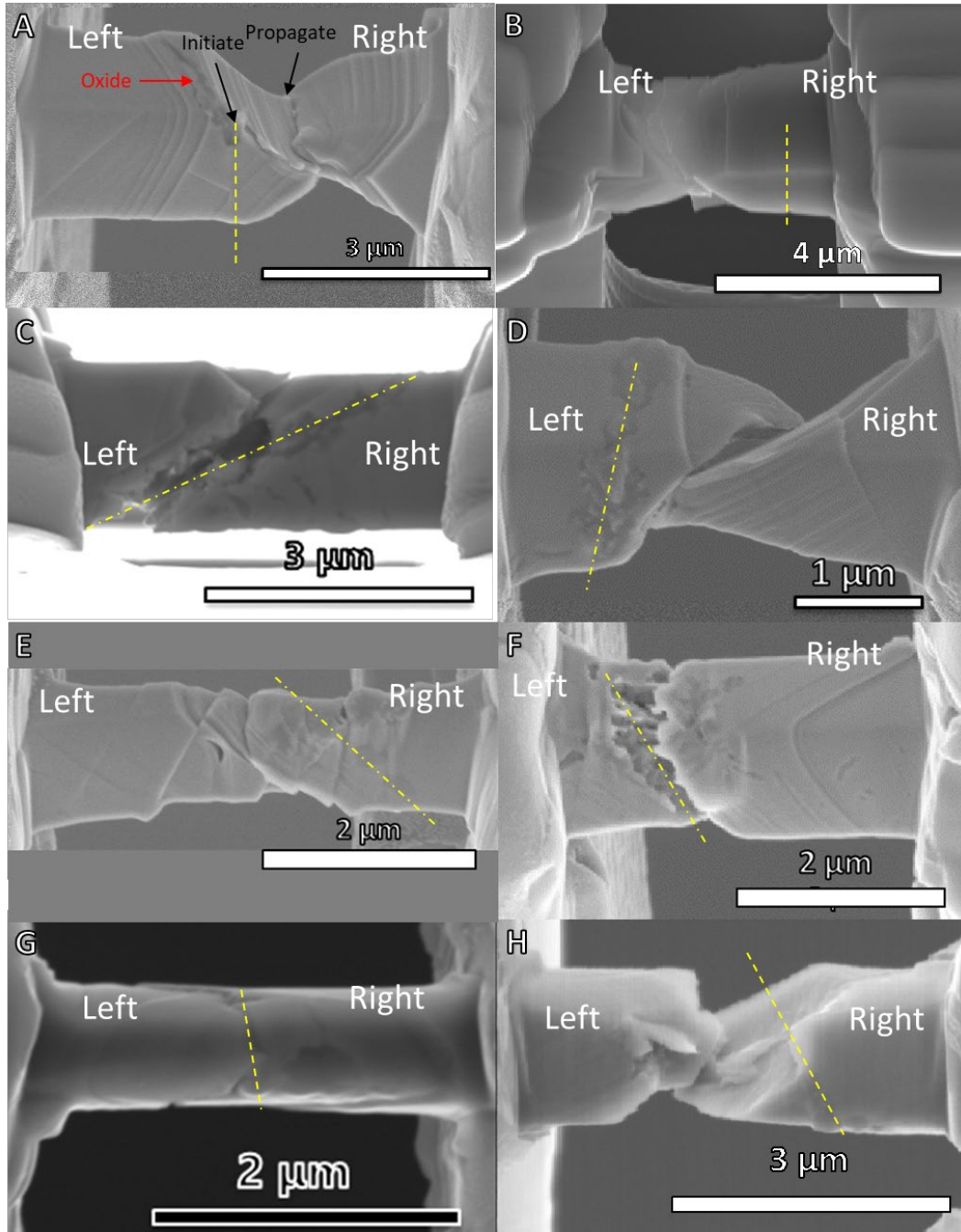
Figure 5-18. Post-deformation SEM images of (A) SA bar 1; (B) SA bar 2; (C) SATT bar 1; (D) SATT bar 2; (E) SATT bar 3; (F) SATT bar 4; (G) MACF bar 1; (H) MACF bar 2. The dashed yellow lines indicate the grain boundary trace on the specimen surfaces.

- SA bar 1 (Figure 5.18A) : According to the test video, the deformation initiated at the oxidized edge of the grain boundary, and propagated into the right grain (Figure 5.18A). It is important to note that the entire grain boundary was not oxidized so it is possible that the grain boundary strength was not significantly degraded by the oxidation, making deformation in the grain interior preferable.

- SA bar 2 (Figure 5.18B): The failure was abrupt and occurred in the left grain. It is hypothesized that a redeposited layer of FIBed-away material prevented the deformation. When the redeposition layer broke, then the specimen itself failed abruptly.

- SATT bar 1 (Figure 5.18C): Gain boundary failure was observed. The measured grain boundary shear stress (342 Mpa) is significantly higher than the RSS of both grains (253 Mpa and 243 Mpa) while the grain boundary normal stress (221 Mpa) is slightly lower.

- SATT bar 2 (Figure 5.18D): In the test video, the deformation initiated at the edge of the fully oxidized grain boundary and propagated into the right grain; therefore, no grain boundary failure was observed. From Table 5.3, the grain boundary shear stress (156 Mpa) is lower than that of the SATT bar 1 (342 Mpa) while the grain boundary normal stress is significantly higher (544 Mpa vs. 221 Mpa).

- SATT bar 3 (Figure 5.18E): The deformation and failure were observed entirely in the left grain. The deformation took place entirely within the left grain via the formation of multiple slip bands. The grain boundary shear stress and normal stress are 226 Mpa and 323 Mpa, respectively.

- SATT bar 4 (Figure 5.18F): The bar failed at the oxidized grain boundary when the grain boundary shear stress reached a similar value (371 Mpa) as that of the SATT bar 1 (342 Mpa).

- MACF bar 1 (Figure 5.18G): The bar failed at the oxidized grain boundary at grain boundary shear and normal stresses of around 336 Mpa.

- MACF bar 2 (Figure 5.18H): Failure at the oxidized grain boundary was observed. The grain boundary shear stress and normal stress are higher than those of the MACF bar 1.

The roles of grain boundary stresses and other parameters in influencing the resulting deformation and failure modes are discussed below.

5.2.2.4. Discussion
5.2.2.4.1. Effects of grain boundary normal stress and shear stress on grain boundary failures

Figure 5.19 plots the grain boundary shear stress versus the grain boundary normal stress of all the tests. From the plot, several valuable trends were observed in explaining the resulting deformation mechanisms. Four out of the eight tests failed at the oxidized grain boundaries. SATT bar 1 and bar 4, which failed at grain boundaries, have grain boundary shear stress values of 342

MPa and 371 MPa; while SATT bar 2 and bar 3, which did not fail at the grain boundaries, have grain boundary shear stress values of 156 MPa and 226 MPa. The SATT tests suggest that a threshold value of the grain boundary shear stress is required to cause failure at the oxidized grain boundaries. Interestingly, failure of an oxidized grain boundaries is not correlated with the observed grain boundary normal stress value. This trend is evident when noting that the grain boundary normal stress values of SATT bar 1 and SATT bar 4, both of which failed at the GB, are 221 MPa and 618 MPa, respectively. Similarly, the grain boundary normal stress values of MACF bar 1 and MACF bar 2 are 336 MPa and 593 MPa, respectively. Therefore, the results suggest that the grain boundary shear stress plays a more important role in causing grain boundary failure than the grain boundary normal stress.

As indicated in Figure 5.19, 4 out of the 8 tests did not fail at oxidized grain boundaries. Failure of oxidized grain boundaries was not observed for the SA tests, consistent with the very shallow oxide depth in the SA microtensile bars. However, as observed in SA bar 1, the fracture can initiate at the edge of the oxide and propagate into the grain if the slip plane is orientated favorably. In the SATT condition, SATT bar 1 and SATT bar 2 did not reach sufficiently high grain boundary shear stress values to initiate grain boundary failure; deformation within the grain interior took place at a lower stress, and formation of multiple slip bands was observed. In addition to the grain boundary stresses, we examined the influence of dislocation pile-up by the grain boundaries on the deformation process in the bi-crystal tests.
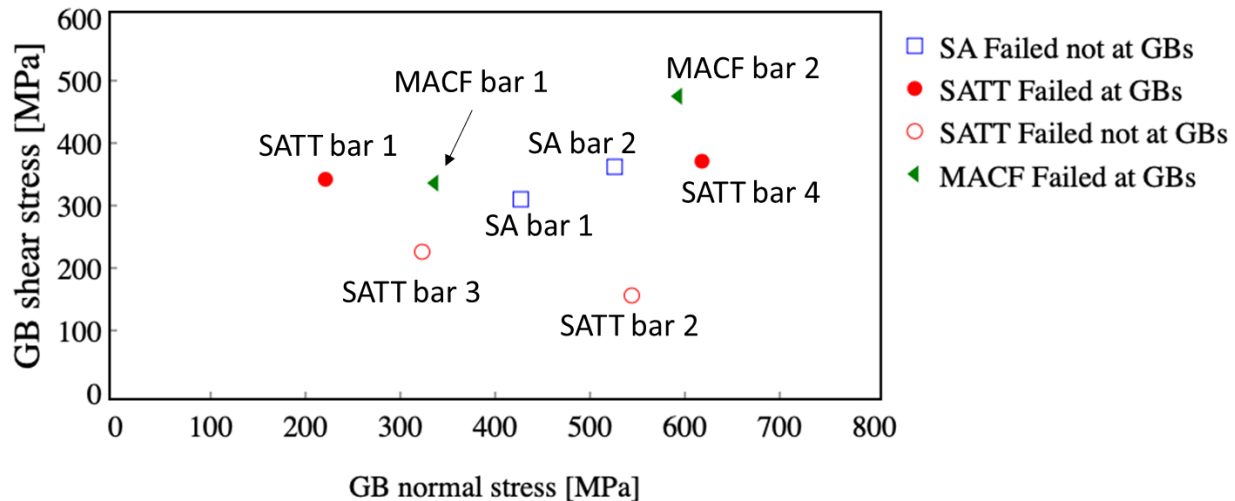
Figure 5-19. Plot showing the grain boundary shear stress versus the grain boundary normal stress

5.2.2.4.2. Blocked volume ratio of the grains in the bi-crystal testing

The deformation mechanisms of in situ SEM bi-crystal testing is inevitably more complex than that of single crystal testing. In addition to the dislocation action within one grain at a set of Schmid factors, the interaction of dislocations with the grain boundary, the transmission of dislocations from one grain to the adjacent grain, and the role of grain boundary strength play important roles in the deformation process. Although the effect of slip transmission ability of grain boundaries has been extensively studied and reviewed [143], it remains a challenging

problem to address. Since the oxidized grain boundary acts as a hard interface, the dislocation transmission across oxidized grain boundaries is severely limited. As a result, dislocation pile-up or dislocation interaction with a hard interface (an oxidized grain boundary in this case) plays an important role in the deformation in the bi-crystal tests containing oxidized grain boundaries. Our developed of the BVR concept in section 5.1.1 provides an extensive investigation on the influence of hard interfaces on the deformation behavior of microscale FCC crystals. As mentioned, the blocked volume of a slip system is defined as the volume within which the slip planes intersect the hard interface (an oxidized grain boundary in this case), such that the dislocations are pinned and cannot escape to the free surface.
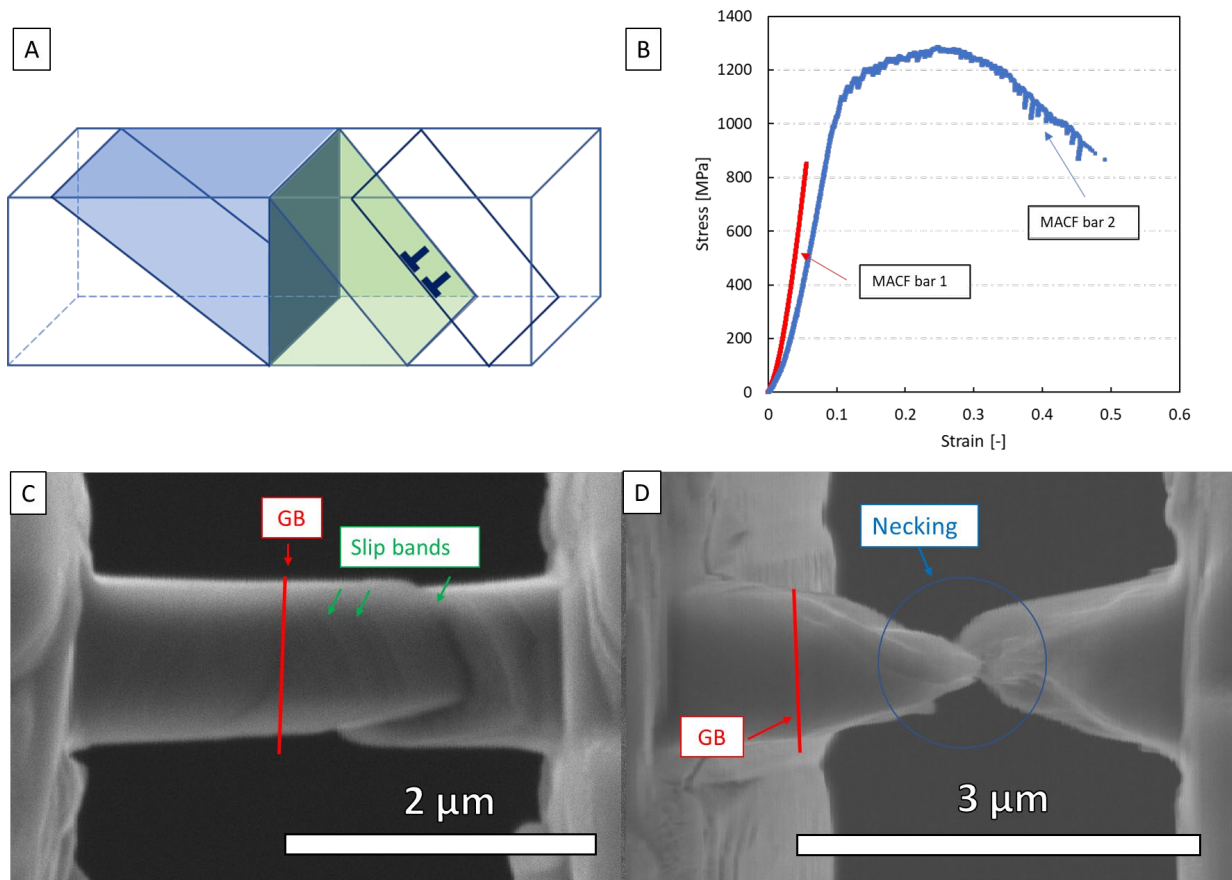
Figure 5-20. (A) schematic of the microtensile bar outlining the blocked volume of the two grains, presented by the blue and green shaded regions; (B) The stress-strain curve of the unoxidized MACF bar 1 and MACF bar 2; Post-deformation SEM images of (C) the unoxidized MACF bar 1 and (D) unoxidized MACF bar 2

As illustrated in Figure 5.20A, the shaded blue and green volumes are considered to be blocked volumes because the slip planes of the slip systems intersect the grain boundary at the center. Within the blocked volume, the formation of discrete slip bands is suppressed, because of the constraining interface. In other words, the blocked volume of the primary slip systems (or slip systems with the highest Schmid factors for FCC materials) indicates the degree of constraint and

dislocation pile-up the grains undergo. The blocked volume ratio (BVR) is then defined as the ratio between the blocked volume over the total volume of each of the two grains in a given microtensile sample. As discussed in section 3.1.1, BVRs above ~0.81, the grain is strongly constrained by the interface and formation of discrete slip bands is suppressed. To demonstrate the effect of the blocked volume ratio in bi-crystal testing, several bi-crystals containing unoxidized grain boundaries, in the MACF condition, were tested. The BVR value of a bi-crystal test is defined as the lower BVR value between the two grains, because it was observed experimentally that the deformation takes place in the grain with the lower BVR value when grain boundary failure did not occur. Figure 5.20B shows the stress-strain curve comparison between bi-crystal tests with a low BVR value of 0.298 (red curve) and a high BVR 0.867 (blue curve). The deformation of the two bi-crystal tests took place within the grain interiors as shown in Figure 5.20C and 6D. The bi-crystal test with a low BVR showed a much lower failure stress and an absence of strain hardening; and the SEM image of the deformed sample indicates discrete slip band formation took place within the grain (Figure 5.20C). In contrast, the bi-crystal test with a high BVR shows a much higher flow stress and strain-hardening response. The SEM image of the deformed sample shows macroscopic-like necking and an absence of slip band formation (Figure 5.20D). In the context of bi-crystal testing of oxidized grain boundaries, high BVRs in the grains means that the majority of the dislocations would pile up at the oxidized grain boundaries instead of escaping to the free surfaces. This condition helps to address a potential scenario characteristic to microscale bi-crystal testing in which dislocation avalanche behavior and discrete slip band formation within the grain interior can take place at a stress below the grain boundary failure stress.

The BVR values of the slip systems with the highest Schmid factors were calculated for all tests. In the tests that deformed within the grain interior, the general observation is that the deformation took place within the grain with the lower BVR value (less constrained by the grain boundary). The grain boundary shear stress versus the BVR values of the tests is plotted in Figure 5.21. The plot shows an important consideration regarding the use of the BVR concept in designing microscale grain boundary testing. The use of BVR is to increase the grain boundary stress values by introducing dislocation pile-up and by suppressing slip band formation within the grains. The role of the BVR value becomes relevant when the grain boundary shear stress values are below the threshold to initiate grain boundary failure. For examples, SATT bar 2 and SATT bar 3 did not fail at the oxidized grain boundary because the grain boundary shear stress did not reach a critical value before the deformation took place within the grain. Therefore, if the BVR values of SATT bar 2 (0.245) and SATT bar 3 (0.607) could be increased to high values (> ~0.8 [138]), the shear stress values can continue to increase to reach the threshold value for grain boundary failure. On the other hand, SATT bar 1 and SAT bar 4 already have sufficiently high grain boundary shear stress values to initiate grain boundary failures, so the BVR values in those tests are not important.
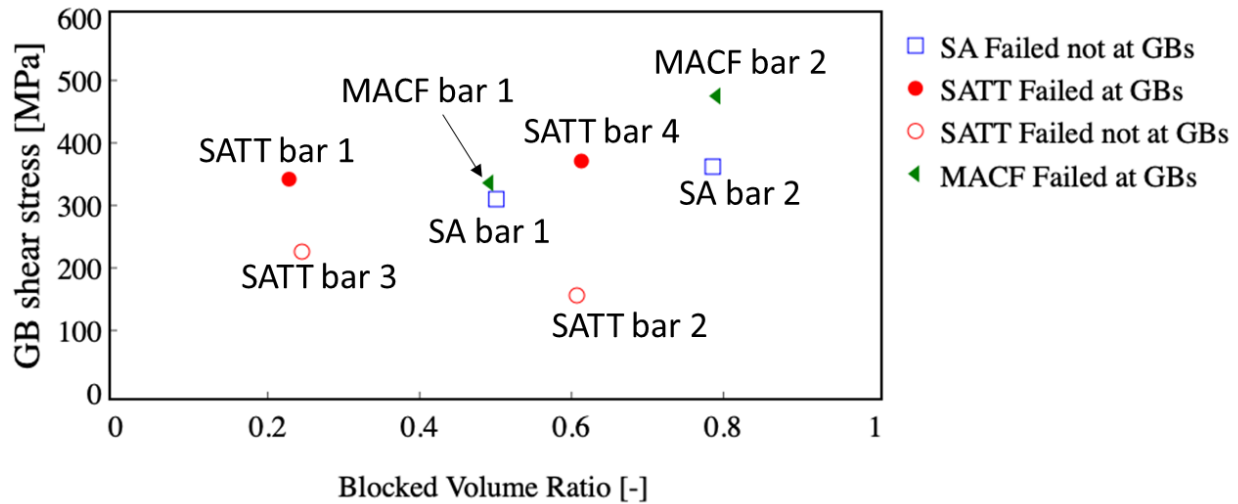
Figure 5-21. The grain boundary shear stress versus the blocked volume ratio

5.2.2.5. Conclusions and Future Work

This study successfully demonstrated the testing and analysis procedures for in situ SEM microtensile testing of oxidized grain boundaries. In situ SEM microtensile testing provides great control of experimental parameters (e.g., grain boundary orientation in 3D, grain boundary type, crystal orientations of adjacent grains). It enables the ability to explore the different parameters that influence the failure of oxidized grain boundaries. The testing and analysis procedures have been applied to Alloy 600 oxidized grain boundaries of three distinct thermal histories. The findings are expected to be useful in other important engineering alloys for corrosion studies. In particular, our study identified that the grain boundary shear stress plays a major role in causing grain-boundary oxide failure as compared to the grain boundary normal stress. Furthermore, the BVR parameter can be used to increase the amount of dislocation pile-up at the grain-boundary oxide, suppress "easy" slip band formation within the grains, and increase the maximum grain boundary shear stress achievable, which may enhance grain boundary failure.

6.1. Intermetallic Precipitates

In this section, we will investigate the effects of long-range-ordered (LRO) precipitates on plastic deformation. The effect of irradiation on LRO precipitates are investigated.

6.1.1. The effect of dose and dose rate on L1$_2$-, DO$_{22}$-structured precipitates in Inconel 718 – Mechanical and Characterization Study

6.1.1.1. Background

It was found that in high energy proton-irradiated Inconel 718, γ' and γ'' LRO precipitates become disordered at a very low dose (< 0.6 dpa) and gradually dissolved at a higher dose [59,62]. Additionally, Maloy et al. [62] showed that the uniform elongation drops below 2% at 0.5 dpa while the yield stress remains relatively unchanged and gradually decreases as the dose increases. The rapid disordering of LRO precipitates at low dose poses a question on the role of disordering on strain localization and embrittlement (reduction in uniform elongation and toughness) of Inconel 718. Therefore, the objective of this study is to investigate the effect of irradiation-induced disordering of the precipitates on the change in the deformation behavior Inconel 718 at the microscale.

The second important aspect of our study is to experimentally investigate the effect of dose rate on the disordering of the LRO precipitates in Inconel 718. Although neutron and high energy proton irradiation have been critical in assessing the irradiation damage in the structural components in their deployed state [61,62], they require extensive planning and long irradiation time. To accelerate the materials development cycle, heavy ion irradiation has been used as a surrogate irradiation technique to provide significantly higher dose rate [60,99,104]. However, previous studies have established that dose rate has a profound influence on the defect accumulation and the microstructure change [68,167,168]. It remains an important issue to address when using heavy ion irradiation to correlate with the neutron irradiation results [68,168]. The role of dose rate on the disordering of LRO precipitates in Inconel 718 nickel-based alloy has not been systematically explored; therefore, our study examines the effect of low dose heavy ion irradiation at two different dose rates on the stability of LRO precipitates of Inconel 718. Transmission electron microscopy (TEM) and atom probe tomography (APT) are utilized to observe the effect of disordering and dissolution of the heavy ion irradiation, respectively. In addition, in situ scanning electron microscopy (SEM) micropillar testing is utilized to measure the change in mechanical properties corresponding to the different irradiation conditions. We further explore the role of disordering of LRO precipitates on strain localization and provide insight on the rapid embrittlement of Inconel 718 at low irradiation dose.

6.1.1.2. Methods

A heat of Inconel 718 with the chemical composition listed in Table 6.1 underwent heat treatment under an inert atmosphere at 1065° C for 0.5 hr, then air cooled, followed by holding at 760 °C for 10 hrs and subsequent aging at 650 °C for 20 hrs, and finally air cooled to room temperature. The specimen was then irradiated at the Center for Accelerator Mass Spectrometry

(CAMS) in Lawrence Livermore National Laboratory. The alloy was irradiated by 70 MeV Fe ion at two different dose rates (2E-4 and 2E-5 dpa/s). For the rest of the manuscript, we refer 2E-4 dpa/s as high dose rate (HDR) and 2E-5 dpa/s as low dose rate (LDR). The irradiation temperatures for the HDR and LDR conditions are 290 °C and 295 °C, respectively. The dose profiles (dose versus depth) are calculated using SRIM (Stopping Range of Ions in Matter) with displacement energy of 40 eV, as shown in Figure 6.1.

Table 6.1. Composition of the Inconel 718 heat

Element	Al	C	Cr	Cu	Fe	Mn	Mo	Ni	P	S	Si	Ti	Others
Wt.%	0.54	0.05	18.13	0.05	Bal	0.21	3.01	52.7	0.005	0.002	0.13	1.06	Nb+Ta-5.07;Co-0.4;B-0.004
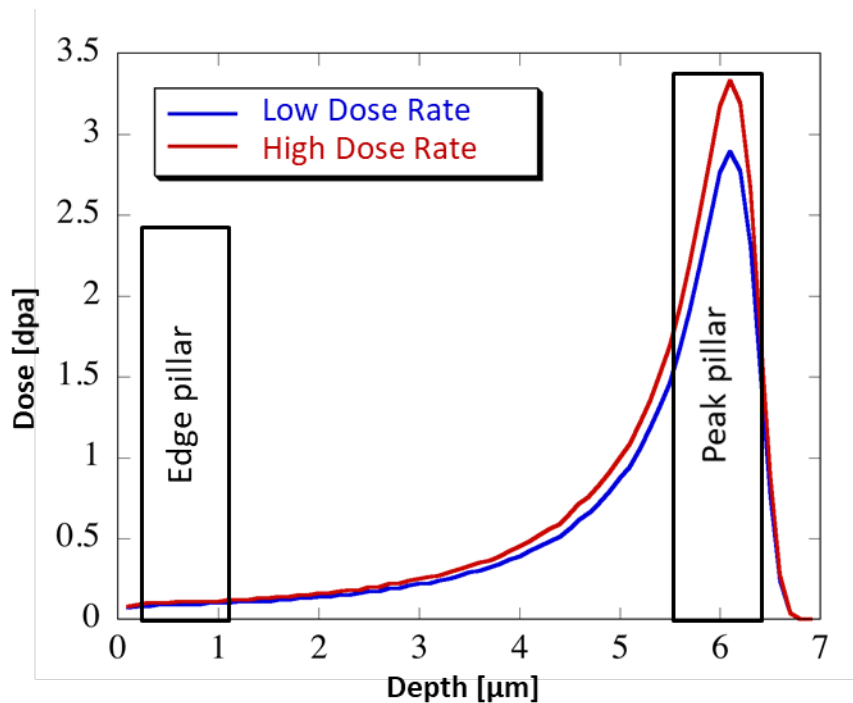
Figure 6-1 . Dose versus depth profiles of the LDR (1E-5 dpa/s) and the HDR (1E-4 dpa/s

The post-irradiation microstructure of the LRO γ′ and γ′′ precipitates were characterized by Transmission Electron Microscopy (TEM). The TEM lamellae were made along the direction of the irradiation so the effect of the full dose profile can be examined. The lamellae of the HDR and LDR conditions were lifted out and prepared with the FEI Quanta 3D dual-beam scanning electron microscope (SEM)/focused ion beam (FIB). The LRO precipitates were characterized using selected area electron diffraction (SAED) and dark-field (DF) TEM to record the influence of irradiation on the disordering of the LRO precipitates. A FEI Tecnai F30, operated at accelerating voltage of 300 kV, were employed to record the microstructures.

Atom probe tomography (APT) analyses were then performed at the edge dose (~0.1 dpa), the peak dose (~3.33 and ~2.9 dpa for HDR and LDR, respectively), and the unirradiated condition for both HDR and LDR samples. The edge dose refers to the early part of the dose profiles (Figure 1A) that corresponding to ~0.1 dpa. The peak dose refers to the highest dose achieved in the dose profiles and corresponds to ~2.9 dpa for LDR and ~3.3 dpa for HDR. The APT is performed using laser mode with laser energy of 1 nJ and 200 kHz pulse frequency at 45 K. The morphologies of LRO γ' and γ'' precipitates are characterized as a function of dose and dose rate using spherical equivalent radius method in the IVAS (Integrated Visualization Analysis Software) software.

Finally, the FEI Quanta 3D dual-beam SEM/FIB was utilized for the fabrication of the micropillars and the in situ micromechanical testing. The micropillars have a square sectional area of (~1 μm x ~1 μm) and height of ~2 μm. The micropillars are fabricated at the edge location (~ 0.1 dpa), peak location (~0.146- ~2.9 dpa for LDR and ~1.69-~3.33 dpa for HDR), and unirradiated condition in both HDR and LDR samples. The corresponding dose range for the edge micropillars and peak micropillars are indicated in the dose profile schematics Figure 6.1. The rough FIB removal was performed at 2 nA and 30 KeV and the final FIB cleaning was done at 0.3 nA and 16 keV. The detailed procedure is reported in [103]. The microcompression was performed *in situ* SEM using a Hysitron PI-88 Picoindenter. The tests were performed using displacement control at a strain rate of 2×10^{-3} s^{-1}

6.1.1.3. Results and Analysis
6.1.1.3.1. Transmission Electron Microscopy

The <101> zone axis SADPs of the LDR and HDR conditions are taken along the dose versus depth profile (Figure 6.1) at the edge, peak, and unirradiated locations, as shown in Figure 6.2. In both dose rate samples, the superimposed superlattice reflections of the γ' and γ'' LRO precipitates are observed in the unirradiated locations; and they decrease in intensity with increasing dose. For a given dose, the intensity of the superlattice reflections is lower in the HDR sample as compared to the LDR sample. It is most evident when comparing the intensity of the superlattice reflections of the LDR peak (Figure 6.2B) and LDR peak (Figure 26.E) as the superlattice reflection spots are not visible in latter compared to the former. To better visualize the disordering effect at different irradiation conditions, darkfield TEM is then performed using the 2-beam condition with the superlattice reflection selected to show the LRO precipitate distribution.
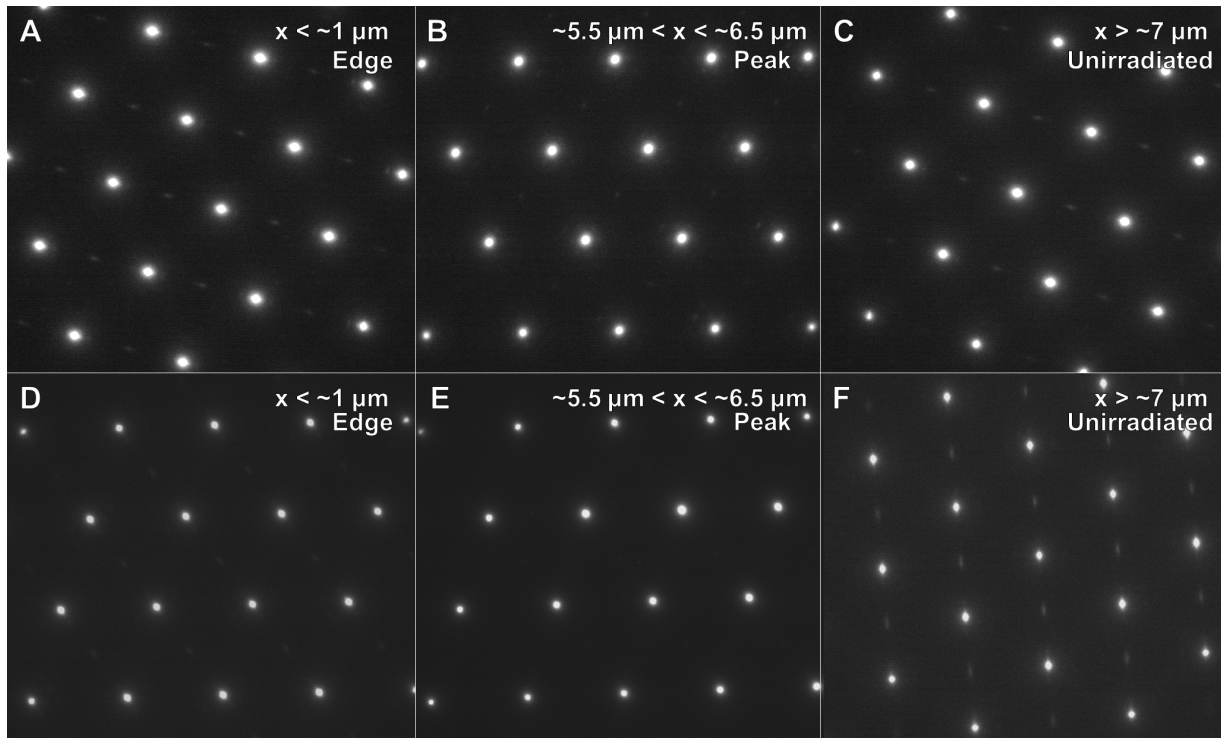
Figure 6-2. Selected area diffraction patterns of the LDR (A) edge, (B) peak, (C) unirradiated locations and the HDR (D) edge, (E) peak, and unirradiated locations. The approximate location with respect to the dose versus depth profile is indicated for each SAED.

The DF TEM images, in Figure 6.3, show the distribution of the ordered γ' and γ'' precipitates as a function of dose and dose rate. As the dose increases, the portion of the ordered precipitates decrease in size and density. In the HDR condition, the LRO precipitates become disordered at a faster rate compared to the LDR condition. This observation is evident when comparing the DF TEM images of the peak dose region (1.46-3.33 dpa) of the dose rates, the LRO precipitates are no longer visible in the HDR condition in contrast to the more visible defect distribution in the LDR sample. The TEM observations provide a novel qualitative observation that the disordering rate of LRO precipitates in Inconel 718 is proportional to dose and dose rate. However, we acknowledge the need for further quantification of the change in ordered parameter in order to calibrate and develop more comprehensive dose rate dependent disordering model. To examine the effect of dose and dose rate on the dissolution of the LRO precipitates, APT was performed and presented in the following section.
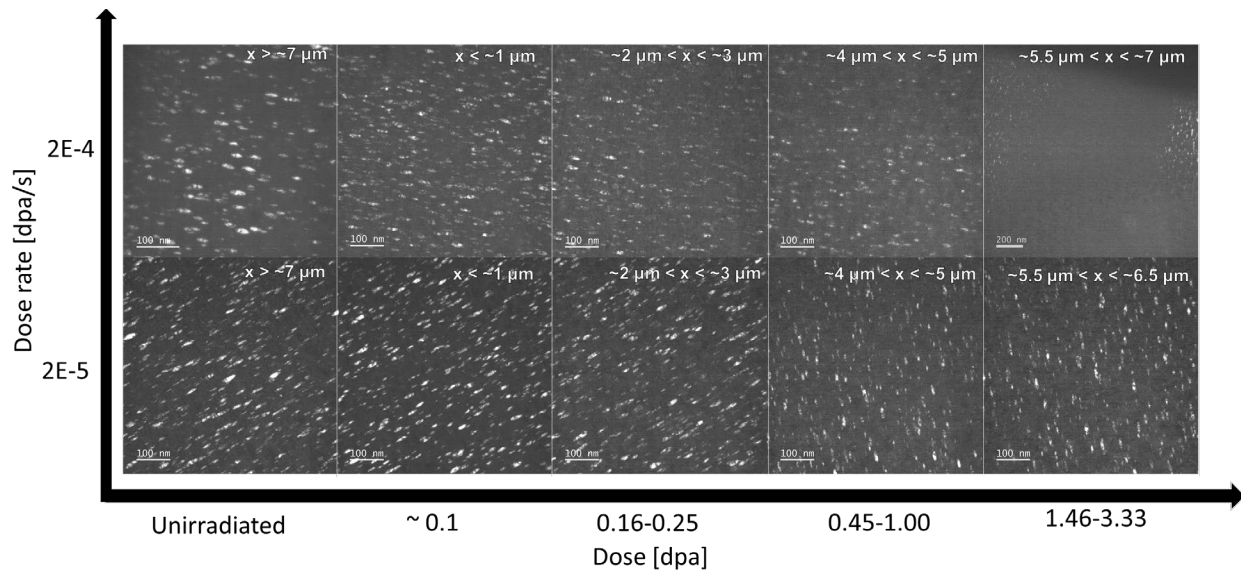
Figure 6-3. The dark field TEM images showing the LRO γ' and γ'' precipitates as a function dose rate and dose. The approximate location with respect to the dose versus depth profile is indicated for each DF TEM image.

6.1.1.3.2. Atom probe tomography

Figure 6.4A shows the iso-surface reconstruction of the γ' $Ni_3(Al,Ti)$ and γ'' (Ni_3Nb) in the unirradiated condition. Consistent with previous literature [59], the γ' precipitates take on disk shape and the γ'' precipitates are spheroidal or disk-shaped. The γ' and γ'' precipitates have been identified using iso-surface construction by choosing threshold values of 9% and 12% for (Al+Ti) and Nb, respectively. Across all ion irradiation dose and dose rate, dissolution of both LRO precipitate types were observed and it increases with increasing dose. In the highest dose and dose rate condition (figure 6.4B), the γ' and γ'' precipitates largely remain as (Al,Ti) and Nb-rich aggregates, respectively, although the precipitates have been mostly (if not completely) disordered as indicated by the DF TEM image (Figure 6.3). This observation is consistent with other proton and heavy ion irradiation studies indicating that significant dissolution only takes place at a much higher dose in other nickel-based alloys [60]. The size, number density, and volume fractions of the γ' and γ'' are quantified and plotted in Figure 6.5.
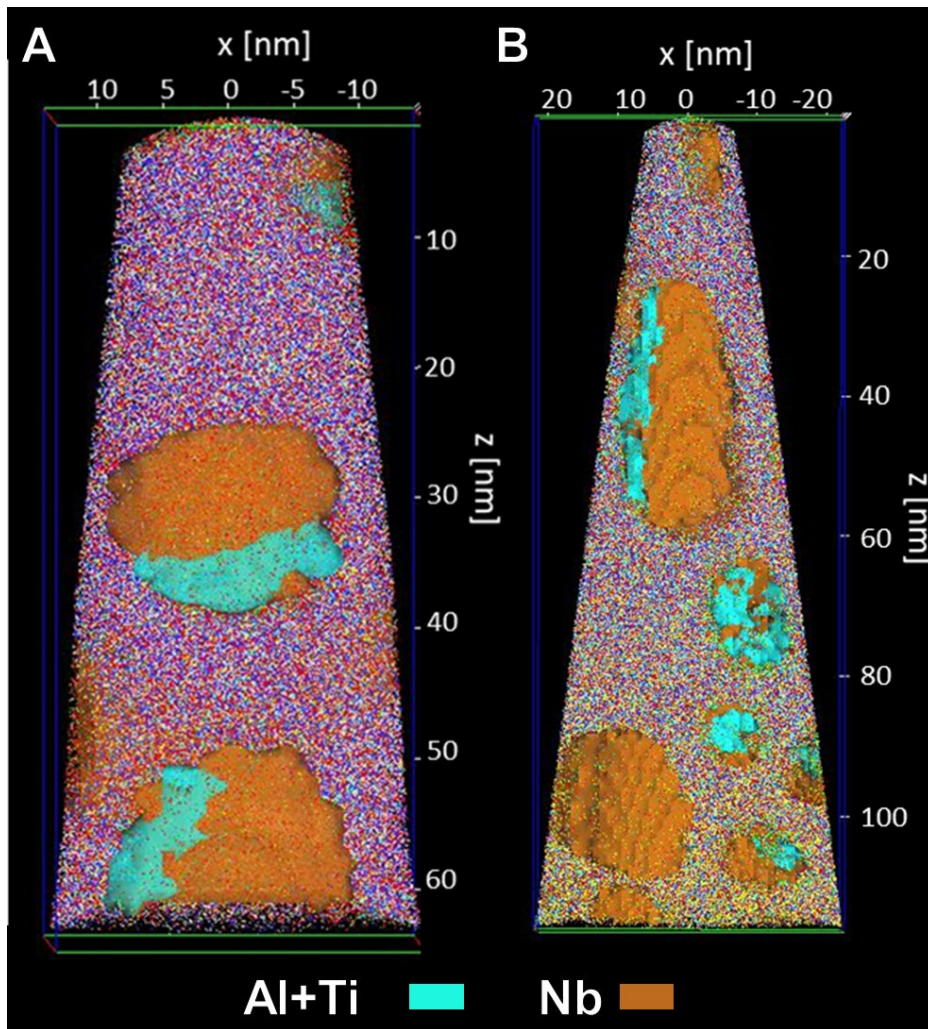
Figure 6-4. APT reconstruction showing the γ' and γ'' precipitates in the (A) unirradiated and the (B) HDR peak condition. The γ' and γ'' precipitates are colored cyan and brown, respectively.

Since 2-3 APT tips of each condition (dose, dose rate) were sampled, the plots in Figure 5 serve as a rough estimate of the effect of dose and dose rate on the precipitate distribution and size. For both precipitate types, the ion irradiation does not strongly affect the precipitate size (figures 5A and 5B); although there is a slight decrease in the average diameter of γ'' compared to γ' as a function of dose. On average, the volume fraction and the number density of both LRO precipitates are decreased after the ion irradiation conditions (figures 5C-5F). The difference between the HDR and LDR conditions are not substantial in the γ' Ni$_3$(Al,Ti) precipitates and slightly more pronounced in the γ'' Ni$_3$Nb precipitates. The data here suggests that dissolution has taken place however the effect of dose rate on dissolution is not clearly observed as compared to the influence of dose. The interesting insight is that the size of the precipitates remain relatively unchanged.

75
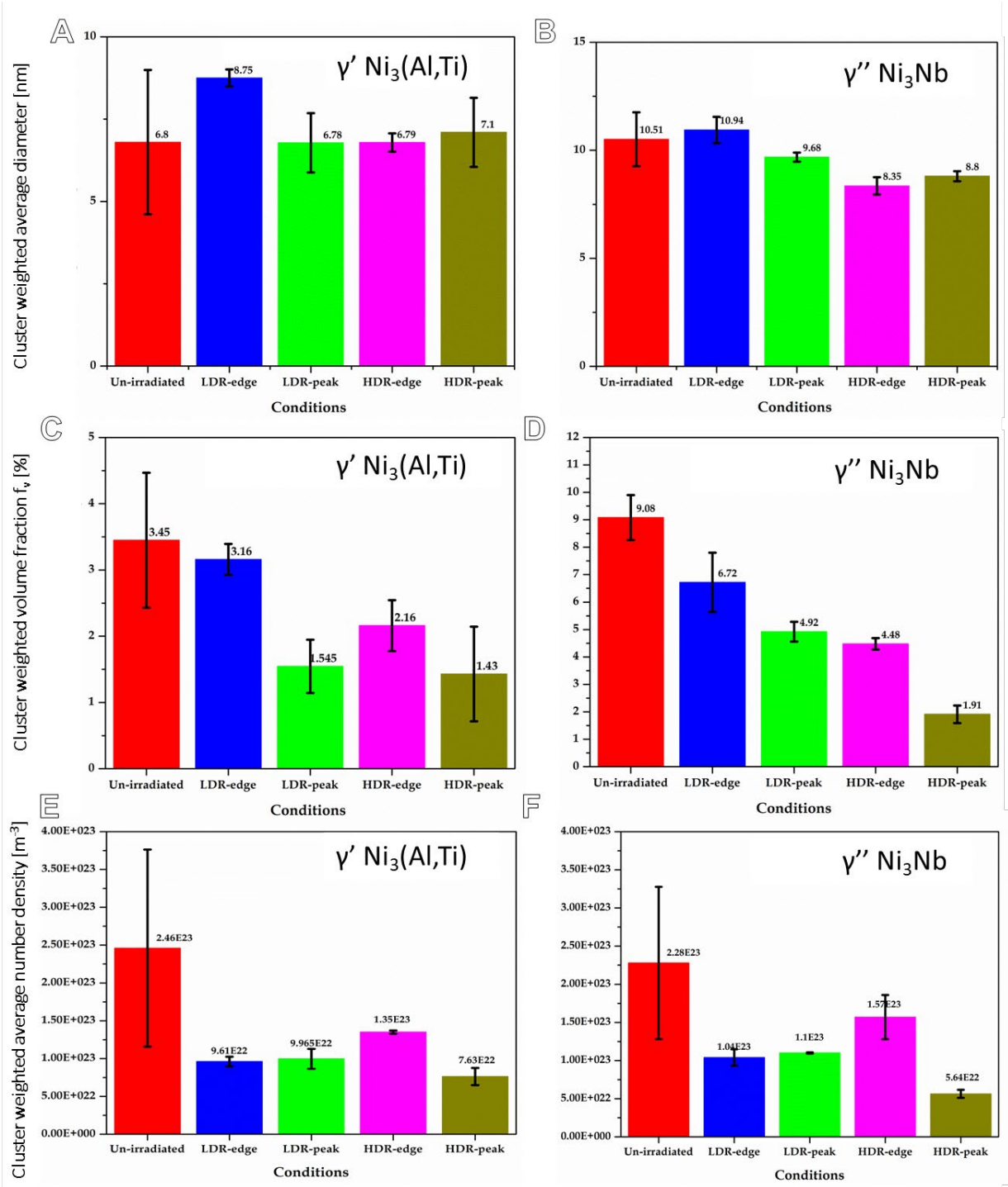
Figure 6-5. (A),(B) Cluster weighted average diameter versus irradiation condition plots. (C),(D) Cluster weighted volume fraction versus irradiation condition plots. (E),(F) Cluster weighted average number density versus irradiation condition plots

6.1.1.3.3. In situ SEM micromechanical testing

Two sets of micropillars were tested for the HDR and LDR samples. The HDR micropillars were compressed along the <100> zone axis and the LDR <111> zone axis respectively. The resolved shear stress values are calculated using Schmid's law (included in the Supplementary section). The stress-strain curves of the all tests are included in Figures 6.6 and 6.7, respectively.
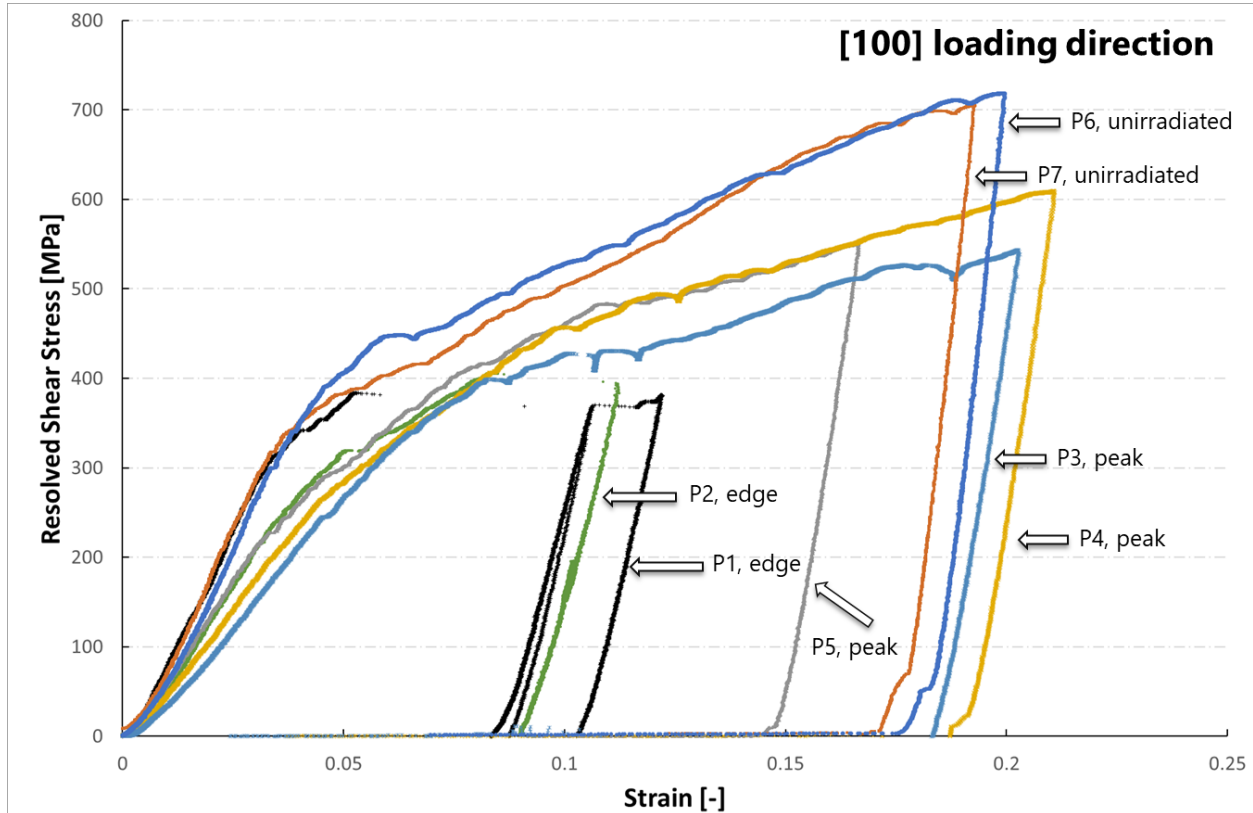
Figure 6-6. Stress versus strain plot for HDR pillars
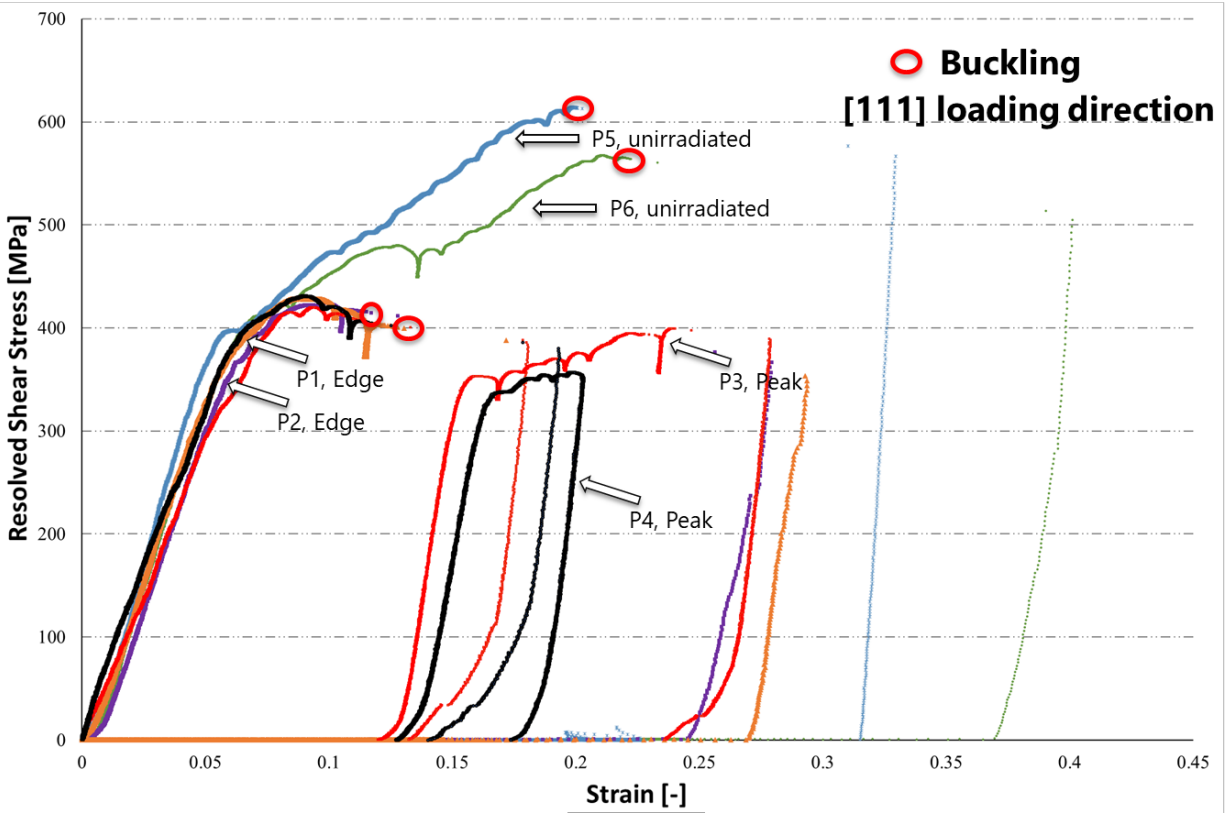
Figure 6-7. Stress versus strain plot for LDR

The one percent yield stress values are calculated, and the corresponding average CRSS values of all the conditions are plotted in Figure 6.8. The CRSS values of the unirradiated condition in the HDR and LDR samples are similar to establish a reference point. Interestingly, the CRSS values remain relatively unchanged in the LDR edge and LDR peak conditions. In contrast, the CRSS value decrease by ~50 MPa in the HDR edge condition and stayed a similar value in the HDR peak condition. This observation is consistent with bulk uniaxial tensile testing of the high energy proton irradiated Inconel 718 [62], where a minor decrease in YS at the very low dose was observed, followed by the increase in YS as the dose increases, and a subsequent gradual decrease in YS at the high dose. An intuitive explanation for such trend roots in the competition between the disordering effect, the dissolution effect, and the buildup of irradiation-induced loops. In the HDR edge condition, the decrease in the CRSS accounts for the nonnegligible disordering effect of the LRO precipitates which reduces the strengthening of the ABP mechanism. In the HDR peak condition, the buildup of the irradiation-induced loops (vacancy and interstitial loops) offset with the continued decrease in the precipitates' order thus the CRSS remains similar to the HDR edge condition. In the LDR edge condition, the disordering effect is not significant enough to lead to a distinguishable in CRSS value. As the disordering increases in the LDR peak condition, the build-up of irradiation-induced loops is enough to offset the disordering effect similar to the HDR condition. In the following section, the effect of disordering on the plastic flow behavior is discussed.

78
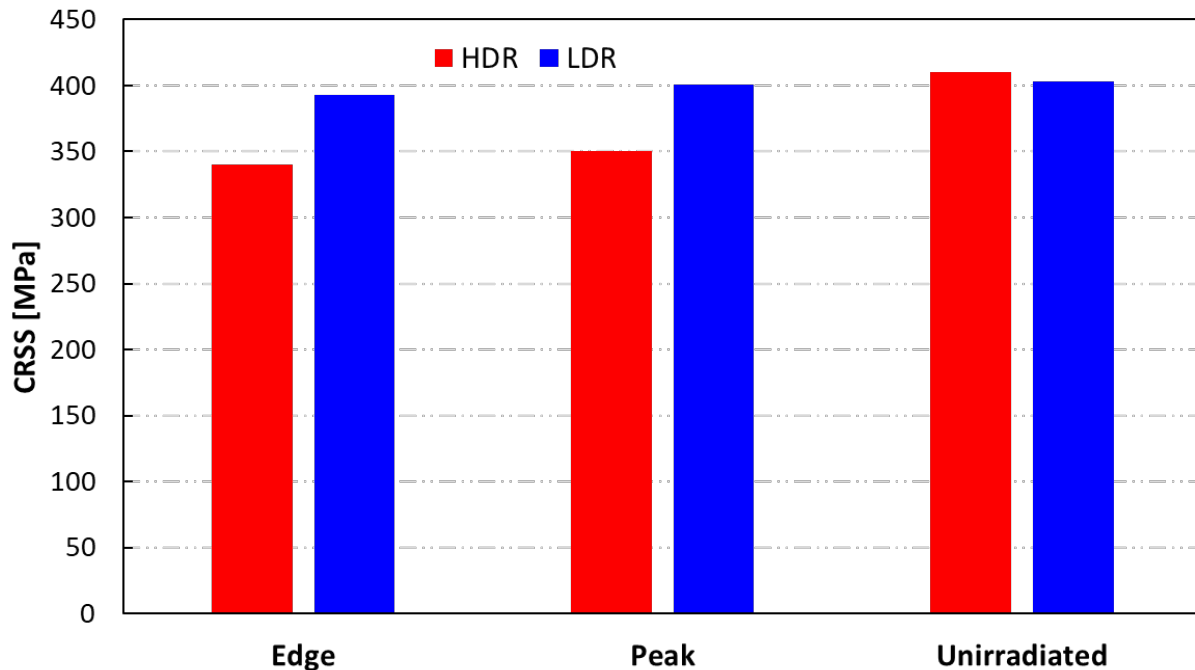
Figure 6-8. Average CRSS values of the edge, peak, and unirradiated conditions of the HDR and LDR samples

6.1.1.4. Discussion

6.1.1.4.1. Influence of low dose disordering effect on the plastic localization

As mentioned in previous section, Maloy et al. [62] presented bulk tensile testing of Inconel 718 irradiated with high energy proton from 0.02 to 11. 4 dpa. With the permission and data provided by the corresponding author Dr. Stuart Maloy, Figure 6.9 plots the uniform elongation and total elongation of the bulk tensile tests as a function of dose. The most notable observation is the drastic decrease in uniform elongation at a very low dose. The UE decreases below 5% at 0.1 dpa. As consequence, the alloy's fracture toughness also significantly decreases. To gain microscopic insight on the loss in toughness as well as uniform elongation at very low dose (~0.1 dpa), we examine the flow stress and the deformation behavior of the micropillars in the unirradiated and HDR edge (~0.1 dpa) conditions. Figure 6.9B shows the comparison of the resolved shear stress-strain curves between the two conditions. Figures 6.9C and 6.9D show the corresponding SEM images of the deformed micropillars in the HDR edge condition and the unirradiated condition, respectively. In the unirradiated condition, the flow stress is stable with a clear strain hardening response. Multiple widely-spaced slip steps are formed, as shown in Figure 6.9D. In contrast, the slip in the HDR edge condition is composed of fewer localized slip steps. Additionally, there is a lack of strain hardening, accompanied by a severe strain burst (Figure 6.9B). Since the PI88 picoindenter is inherently load controlled, the transducer uses the feedback loop to maintain a constant displacement for displacement-controlled tests. When a sudden deformation takes place, the feedback loop is not fast enough to follow the displacement, resulting in a load drop and a strain jump. When the indenter catches up with the displaced micropillar, the load and displacement resume recording.
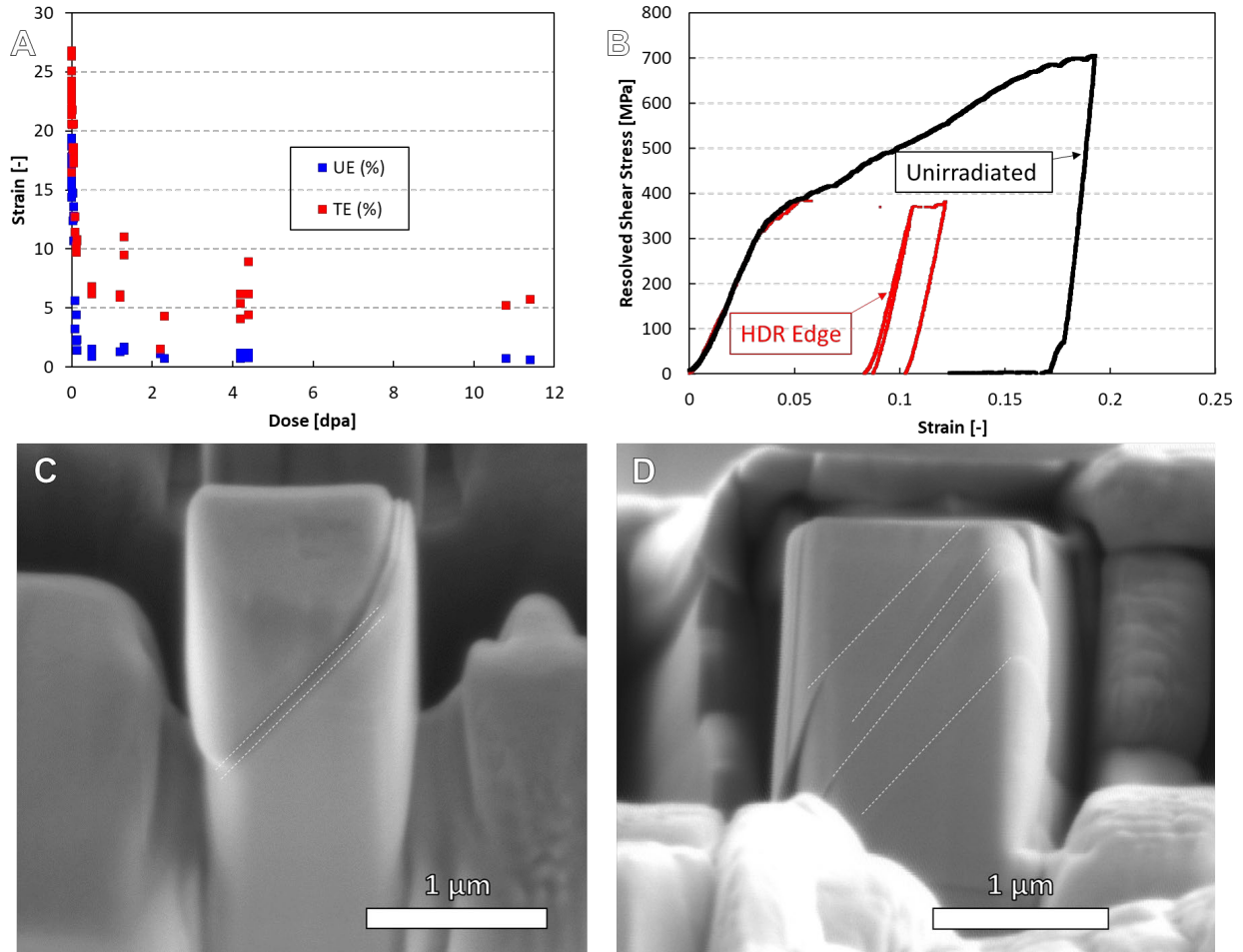
Figure 6-9. (A) The UE and TE versus dose plot. (B) the resolved shear stress versus strain of the HDR edge and unirradiated conditions in the HDR sample. (C),(D) the corresponding SEM images of the deformed HDR and unirradiated micropillars, respectively

To rationalize the strain burst and connect it to strain localization (plastic instability), we examine the interaction of the dislocations and the LRO precipitates in the unirradiated and partially ordered precipitate (HDR edge condition). Figure 6.10A presents the 2D schematic of the dislocation pair of slip system $(111)[10\bar{1}]$ and a single layer LRO γ' structure, looked along the $[1\bar{2}1]$ direction. As mentioned in the introduction, the dislocations prefer to travel in pairs when shearing LRO γ' precipitates [42], because it requires a displacement of two perfect Burger vectors to shift Ni atoms and Al (or Ti) atoms to their respective lattice sites to maintain the order, as indicated in Figure 6.10A.
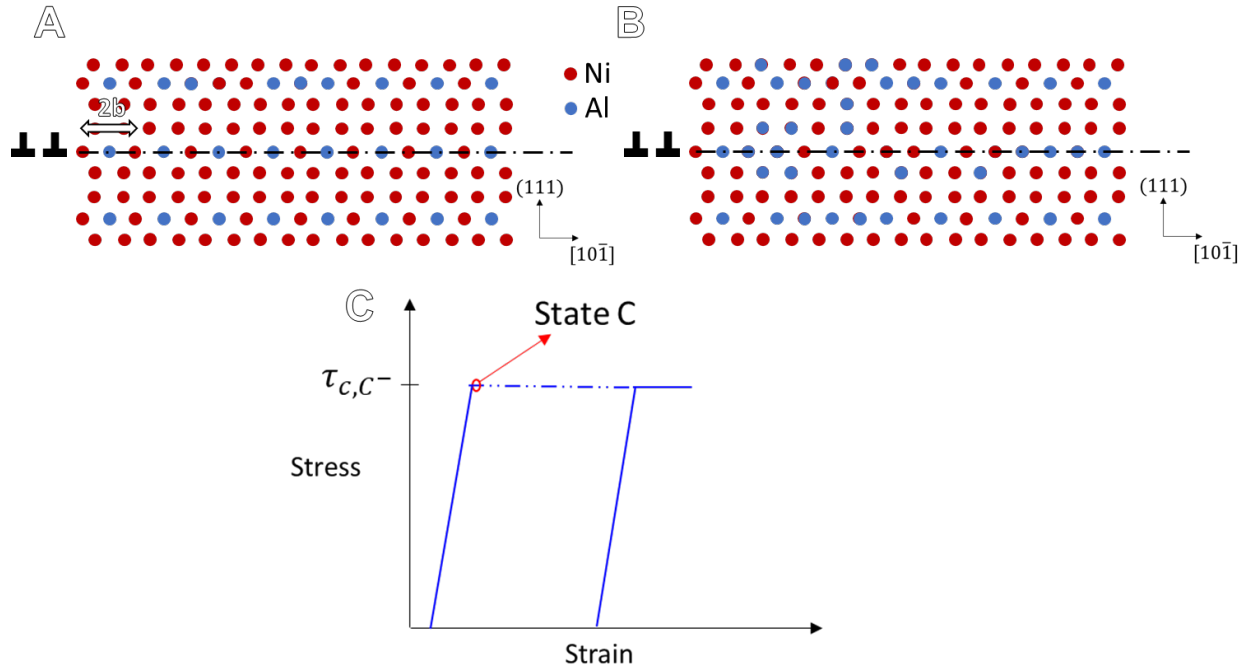
Figure 6-10. 2D schematics of the dislocation pair of slip system $(111)[10\bar{1}]$ and a single layer LRO γ' structure, looked along the $[1\bar{2}1]$ direction in (A) the unirradiated condition and (B) the partially disordered condition. (C) Schematic of the stress-strain curve with a strain burst event.

As the result of the irradiation process, some part of the LRO precipitates becomes disordered due to the disordering effect. A simple schematic of the LRD precipitate structure, representing the partial disorder in the LRO precipitate after the irradiation is shown in Figure 6.10B. In the partially disordered condition, a shift of two perfect Burger vectors via the dislocation pair does not necessarily maintain the order of the precipitate on the particular glide plane; because Ni atoms and Al (or Ti) atoms do not necessarily go back to the corresponding lattice sites. As a consequence, the dislocations shear through the LRO precipitates, leaving behind a disordered glide plane. Equation 6.1 outlines a simple equation for the critical shear stress required to shear through a LRO precipitate, derived from the line tension equation [49].

$$\tau_c = \frac{d\gamma_{APB}}{Lb} \qquad Eq.\ 6.1$$

Where L: dislocation length, b: Burger's vector, d: diameter of the ordered precipitate, γ_{ABP}: ABP energy, τ_c: critical shear stress required to shear the precipitate

The equation (1) shows that τ_c is expected to decrease as the LRO precipitate's size (d) decreases, which is consistent with our experimental observation in the HDR edge condition. The precipitate becomes locally disordered, the precipitate's dislocation resistance is significantly reduced on the particular glide planes. We then utilize several constitutive relations to understand how a sudden loss in dislocation resistance leads to severe strain burst in the stress-strain curve and vice versa. In a single crystal micropillar, the shear strain rate on a slip plane is given by the Orowan's relation as:

$$\dot{\gamma} = b\rho v \qquad Eq.\ 6.2$$

Where $\dot{\gamma}$: shear strain rate, ρ: dislocation density on the glide plane, v: dislocation velocity

We denote point C to be the moment when the shear stress reaches τ_c and the strain burst takes place, as shown in the schematic stress-strain curve in Figure 8C. As a result of the strain burst there must be an instantaneous change in the shear strain rate $\dot{\gamma}$. Following equation 2, the dislocation velocity must increase abruptly as the other terms are expected to remain unchanged. In the present of precipitates as the dominant defect type, the average glide velocity can be expressed as [169,170]:

$$v = \frac{\lambda}{t_t + t_w} \qquad Eq.\ 6.3$$

where t_t : transverse time, t_w: waiting time, λ: mean spacing of the LRO precipitates

t_t traverse time is the time required to travel between the LRO precipitates which can be estimated using the mobility relation [169]:

$$t_t = \frac{\lambda B}{b|\tau_{applied} - \tau_R|} \quad Eq.\ 6.4$$

Where B: drag coefficient, $\tau_{applied}$: applied shear stress, and τ_R : lattice resistance

Lastly, the t_w waiting time is the time required to activate shearing (or bypassing) of the LRO precipitates. It can be described by the Kocks-type stress dependent activation enthalpy equation as [171]:

$$t_w = A\ exp\left(-\frac{\Delta G}{kT}\right) = \ Aexp\left(-\frac{1}{kT}f\left(\frac{\tau_{applied}}{\tau_c}\right)\right) \quad Eq.\ 6.5$$

Where A: constant, ΔG : function of $\left(\frac{\tau_{applied}}{\tau_c}\right)$, k: Boltzmann constant, and T: temperature term

At the point C, equation 3 indicates that in order to have a drastic increase in dislocation glide velocity, the waiting time t_w and/or transverse time t_t have to be reduced significantly. Following equation 4, the traverse time is not expected to be decreased as the applied shear stress does not increase and other parameters remain constant; therefore, the waiting time has to be reduced in order to have an instantaneous increase in the glide velocity. As described in equation 5, the waiting time can be decreased if the critical shear stress (e.g. the strength of the LRO precipitate) decreases. Following the equations 6.1-5, the instantaneous increase in the shear strain rate (or strain burst) in a given slip plane requires a substantial decrease in the strength of the LRO precipitates on the particular slip plane. In other words, the observation of the strain burst indicates that the dislocation pair mechanism no longer retains the precipitate's order, leading to strain localization. Important to note that in the micropillars that do not contain a dense distribution of defects (precipitates, dislocations, or voids etc...), strain bursts can be manifested due to dislocation avalanches and size effect [84]. In the presence of dense precipitate distribution, the strain burst related to size effect are minimized as the defect mean spacing is much smaller than the dimensions of the micropillars. Therefore, the strain burst observed in the partially disordered condition is an indication of the unstable dislocation-precipitate interaction. The conceptual analysis reveals an interesting insight, which is disordering-induced strain localization takes place at a much lower dose compared to strain localization induced by irradiation induced loops. Since Von Mises criterion requires at least five independent slip

systems to accommodate for any plastic strain tensor and ensure a ductile deformation behavior within a polycrystalline material [78], strain localization limits the number of active independent slip systems, thus limiting strain hardening. Therefore, the low dose disordering effect of LRO precipitates play an important role of the rapid reduction in bulk scale uniform elongation and fracture toughness in irradiated Inconel 718 as shown in figure 6.9A.

6.1.1.4.2. The effect of dose rate on the disordering and dissolution of LRO precipitates

Various theories [64–66] on the effect of dose rate have been explored and developed to account for different radiation-related processes . K. Liou and P. Wilkes have proposed an irradiation-induced disordering model for ordered alloys, that account the effect of irradiation dose rate and temperature on the steady state long range order parameter, which describes the degree of ordering of an ordered phase. The details of the formulation are shown in [66]. The rate equation for describing the change in ordering is written as:

$$\frac{dS}{dt} = \left(\frac{dS}{dt}\right)_{Irr} + \left(\frac{dS}{dt}\right)_{Th'} \quad Eq.\ 6.6$$

Where S: long range order parameter, $\left(\frac{dS}{dt}\right)_{Irr}$: the disordering rate induced by the radiation cascade, $\left(\frac{dS}{dt}\right)_{Th'}$: the radiation enhanced thermal reordering rate.
The disordering rate is given as:

$$\left(\frac{dS}{dt}\right)_{Irr} = -\epsilon k S \quad Eq.\ 6.7$$

Where ϵ: disordering efficiency depending on the types of irradiation (heavy ion, neutron, electron, etc), k: dose rate
The radiation enhanced reordering rate is given as:

$$\left(\frac{dS}{dt}\right)_{Th'} = \frac{x(1-S)^2}{(1-S_e)} - (1-S_e)x \quad Eq.\ 6.8$$

Where S_e: equilibrium order parameter in the absence of irradiation, calculated from order-disorder transition theory, x: rate constant.
The rate constant x takes into account the concentration of point defects (interstitial and vacancy), atomic fractions of each element in the ordered phase, and temperature. By solving the rate equation 6.6, K. Liou and P. Wilkes [66] showed that for a given dose, the steady state order parameter of an ordered alloy is lower when irradiated at higher dose rate. It is because the disordering rate is directly proportional with the dose rate k, whereas the reordering rate is thermally dependent and enhanced by the irradiation as it increases the steady state point defect concentrations. In order words, the dose rate has a stronger influence on the disordering rate as compared to the ordering rate in the rate equation. In future work, we emphasize the need to obtain quantitative ordering parameter as a function of dose rate in order to help validate and calibrate the existing dose rate model.

6.1.1.5. Conclusion

In this study, we examined the effect of dose and dose rate on the LRO precipitates and the corresponding mechanical properties in Inconel 718 nickel-based alloy by using a range of experimental methods. The advances made in this work are summarized as followed:

1. TEM results show that the irradiation-induced disordering of LRO precipitates is proportional to both dose and dose rate. In the high dose rate condition, the nonnegligible disordering was observed as early as ~0.1 dpa and complete disordering was observed above ~1.69 dpa. In the low dose rate condition, the LRO precipitates are still visible at the highest dose condition of ~2.9 dpa.
2. As confirmed by APT, dissolution was observed through the entire dose profile in both dose rate conditions. The observation is also consistent with previous literature, indicating that disordering effect is dominant at the low dose regime.
3. In situ SEM micropillar testing was performed on all conditions. Rapid decrease in yield stress and significant strain burst were observed for the 0.1 dpa HDR condition. An explanation for the role of low dose disordering effect on inducing strain localization and loss in uniform elongation at the macroscale is provided.

6.1.2. Influence of Pt$_2$Mo-structured Precipitates on Deformation Mode (Slip versus Twin) in Ni-based Alloy
6.1.2.1. Background

Background regarding Pt$_2$Mo-structured Precipitates in Nickel-based alloys have been provided extensively in Section 1.3.4.2.

6.1.2.2. Theory and Methodology
6.1.2.2.1. Crystallographic analysis of the relationship between Pt$_2$Mo-structured precipitates and the matrix slip systems

Previous studies have investigated the crystallographic relationship between the FCC slip systems of the matrix and the LRO Ni$_2$(Cr,Mo) precipitate structure [43,71,72]. Figure 6.11 outlines such relationship. As mentioned in these studies, the outcome of the dislocation-LRO precipitate interactions depends on the geometry of the configuration. Following [43,71,72], we define two types of crystallographic configurations. Type 1 describes the situation in which a shift of a matrix dislocation by a perfect Burger's vector on a particular slip system maintains the ordered precipitate structure while type 2 does not; thereby creating an APB. As noted in Figure 1, slip systems $(\bar{1}1\bar{1})[110]$ are $(1\bar{1}\bar{1})[110]$ belong in Type 1, and slip systems $(111)[\bar{1}01]$, $(111)[0\bar{1}1]$, $(111)[1\bar{1}0]$, $(\bar{1}\bar{1}1)[011]$, $(\bar{1}\bar{1}1)[\bar{1}10]$, $(\bar{1}\bar{1}1)[101]$, $(1\bar{1}\bar{1})[0\bar{1}1]$, $(1\bar{1}\bar{1})[101]$, $(\bar{1}1\bar{1})[011]$, $(\bar{1}1\bar{1})[\bar{1}01]$ belong in type 2.

Type 1	Type 2
Example: (-11-1)[110]	Example: (111)[-101]

Type 1: $(\bar{1}1\bar{1})[110]$, $(1\bar{1}\bar{1})[110]$

Type 2: $(111)[\bar{1}01]$, $(111)[0\bar{1}1]$, $(111)[1\bar{1}0]$, $(\bar{1}\bar{1}1)[011]$, $(\bar{1}\bar{1}1)[\bar{1}10]$, $(\bar{1}\bar{1}1)[101]$, $(1\bar{1}\bar{1})[0\bar{1}1]$, $(1\bar{1}\bar{1})[101]$, $(\bar{1}1\bar{1})[011]$, $(\bar{1}1\bar{1})[\bar{1}01]$,

Legend:
[001], [010], [100] — Matrix Reference Coordinate
- Cr (red)
- Ni (blue)
- Random of Ni or Cr (dashed)
- Slip Plane (red triangle)
- Burger direction (black arrow)
- Leading Partial Direction (purple dashed arrow)
- Trailing Partial Direction (green dashed arrow)

Figure 6-11. Type 1 and type 2 configurations. There are 2 slip systems and 10 slip systems that are type 1 and type 2, respectively

In type 2, the individual movement of the leading and trailing partials typically do not disrupt the ordered structure, while the combined movement of both leading and trailing partials would cause the disorder. It is logical to hypothesize that the ordered precipitate structure serves as a pinning site for trailing partial in type 2 because the sweeping of the trailing dislocation through the precipitate would generate an APB. Therefore, previous studies have suggested that it is more energetically favorable to twin than slip in 10 of the 12 FCC slip systems, *i.e.* for the type 2 configuration, to explain the dominant deformation twinning in bulk scale mechanical tests [43,70,72]. In contrast, slip is expected to be more favorable in type 1 as no ABP is created after precipitate shearing. In our work, molecular dynamics was performed to examine the differences in type 1 and type 2 interactions. Additionally, all previous studies were performend on polycrystalline bulk materials which do not allow direct observation of the phenomena and where complex stress states within a grain may exist [43,70,72]. Therefore, microcompression testing was performed here to activate type 2 interaction in single-crystal micropillars, containing Pt_2Mo-structured precipitates. Interestingly, we found that type 2 interaction does not always activate deformation twinning which was not reported in previous studies. The role of the resolved shear stress on the dislocation partials play a big role in the resulted deformation mode in type 2 interaction. Lastly, molecular dynamics was performed to examine the twin formation process from thermodynamics perspective.

6.1.2.2.2. Materials Preparation

A Ni_2Cr binary alloy was produced by small batch arc-melting, followed by hot-rolling, and homogenized for 24 h at 1093 °C. One batch of the Ni_2Cr alloy was aged inside the furnace at 475°C for 10,000 h. To accurately monitor the temperature, three thermocouples were placed

around the samples and monitored throughout the aging process. The full detail of the material fabrication and aging process is reported in [172]. The aging process was performed to induce precipitation of Ni$_2$Cr LRO precipitates with body-centered-orthorhombic crystal structure, as shown in Supplementary Figure 1. The orientation relationship between the LRO Ni$_2$Cr precipitate and the Ni$_2$Cr disordered face-centered cubic (FCC) matrix is characterized as (002)$_{matrix}$ // (010)$_{precipitate}$ and [010]$_{matrix}$ // [103]$_{precipitate}$. A detailed TEM characterization of the orientation relationship (OR) of the Ni$_2$Cr type precipitate and the Ni-based matrix is reported in [173].

6.1.2.2.3. Molecular Dynamics Simulations

Using LAMMPS [174], the molecular dynamics (MD) simulation work consists of two parts. The first part examines the interaction between a single dislocation and a Pt$_2$Mo-structured precipitate for the type 1 and type 2 interactions. The role of the resolved shear stresses acting on the dislocation partials is also examined in these simulations. For this study, the angular-dependent potential (ADP) for Ni-Cr system developed by Howells and Mishin is utilized since it can capture the elastic constants, lattice spacing and defect energies (stacking fault energies) of both individual elements and binary alloys [175]. OVITO is used to visualize all of the MD results [176]. As shown in Figure. 6.12, a spherical LRO Ni$_2$Cr precipitate is placed at the center of the simulation cell and surrounded by disordered FCC Ni$_2$Cr matrix atoms. The LRO Ni$_2$Cr precipitate is generated by rotating atoms within a defined spherical region to the body-centered tetragonal (BCT) crystal structure according to the OR shown in Figure. 6.11. The matrix atoms are randomly generated using the FCC lattice while maintaining the stoichiometry of 2:1 for Ni and Cr atoms. An edge dislocation dipole is introduced with use of the displacement field of a dislocation shear loop [177–179]. Since the initial displacement field does not describe properly the dislocation core structure, energy minimization via a nonlinear conjugate gradient method is performed to relax the core structure after inserting the dislocation. The system is then brought to thermodynamic equilibrium at 10 K using a Nose-Hoover style thermostat and barostat [180]. This dislocation is then driven towards the precipitate under different applied shear stresses.
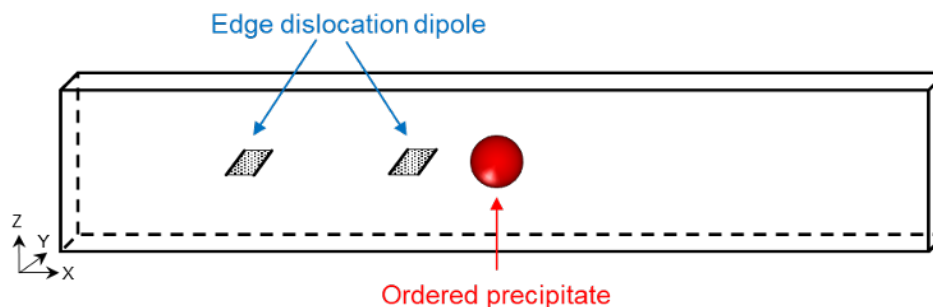
Figure 6-12. Simulation cell with an edge dislocation dipole and an ordered Ni$_2$Cr precipitate

The simulation cell is oriented such that the X, Y, and Z axis are in the <101>, <121>, and <111> directions, respectively. Periodic boundary conditions are used in all 3 directions. The simulation

cell is approximately $302.0 \times 12.2 \times 49.2$ nm^3 in X, Y, and Z directions and contains about 16 million atoms. The X dimension is much longer than the other two dimensions to minimize the effects of the dislocation dipole self-interaction. Two different slip systems $[110](\bar{1}1\bar{1})$ and $[101](1\bar{1}\bar{1})$ are studied to understand the role of loading orientation on the interaction between dislocation and the LRO Ni$_2$Cr precipitates. For the $[110](\bar{1}1\bar{1})$ slip system, a 350 MPa pure shear stress is applied in the full Burgers' vector direction. Moreover, for the $[101](1\bar{1}\bar{1})$ slip system, two different stress states are considered: (1) 750 MPa pure shear stress in the direction of the full dislocation(which results in a 650 MPa resolved shear stress on both dislocation partials) and (2) 650 MPa pure shear stress in the direction of the leading partial to explore the role of Schmid factor of the Shockley's partials the outcome of the interaction.

To explore possible twin formation process, the second part of MD simulations focuses on the interactions between multiple coplanar dislocations with a Pt$_2$Mo-structured precipitate for type 2 interactions. Specifically, the interaction between three consecutive coplanar $[101](1\bar{1}\bar{1})$ dislocations with the Pt$_2$Mo-structured precipitate under an applied shear stress of 350 MPa in the Burgers vector direction is investigated. To rationalize the observed mechanism, generalized SF energy (GSFE) curves of the Pt$_2$Mo-structured precipitate are investigated by shifting the top six layers along the $\langle 12\bar{1} \rangle$ direction by the Burgers vector of the Shockley partial $\frac{a}{6}\langle 12\bar{1} \rangle$.

6.1.2.2.4. Experimental Methods and Analysis Technique

As type 2 interaction is dominant compared to type 1 interaction (since 10 out of 12 slip systems are type 2 interaction), micropillar compression testing is performed specifically to activate different type 2 interactions. To further support the MD results on the type 2 interaction, two sets of single-crystal micropillars were fabricated and tested in two different loading orientations in order study the role of resolved shear stresses on the dislocation partials (directly related to the loading orientations) on the deformation mechanisms.

A FEI Quanta 3D dual-beam scanning electron microscope (SEM)/focused ion beam (FIB) was utilized for the fabrication of the micropillars and the observation of the subsequent testing. The micropillars have a square cross-section (~2 µm x ~2 µm) and side:length aspect ratios of 1:2.5-3. The bulk material removal was accomplished with a FIB beam of 2 nA at 30 keV and the final polishing was with a 0.3 nA beam at 16 keV. A detailed procedure is reported in [95]. The *in situ* microcompression tests were performed in the SEM using a Hysitron PI-88 Picoindenter. The tests were conducted at a strain rate of 2×10^{-3}/s.

A script was written in Python to visualize the micropillars and the activated slip such as to perform slip trance analysis. The procedures are detailed as followed. A representative pillar volume is created with the sample dimensions and crystal orientation obtained from SEM images and EBSD, respectively. The locations of the activated slip are measured in the post-deformation SEM images, as shown in Figure 6.13A for instance. To visualize dislocation slip, at the locations of the slip events, the top half of the representative pillar volume is shifted with respect to the bottom half along the slip plane and the burger direction of each of the 12 slip systems in FCC, like in Figure 6.13B. The slip system that provides the best match as compared to the post-deformation SEM images is determined to be the active slip system. For example, Figure 6.13A presents the post-deformation SEM image of a representative aged micropillar, showing

dislocation slip. In the representative pillar volume in Figure 6.13B, the slip system $(1\bar{1}1)[\bar{1}01]$ provides the best match to the activated slip in Figure 6.13A; therefore, slip system $(1\bar{1}1)[\bar{1}01]$ is determined to be the active slip system. In case of deformation twinning, for a given loading direction, the leading partials and trailing partials can be determined for the different perfect Burger vectors using the Thompson Tetrahedron [78]. Similarly, the procedure can be applied to identify the active deformation twinning systems.
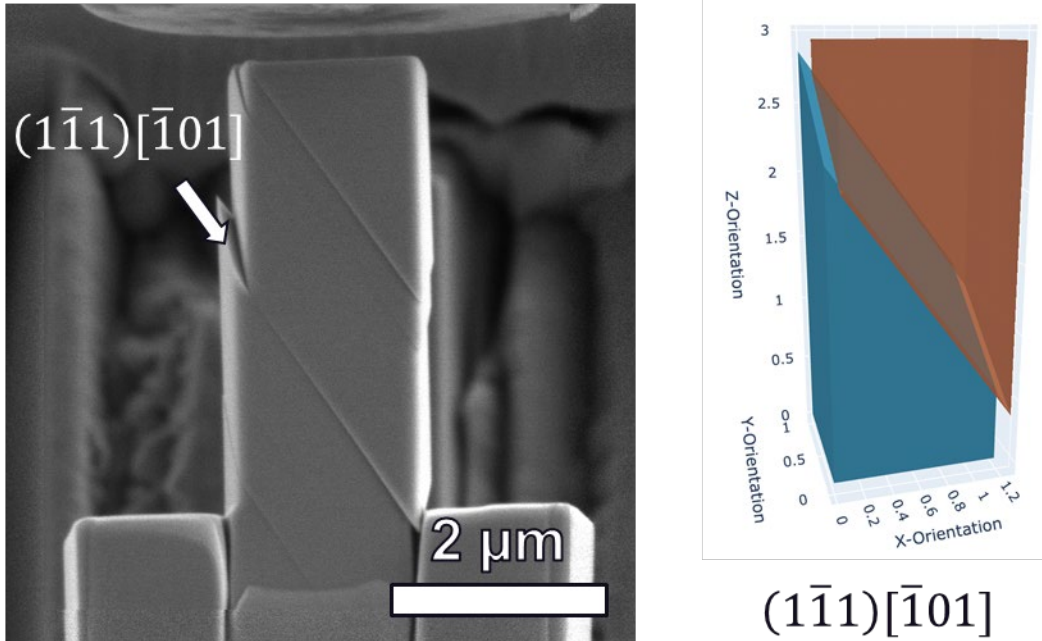
$(1\bar{1}1)[\bar{1}01]$

Figure 6-13. (A) The SEM image of a deformed micropillar with Euler angles (141.6^{o}, 35.5^{o}, -142.9^{o}). (B) The representative pillar volume of the tested micropillar shows that the activated slip system is determined to be ($1\bar{1}1)[\bar{1}01]$

The post-deformation microstructure was characterized by TEM. TEM lamellae of several deformed micropillars were lifted out and prepared with the FIB. The microstructures presenting within the lamella were characterized using selected area electron diffraction (SAED), bright-field (BF), and dark-field (DF) TEM. An FEI Tecnai F30 and an image-corrected FEI Titan 80-300, both operated at accelerating voltage of 300 kV, were employed to record the deformed microstructures.

6.1.2.3. Results and Analysis

6.1.2.3.1. Isolated interaction between an edge dislocation with the Pt$_2$Mo-structured precipitate via MD simulations

For FCC systems, it is energetically favored for the perfect dislocation to dissociate into two Shockley partials connected by an intrinsic stacking fault [78,181]. While the individual motion of the partials maintains the order, for 10 out of the 12 slip systems shown in Figure 6.11, the combined motions of these partials through the Pt$_2$Mo-structured precipitates (which is the Burgers vector) can disrupt the order of the precipitates and create anti-phase boundaries

(APBs). This process results in an extra energy barrier that the trailing partial needs to overcome to glide through the precipitate.

Four different configurations for the interaction between dislocation and the LRO Ni$_2$Cr precipitate are shown in Figure 6.14. Specifically, Figure 6.14A shows the interaction between an $[110](\bar{1}1\bar{1})$ (Type 1 interaction as shown in Figure 1) edge dislocation with the precipitate under 350 MPa pure shear stress in the $[110]$ direction. Figures 6.14B and 6.14C show the interaction between an $[101](1\bar{1}\bar{1})$ (Type 2 interaction as shown in Figure 1) edge dislocation with the precipitate in the $[101]$ direction under 350 and 750 MPa pure shear stress, respectively. In the last configuration, Figure 6.14D shows the type 2 interaction between an $[101](1\bar{1}\bar{1})$ edge dislocation with the precipitate under a 650 MPa shear stress in the leading partial to explore the effects of applied stress on the Shockley's partials to the outcome of the reaction. For slip systems with the [110] Burgers' vector (Type 1) shown in Figure 6.14A, the dislocation easily glides through the precipitate since it does not cause the anti-phase boundary inside the precipitate. In fact, for other slip systems under the same 350 MPa applied shear stress, only the leading partial glides through the precipitate (as shown in Figure 6.14B for the [101] Burgers' vector). In these cases (i.e. Type 2), the trailing partial is pinned by the precipitate due to the extra energy barrier caused by the APB which would form when the trailing partial sweep through the precipitate. This indicates that the resolved shear stress of $350\cos 30^o \approx 303$ MPa on the trailing partial is insufficient to push the trailing partial through the precipitate and create the APB in the process. When the shear stress is increased up to 750 MPa which results in a 650 MPa resolved shear stress on both partials, the trailing partial can glide through and disorder the Pt$_2$Mo-structured precipitates, as shown in Figure 6.14C for the $[101](1\bar{1}\bar{1})$ edge dislocation. Importantly, the resolved shear stress on the trailing partial is essential to the outcome of the interaction. This is shown in Figure 6.14D for the same slip system but under different stress state of 650 MPa shear stress in the leading partial, which is identical to the resolved shear stress on the leading partial of the configuration shown in Figure 6.14C. However, the resolved shear stress on the trailing partial is only $650\cos 60^o \approx 325$ MPa, which is much lower than the resolved shear stress acting on the trailing partial of the configuration shown in Figure 6.14C. As a result, only the leading partial can glide through the precipitates while the trailing partial is pinned, which elongates the ISF between these partials. Consistent with the geometric-based theory, configurations 1 and 2 (Figures 6.14A and 6.14B) show that the type 2 interaction elongate the stacking fault width as the APB formation energy prevents the trailing partial from easily gliding through the precipitate as compared to type 1 interaction. In addition, the comparison between configurations 3 and 4 (Figures 6.14C and 6.14D) show that the resolved shear stresses acting on the dislocation partials significantly influence the stacking fault width. This finding suggests that type 2 interaction does not necessarily lead to deformation twinning as the role of the resolved shear stresses on the partial dislocations need to be considered. To provide experimental evidence to this hypothesis, micropillar compressions of single crystal Ni$_2$Cr are tested in two specific loading orientations to activate type 2 interaction with different resolved shear stresses acting on the dislocaiton partials.
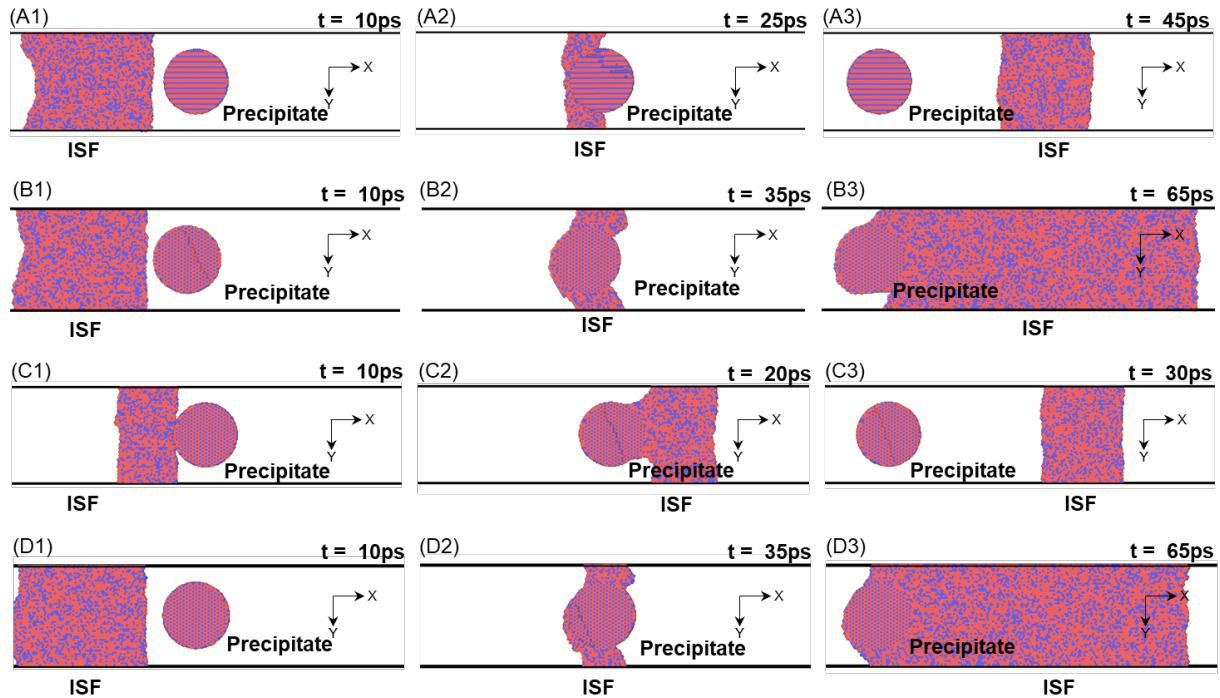
Figure 6-14. Top view of dislocation – precipitate interactions. (A1), (A2), and (A3) are snapshots of $[110](\bar{1}1\bar{1})$ edge dislocation interaction with precipitate under 350 MPa pure shear stress in the Burgers' vector direction at 10, 25, and 45 ps, respectively. (B1), (B2), and (B3) are snapshots of $[101](1\bar{1}\bar{1})$ edge dislocation interaction with precipitate under 350 MPa pure shear stress in the Burgers' vector direction at 10, 35, and 65 ps, respectively. (C1), (C2), and (C3) are snapshots of $[101](1\bar{1}\bar{1})$ edge dislocation interaction with precipitate under 750 MPa pure shear stress in the Burgers' vector direction at 10, 20, and 30 ps, respectively. (D1), (D2), and (D3) are snapshots of $[101](1\bar{1}\bar{1})$ edge dislocation interaction with precipitate under 650 MPa pure shear stress in the leading Shockley's partial at 10, 35, and 65 ps, respectively.

6.1.2.3.2. Micropillar Compression and TEM analysis

Two sets of micropillars were tested. The crystal orientations of the micropillars are selected such that the type 2 slip systems would have the highest Schmid factors for the perfect dislocations (SF$_P$). Set 1 has the Euler angles of (141.6°, 35.5°, -142.9°) and set 2 has the Euler angles of (-78.6°, 70.9°, -69.9°). Three micropillars of each set were tested to failure. Additional tests were performed and stopped slightly pass yielding for TEM characterization of the deformed pillars. The representative resolved shear stress versus strain plots of the two sets are shown in Figure 6.15A. The set 1 micropillars deformed only via dislocation slip (Figure 6.15B) while the set 2 micropillars deformed via deformation twinning followed dislocation slip (Figure 6.15C). In both sets, the slip events correspond to a strong strain burst while the twin events show stabilized plastic flow, as indicated in Figure 6.15A.

90
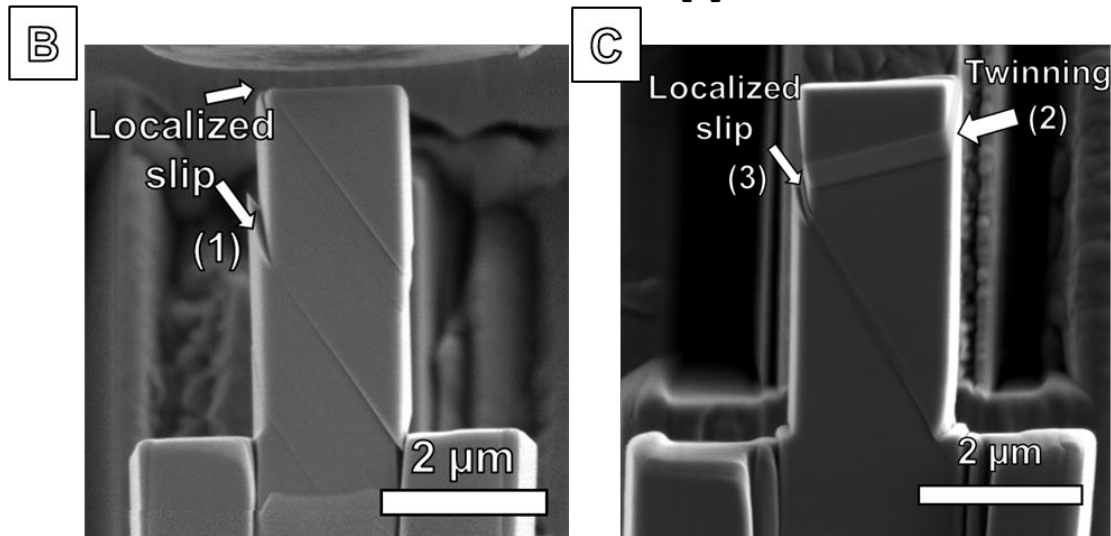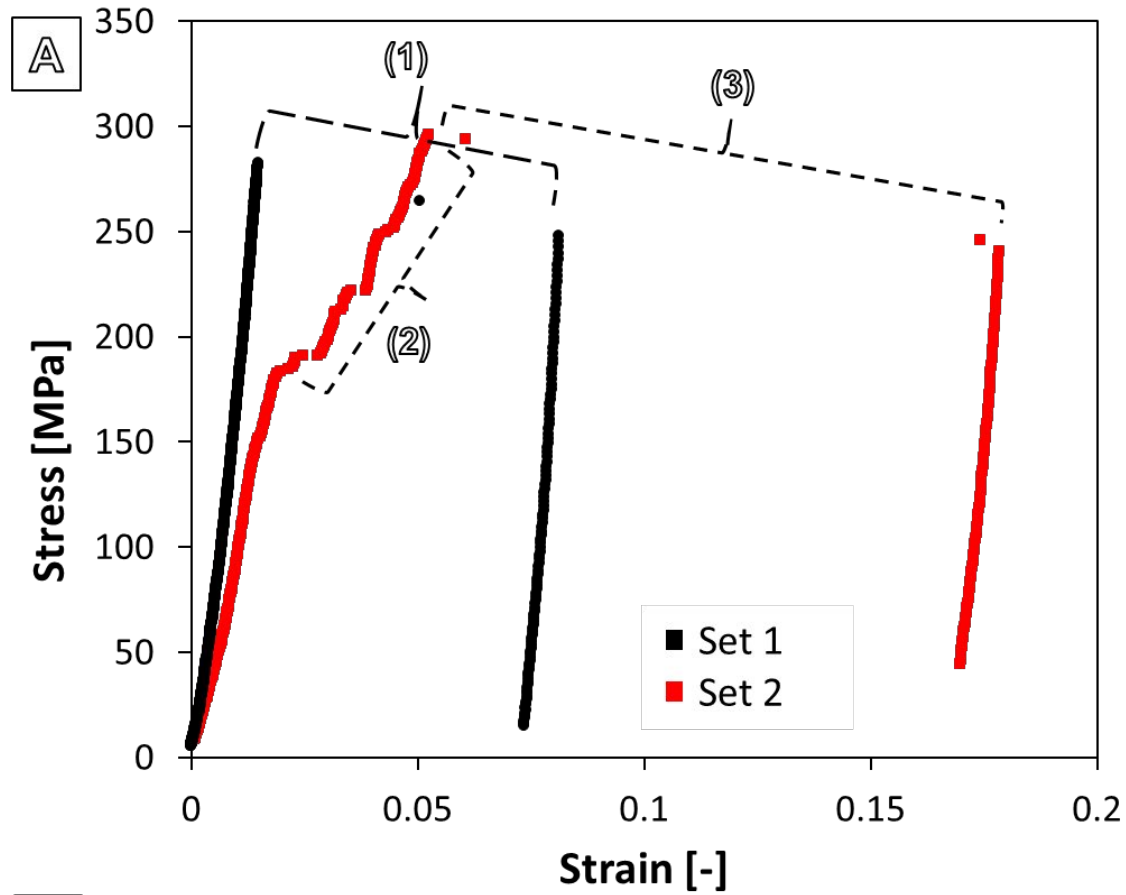
Figure 6-15. (A) The representative resolved shear stress-strain curves of sets 1 and 2. The SEM images of (A) a representative deformed micropillar set 1, (B) a representative deformed micropillar set 2. The different deformation events are indicated with arrow signs and correlated with the stress-strain curves

To confirm the presence of the deformation twin in set 2, HR-TEM was performed on the deformed twinned micropillars. Figure 6.16 shows the HR-TEM image of the twinned micropillars with the sample oriented along the $[01\bar{1}]$ axis, clearly shows the twin-matrix interface along $(1\bar{1}\bar{1})$ plane. The inset selected area electron diffraction (SAED) pattern shows the diffraction spots from both the matrix and the twin domains, confirming the presence of the deformation twin. {211} steps were observed along the twin-matrix interface; these steps are commonly observed in FCC metals [182].
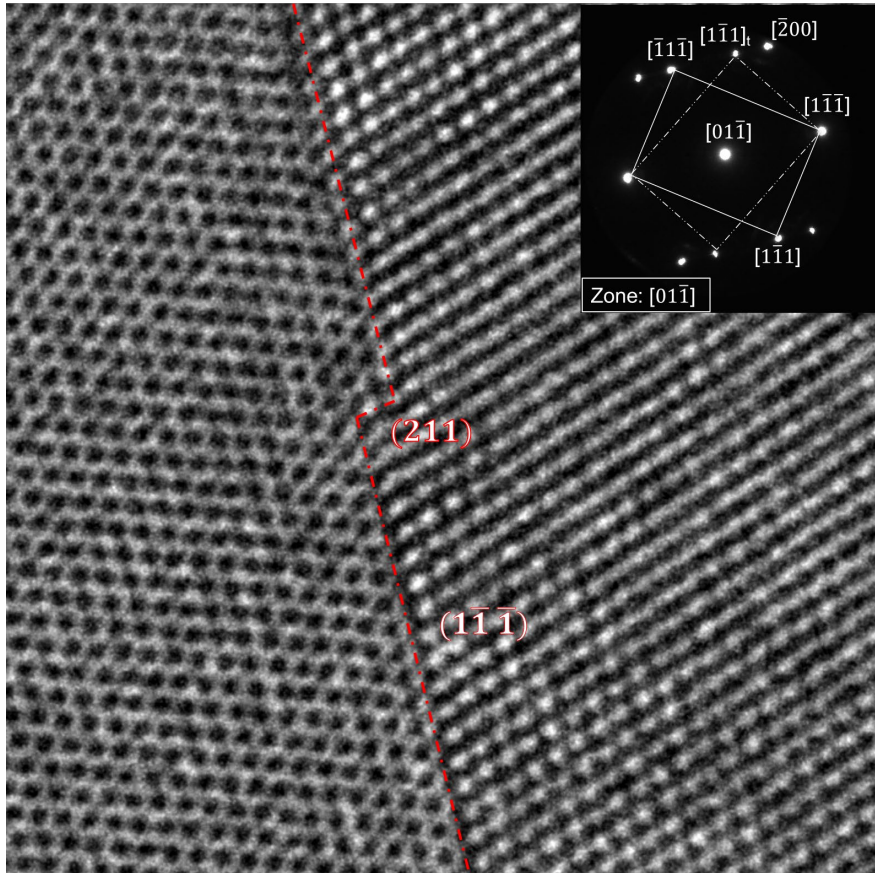
Figure 6-16. HR-TEM micrograph of the twin/matrix interface. The right image shows the corresponding selected area electron diffraction (SAED) pattern oriented along the $[01\bar{1}$-1] zone axis.

To determine the active slip/twin systems, slip trace analysis was performed in both sets. In set 1, the activated slip system is determined to be $(1\bar{1}1)[\bar{1}01]$ as shown in Figure 6.13. Table 1 shows the Schmid factor of the perfect dislocation (SF_P), leading partial (SF_{LP}), and trailing partial (SF_{TP}) for all slip systems for set 1. The activated slip system $(1\bar{1}1)[\bar{1}01]$ has the highest SF_P, SF_{LP}, and SF_{TP}. Although the activated slip system is Type 2, deformation twinning did not take place. Because the SF_{LP} (0.311) is lower than the SF_{TP} (0.432), the resolved shear stress along the trailing partial is ~1.4 (0.432/0.311) times higher than that of the leading partial. The higher resolved shear stress on the trailing partial means a higher driving force for the trailing partial to overcome the ordered precipitate and close the intrinsic stacking fault.

*Table 6.2. The Schmid factors for the leading partials (**SF$_{LP}$**), trailing partials (**SF$_{TP}$**), and the perfect Burger vectors (**SF$_{PD}$**) for micropillar set 1's slip systems. The loading direction is [-0.350, -0.463, 0.814] and the pillars' Euler angles are (141.6º, 35.5º, -142.9º). The activated slip system is bolded.*

Slip systems	SF$_{PD}$	SF$_{LP}$	SF$_{TP}$
$(111)[\bar{1}10]$	0.000	0.000	0.000
$(111)[\bar{1}01]$	0.000	0.001	0.000
$(111)[0\bar{1}1]$	0.000	0.000	0.001
$(11\bar{1})[\bar{1}10]$	0.075	0.221	0.091
$(11\bar{1})[101]$	0.308	0.221	0.313
$(11\bar{1})[011]$	0.233	0.091	0.313
$(1\bar{1}1)[110]$	0.308	0.101	0.432
$(1\bar{1}1)[\bar{1}01]$	**0.441**	**0.331**	**0.432**
$(1\bar{1}1)[011]$	0.133	0.331	0.101
$(\bar{1}11)[110]$	0.233	0.058	0.346
$(\bar{1}11)[101]$	0.133	0.288	0.058
$(\bar{1}11)[0\bar{1}1]$	0.366	0.288	0.346
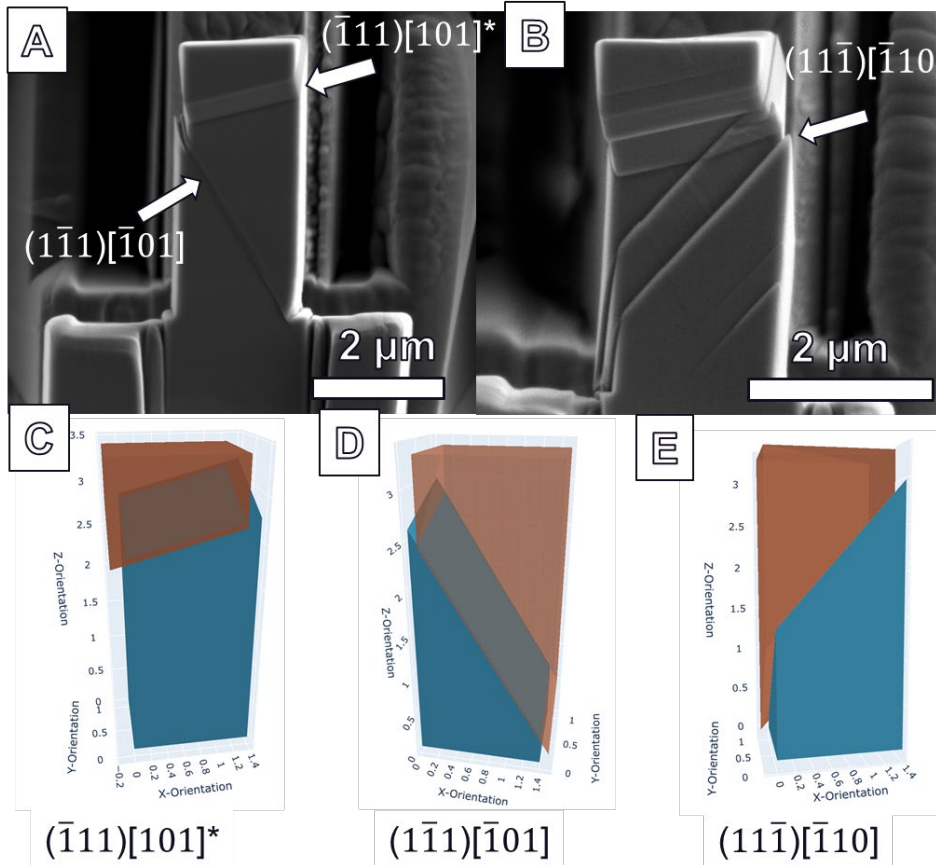
$(\bar{1}11)[101]^*$

$(1\bar{1}1)[\bar{1}01]$

Figure 6-17. (A)(B) show the SEM images of two representative deformed micropillars with Euler angles (-78.6°, 70.9°, -69.9°). Using the visualization script, the simulated slip systems (C) ($\bar{1}$11)[101], (D) (1$\bar{1}$1)[$\bar{1}$01], and (E) (11$\bar{1}$)[$\bar{1}$10] were shown by displacing the corresponding slip planes of the simulated micropillar along the Burger vector direction. *Important to note, the leading partial of the slip system ($\bar{1}$11)[101] (C) is responsible for the deformation twinning observed in (A,B).

Figure 6.17A and 6.17B show the two deformation behaviors observed in set 2 where deformation twinning on slip system ($\bar{1}$11)[211] followed by slip either on (1$\bar{1}$1)[$\bar{1}$01] slip system (Figure 5A) or on (11$\bar{1}$)[$\bar{1}$11] slip system (Figure 6.17B). Figure 6.17C,6.17D, and 6.17E show the slip system visualization for all the observed active slip systems.

Similarly, in Table 2, SF_{PD}, SF_{LP}, and SF_{TP} values are reported for all slip systems. Although slip system ($\bar{1}$11)[101] does not have the highest SF_P (0.352) compared to the secondary activated slip systems (11$\bar{1}$)[$\bar{1}$10] (0.440) and (1$\bar{1}$1)[$\bar{1}$01] (0.439), the corresponding leading partial of slip system ($\bar{1}$11)[101] has the highest SF_{LP} (0.408) out of all slip systems and slightly higher than the secondly activated slips' SF_{LP}. Secondly, the trailing partial of the slip system ($\bar{1}$11)[101] has a very low SF_{TP} compared to the secondary activated slip systems' SF_{TP} (0.372 and 0.371). Another point is that the Schmid factors of the leading and trailing partials are very similar in the slip case in contrast to the twin case, where the Schmid factor of the leading partial is significantly higher than that of the trailing partial. The deformation response from both sets indicates that type 2 interaction can activate both deformation twinning and slip. Deformation twinning takes place when the driving force on the leading partial is higher than that of the trailing partial; and, slip takes place when the driving force on the leading partial is similar or lower than that of the trailing partial. The microcompression results are consistent with the MD results in the previous section. However, to further establish the connection between the MD results and the experimental observations, the twin formation process from an intrinsic stacking fault (ISF) caused by type 2 interaction is explored from an energy-based perspective in the next section.

*Table 6.3. The Schmid factors for the leading partials (**SF_{LP}**), trailing partials (**SF_{TP}**), and the perfect Burger vectors (**SF_{PD}**) for micropillar set 2's slip systems. The loading direction is [-0.888, 0.325, 0.327] and the pillars' Euler angles are (-78.6°, 70.9°, -69.9°). The slip systems activated are bolded.*

Slip Systems	SF_{PD}	SF_{LP}	SF_{TP}
(111)[$\bar{1}$10]	0.117	0.135	0.067
(111)[$\bar{1}$01]	0.117	0.068	0.135
(111)[0$\bar{1}$1]	0.000	0.067	0.068
(11$\bar{1}$)[$\bar{1}$10]	**0.440**	**0.391**	**0.372**
(11$\bar{1}$)[101]	0.204	0.019	0.372
(11$\bar{1}$)[011]	0.237	0.391	0.019
(1$\bar{1}$1)[110]	0.204	0.019	0.371
(1$\bar{1}$1)[$\bar{1}$01]	**0.439**	**0.390**	**0.371**
(1$\bar{1}$1)[011]	0.236	0.390	0.019

$(\bar{1}11)[110]$	0.354	0.408	0.205
$\mathbf{(\bar{1}11)[101]}$	**0.352**	**0.408**	**0.203**
$(\bar{1}11)[0\bar{1}1]$	0.001	0.205	0.203

6.1.2.3.2. Twin formation process from an ISF induced by type 2 interaction via MD simulations

So far, our MD results only show how type 2 interaction can lead to the formation of ISF. To rationalize with the experimental observation and confirm that the Pt$_2$Mo-structured precipitates indeed lead to twinning, MD simulations were performed to demonstrate the twin formation process from a 1-layer twin (ISF) induced by type 2 interaction. While it is commonly agreed that twinning in FCC systems starts with the formation of ISF (sometimes called 1-layer twin), there are many proposed mechanisms for how the ISF evolves into a multiple-layer twin [183,184]. S. Mahajan has extensively outlined the different theories for twinning thickening process in FCC metals [183]. However, it has remained a challenge to provide direct experimental observations and detailed molecular dynamics work to confirm the proposed theories. Here, we applied MD simulations to propose a potential ISF-to-twin formation mechanism to explain the role of Pt$_2$Mo-structured precipitates on deformation twinning.

One possible scenario is that the glide and interactions of multiple coplanar dislocations with the precipitate plays a role in triggering twinning. To model this scenario and assess this hypothesis, at the end of the configuration shown in Figure 6.14B, two more dislocations are inserted and driven toward the precipitates for interactions. Indeed, Figure 6.18 shows the interaction between multiple coplanar $[101](1\bar{1}\bar{1})$ dislocations with the LRO precipitate under an applied shear stress of 350 MPa in the Burgers vector direction. This reaction is likely since multiple dislocations can be emitted from the same dislocation source from the free surface. The interaction of the 1st dislocation results in the passing of the leading partial and pinning of the trailing partials by the ordered precipitate. Figure. 6.18A, 6.18B, and 6.18C show the interaction of the 2nd dislocation with the ordered precipitate and Figure 8D and 8E show the interaction of the 3rd dislocation with the ordered precipitate. Figure 8F shows the intrinsic stacking fault formed by the leading partial of the 1st dislocation. Interestingly, when the 2nd dislocation arrives near the precipitate, there is a repulsive force between the leading partial of the 2nd dislocation and the trailing partial of the 1st dislocation. This provide an extra driving force for the trailing partial of the 1st dislocation to move out of the precipitate and generate the APB within the precipitate in the process. The interaction of the 2nd dislocations' leading partial with the APB results in a 2-layer SF (i.e. an extrinsic stacking fault) inside the precipitate as seen in Figures. 6.188G and 6.18H. This newly formed 2-layer SF then acts as a barrier when the 3rd dislocation interacts with the precipitate. While there is also a repulsive force between the leading partial of the 3rd dislocation and the trailing partial of the 2nd dislocation, the pinning effects of the 2-layer SF inside the precipitate is significant and prevent the trailing partial of the 2nd dislocation to sweep through the precipitate. As a result, the leading partial of the 3rd dislocation cross-glide and forms the 2-layer SF in the matrix shown in Figures 6.18I and 6.18J. This process is repeated for the subsequent dislocations and thickening the twin in the process.
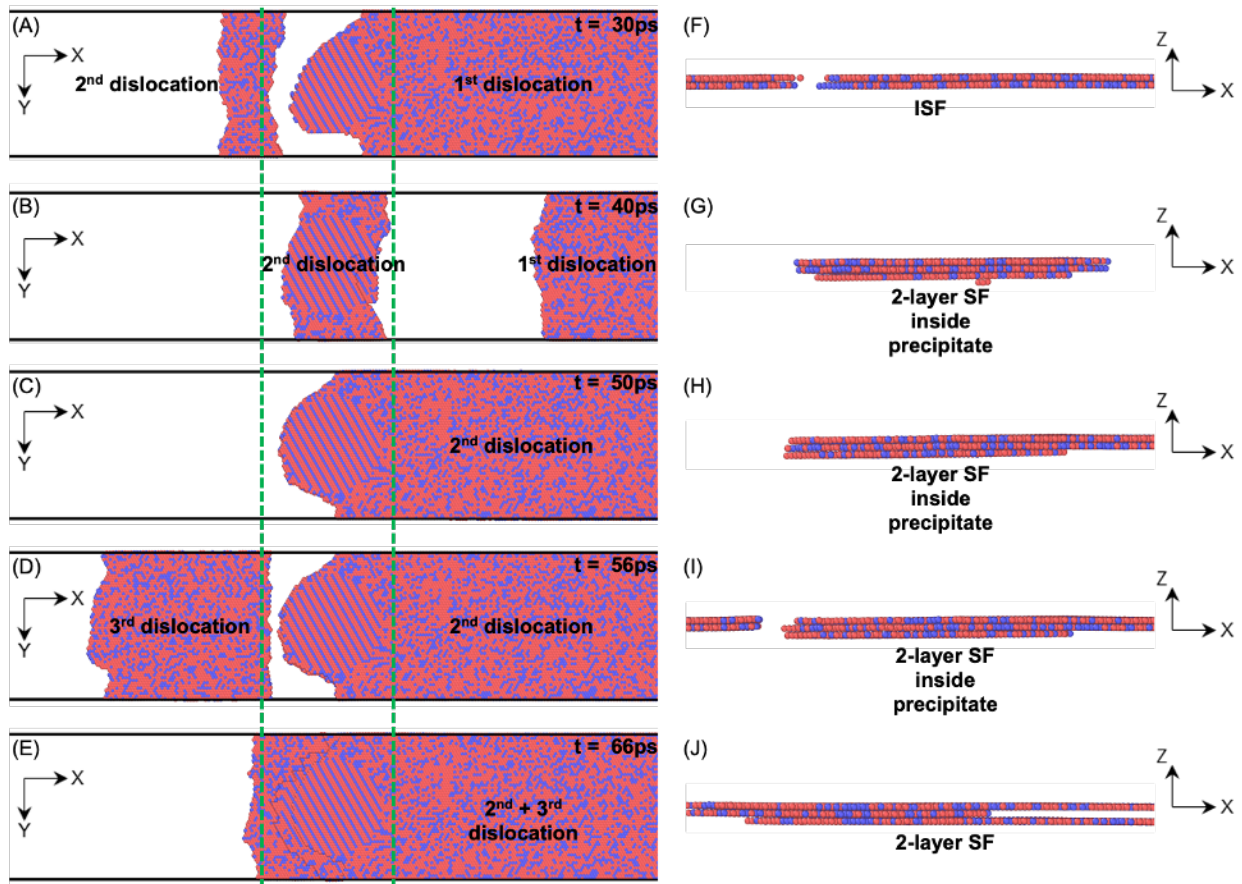
Figure 6-18. Top view of 3 co-planar edge dislocation – precipitate interactions at (A) 30 ps, (B) 40 ps, (C) 50 ps, (D) 56 ps, and (E) 66 ps. (F), (G), (H), (I), and (J) are the side view of the regions between two green dashed lines in (A), (B), (C), (D), and (E), respectively. Red atoms are Ni, while blue atoms are Cr. Perfect atoms are removed in all figures.

These MD results also indicate that the structures of the precipitate when the 1st and 2nd dislocations arrive are significantly different due to the formation of the APB after the trailing dislocation of the 1st dislocation sweeps through. However, these simulations do not rationalize why the interaction of the APB with the leading partial of the 2nd dislocation results in the 2-layer SF shown in Figures 6.18B and 6.18F. To further understand this process, generalized SF energy (GSFE) curves of the initial precipitate ordered structure and the one with APB are investigated. Figure 6.19 shows that the intrinsic SF energy of the precipitate is 62.8 mJ/m². However, once the 1st dislocation passes through and creates an APB, the intrinsic SF energy of two consecutive $(1\bar{1}\bar{1})$ atomic planes (the APB and the layer right below) is -227 mJ/m² as shown in Figure 6.19C. These negative SF energies indicate that the FCC structure will destabilize to become the HCP structure. Therefore, it is energetically favored for the atoms to be in HCP stacking inside the precipitate with the antiphase boundary. As a result, 2-layer SF is formed as shown in Figures 6.18G, and 6.18H. Similar behaviors of negative SF energies and nano-twin formation have been observed in FCC high entropy alloys[185]. Therefore, from an energy-based approach, MD results

have shown that type 2 interaction can lead to deformation twinning, which is consistent with the experimental observations.

Figure 6-19. Atomic configurations of the original precipitate (A) initially and (B) with intrinsic SF. (C) Generalized SF energy (GSFE) curves of the perfect crystal structure and the antiphase boundary. Atomic configurations of the precipitate (D) with APB, (E) with APB and intrinsic SF, and (F) with APB and intrinsic SF of the layer below the APB. All configurations are viewed along the Burgers vector direction of the FCC matrix. Red atoms are Ni, while blue atoms are Cr. APB is marked by the black dashed lines.

6.1.2.3.3. Summary of the deformation twinning process

The schematic in Figure 6.20 summarizes the proposed deformation twinning process in Type 2 configuration. When the first dislocation interacts with the Pt_2Mo-structured precipitates, the leading partial passes through the precipitates while the trailing partial is pinned. The stacking fault elongates as the leading partial continues to propagate (Figure 6.20A.) The addition of the APB term allows for sufficient interaction time for the second coplanar dislocation to interact with the trailing partial of the first dislocation. The leading partial of the second dislocation adds an additional forward force to unpin the first dislocation's trailing partial, leaving an APB behind (Figure 6.20B.) The leading partial interacts with the APB and forms an extrinsic fault (Figure 6.20C.). MD shows that such process is energetically favorable. The second dislocation's leading

97

partial continues to propagate. As the third dislocation approaches the 2-layer SF, the dislocation cross-glide and the leading partial propagates and forms the 2-layer SF in the matrix (Figure 6.13D.) We propose that the twin would thicken successively from the 2-layer SF by the repeating the process.
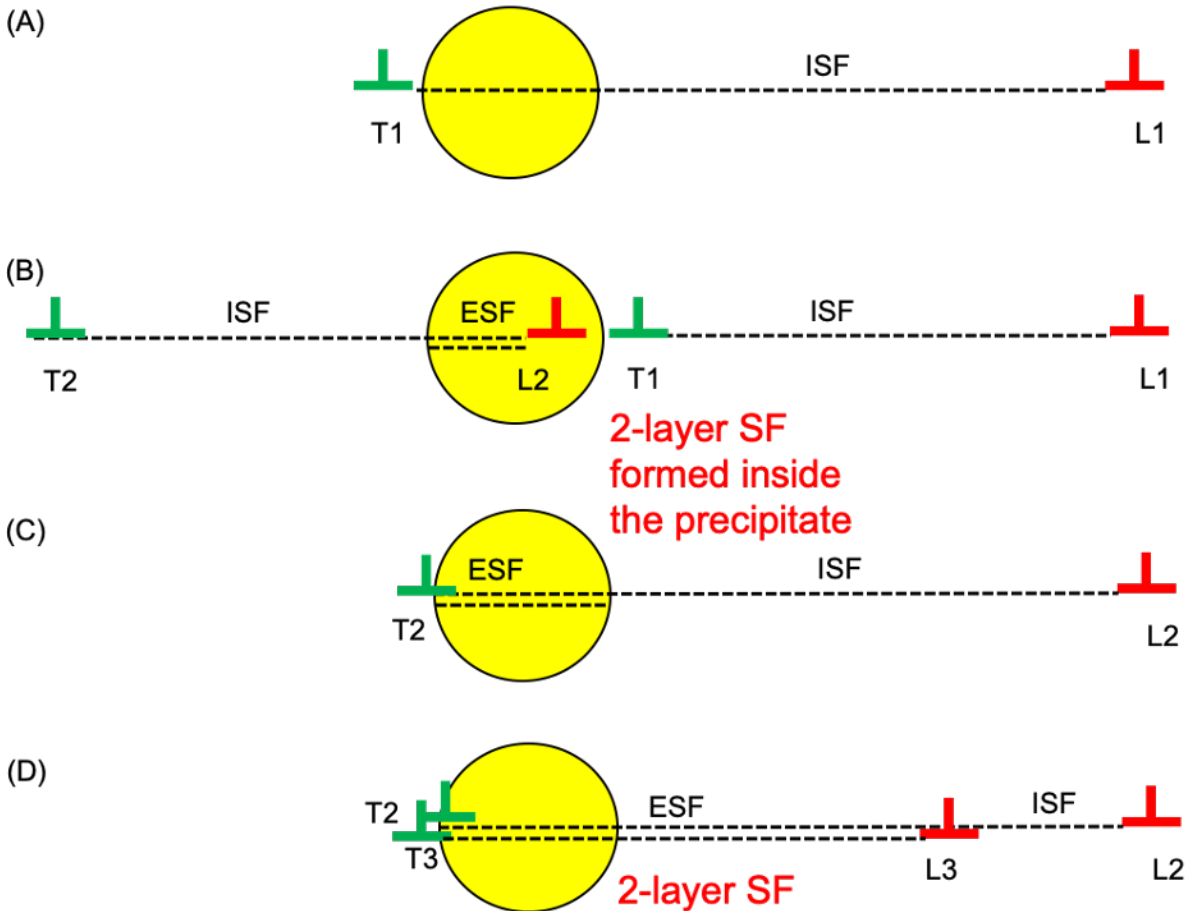
Figure 6-20. Schematic summarizing the MD observation of the formation of 2-layer fault from single-layer intrinsic fault.

6.1.2.4. Discussion

6.1.2.4.1. Influence of the applied stress on partial dislocations and APB formation on stacking fault formation

As shown in the previous sections, the deformation mode depends on the interaction between the partials and the ordered precipitates. To qualitatively understand the different factors influencing the deformation mode, we look at the forces acting on the leading and trailing partials when they meet the precipitates. Figure 6.21 shows the partial dislocations and precipitate setup considered in our formulation. The different angles are defined in Figure 6.21. For simplicity, we consider the edge dislocations to be consistent with the MD simulation.
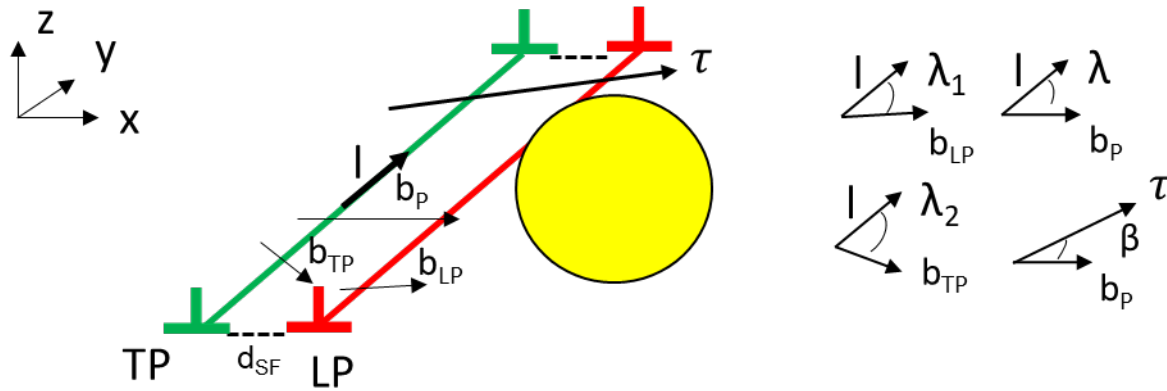
Figure 6-21. A schematic of the partial dislocations and precipitate arrangement; LP: leading partial, TP: trailing partial, d_{SF}: stacking fault width, b_p: perfect Burger vector, b_{LP}: leading partial's Burger vector, b_{TP}: trailing partial's Burger vector, l: line direction, τ: applied shear stress, λ_1 : the angle between the line direction and the leading partial's Burger vector, λ_2 : the angle between the line direction and the trailing partial's Burger vector, λ : the angle between the line direction and the perfect Burger vector, β: the angle between the applied stress and the perfect Burger vector

Similar to the formulations proposed in [186], the equilibrium force equations of the leading and trailing partials are then written, for type 1 configuration, as:

$$F_{LP} = b_p \tau cos\,(30^o - \beta) - \gamma_{SF} + \frac{Gb_P^2}{2\pi d_{SF}}\left(cos(\lambda_{LP})\,cos(\lambda_{TP}) + \frac{1}{1-v}sin(\lambda_{LP})\,sin(\lambda_{TP})\right) - \frac{Gb_P^2}{R} - f_o = 0 \;\; Eq.\;\; 6.9$$

$$F_{TP,} = b_p \tau cos\,(\beta + 30^o) + \gamma_{SF} - \frac{Gb_P^2}{2\pi d_{SF}}\left(cos(\lambda_{LP})\,cos(\lambda_{TP}) + \frac{1}{1-v}sin(\lambda_{LP})\,sin(\lambda_{TP})\right) - \frac{Gb_P^2}{R} - f_o = 0 \;\; Eq.\;\; 6.10$$

Where F_{LP} : total force acting on the leading partial; F_{TP} : total force acting on the trailing partial; γ_{SF} : stacking fault energy created inside the precipitate; γ_{APB} : antiphase boundary energy created inside the precipitate; d: separation distance between the partials; G : shear modulus, f_o : other backward forces, not including the APB energy term.

In Eq. 6.9 and Eq. 6.10, the forward forces are positive, and the backward forces are negative. The first term accounts for the different resolved shear stresses acting on the leading and trailing partials. The second term describes the force imposed by the stacking fault formation that pulls the leading partial backward and pushes the trailing partial forward. The third term accounts for the interaction between the leading and the trailing partials. The fourth term is the line tension energy term imposed by the precipitate pinning. The last term describes the other backward forces that do not include the APB energy term and the line tension energy term. By subtracting

Eq. 6.9 from Eq. 6.10, we obtain the equation for the stacking fault width for Type 1 configuration, similar to the equation reported in [186].

$$d_{SF} = \frac{\left(cos(\lambda_{LP}) \, cos(\lambda_{TP}) + \frac{1}{1-\nu} sin(\lambda_{LP}) \, sin(\lambda_{TP})\right) Gb_P^2}{\pi[2\gamma_{SF} - b_p\tau(cos(30^o - \beta) - cos(\beta + 30^o))]} \quad Eq. \ 6.11$$

For edge dislocations, EQ3 is simplified into:

$$d_{SF} = \frac{\left(-\frac{1}{4} + \frac{3}{4(1-\nu)}\right) Gb_P^2}{\pi[2\gamma_{SF} - b_p\tau(cos(30^o - \beta) - cos(\beta + 30^o))]} \quad Eq. \ 6.12$$

The parameters in Eq. 6.11 are provided by the MD results and the MD potential. The MD calculates the γ_{SF} of the stacking fault created inside the precipitate to be 62.8 mJ/m^2. The shear modulus, G, and the Poisson ratio, ν, are calculated from the elastic constants provided by the MD potential, to be 77.142 GPa and 0.338, respectively. The magnitude of the Burgers vector partial is calculated to be 0.145 nm.

Eq. 6.11 and Eq. 6.12 describe a theoretical equilibrium stacking fault width created inside the precipitate for Type 1. In Type 1 configuration, EQ3 shows that the stacking fault width depends primarily on the SF energy and the difference between the resolved shear stresses of the partials. The difference in the partials' stresses can be described by the angle β. For example, the ratio between the τ_{LP} and τ_{TP} are 1.0 and 2.0 for β of 0° and 30°, respectively. Using the provided values and EQ3, Figure 6.22 plots theoretical equilibrium stacking fault width created inside the precipitate as a function of the applied shear stress for different β angles. As shown in the figure, the β angles, equivalently the partials' resolved shear stress differences, significantly influences the stresses required to maintain a certain stacking fault width.
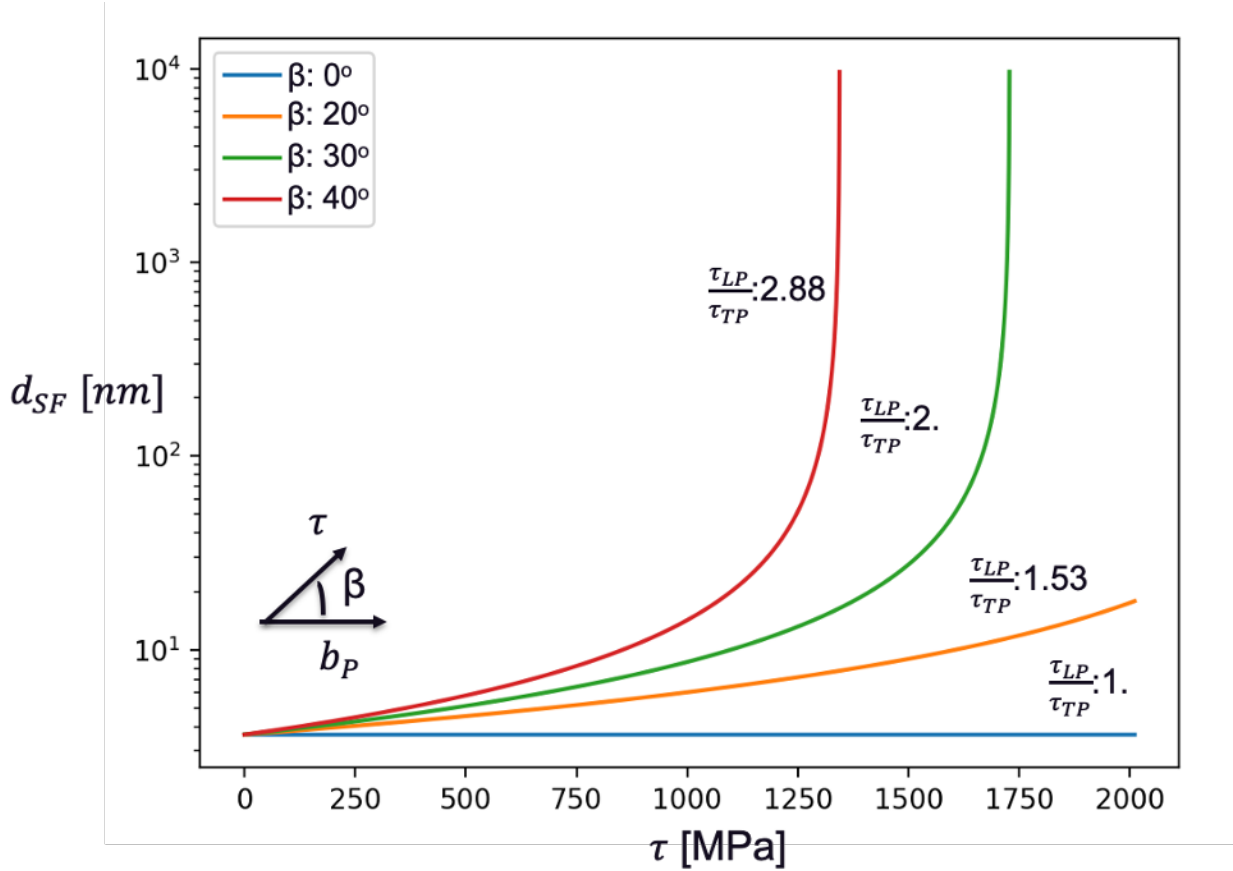
Figure 6-22. The theoretical equilibrium stacking fault width as a function of applied shear stress at different β angles. As shown in Figure 14, β describes the angle between the applied shear stress and the perfect Burger vector. Therefore, β influences the difference between the resolved shear stresses of the leading and trailing partials.

In Type 2 configuration, an additional resisting force results from the antiphase boundary formation is added in Eq. 6.10. Therefore, Eq. 6.10 is modified to be:

$$F_{TP,} = b_p \tau \cos(\beta + 30^o) + \gamma_{SF} - \frac{Gb_P^2}{2\pi d}\left(\cos(\lambda_{LP})\cos(\lambda_{TP}) + \frac{1}{1-v}\sin(\lambda_{LP})\sin(\lambda_{TP})\right) - \frac{Gb_P^2}{R} - \gamma_{APB} - f_o = 0 \; Eq. \; 6.13$$

For Type 2 configuration, by subtracting Eq. 6.9 from Eq. 6.13, the stacking fault width for an edge dislocation is then written as:

$$d_{SF} = \frac{\left(-\frac{1}{4} + \frac{3}{4(1-v)}\right)Gb_P^2}{\pi[2\gamma_{SF} - \gamma_{APB} - b_p\tau(\cos(30^o - \beta) - \cos(\beta + 30^o))]} \; Eq. \; 6.14$$

101

Eq. 6.14 shows that the γ_{APB} helps lower the applied stress required to elongate and maintain a certain stacking width. Our MD result calculates the γ_{APB} of the antiphase boundary created by the trailing partial to be 139.3 mJ/m^2. Since the $\gamma_{APB}/\gamma_{SF} > 2.0$, this means that it is always preferred for the stacking fault to form and elongate when the dislocation interacts with the precipitate. However, it assumes that the ordered precipitate is infinitely large. For the finite ordered precipitate size, we observed that the stress difference between the partials play a role in determining the deformation mode, as shown in experiment and modeling. In micropillar set 2, dislocation slip takes place when the Schmid factors of the partials are similar while deformation twinning takes place when the Schmid factor of the trailing partial is a lot lower than that of the leading partial, as shown in Table 6.3. A similar observation was made for the stacking fault formation in the MD results (Figure 6.20). Nevertheless, this exercise allowed us to conceptualize how the APB formation helps to lower the stress required for elongating the stacking fault.

6.1.2.4.2. Comparison between plastic stability between unaged and aged micropillars

To understand the influence of thermal aging on plastic stability, a set of unaged micropillars was tested in order to compare the plastic flow response with those of the aged micropillars. The plastic instability is indicated by the severity of the strain burst events in displacement-controlled micropillar tests. Since the PI88 picoindenter is inherently load controlled, the transducer uses the feedback loop to maintain a constant displacement. When sudden deformation takes place, the feedback loop is not fast enough to follow the displacement, resulting in a load drop and a strain jump. When the indenter catches up with the displaced micropillar, the load and displacement resume recording.

Figure 6.23 shows the representative SEM images of the deformed micropillars in unaged (Figure 6.23A) and aged (Figure 6.23B and 6.23C) conditions. In the unaged condition, multiple slip bands are formed closely together, which is characteristic of the diffused slip behavior found in metals with high ductility [99,187]. The corresponding strain bursts are small, as shown in Figure 6.23D. In contrast, dislocation slip in the aged micropillars is composed of fewer slip bands and spaced further apart; and the corresponding strain burst's magnitude is significantly greater compared to the unaged condition (Figure 6.23D.) Additionally, there is a lack of strain hardening and the beginning of the plastic domain is marked by a severe strain burst (Figure 6.23D.) The strain bursts associated with deformation twinning are very minimal and a clear work hardening response is observed (Figure 6.23D.) Therefore, Figure 6.23 suggests that deformation twinning helps stabilize the plastic flow while dislocation slip exacerbates the plastic instability in the aged alloys. This observation also confirms the hypothesis that deformation twinning is responsible for retaining the material's ductility after thermal aging.
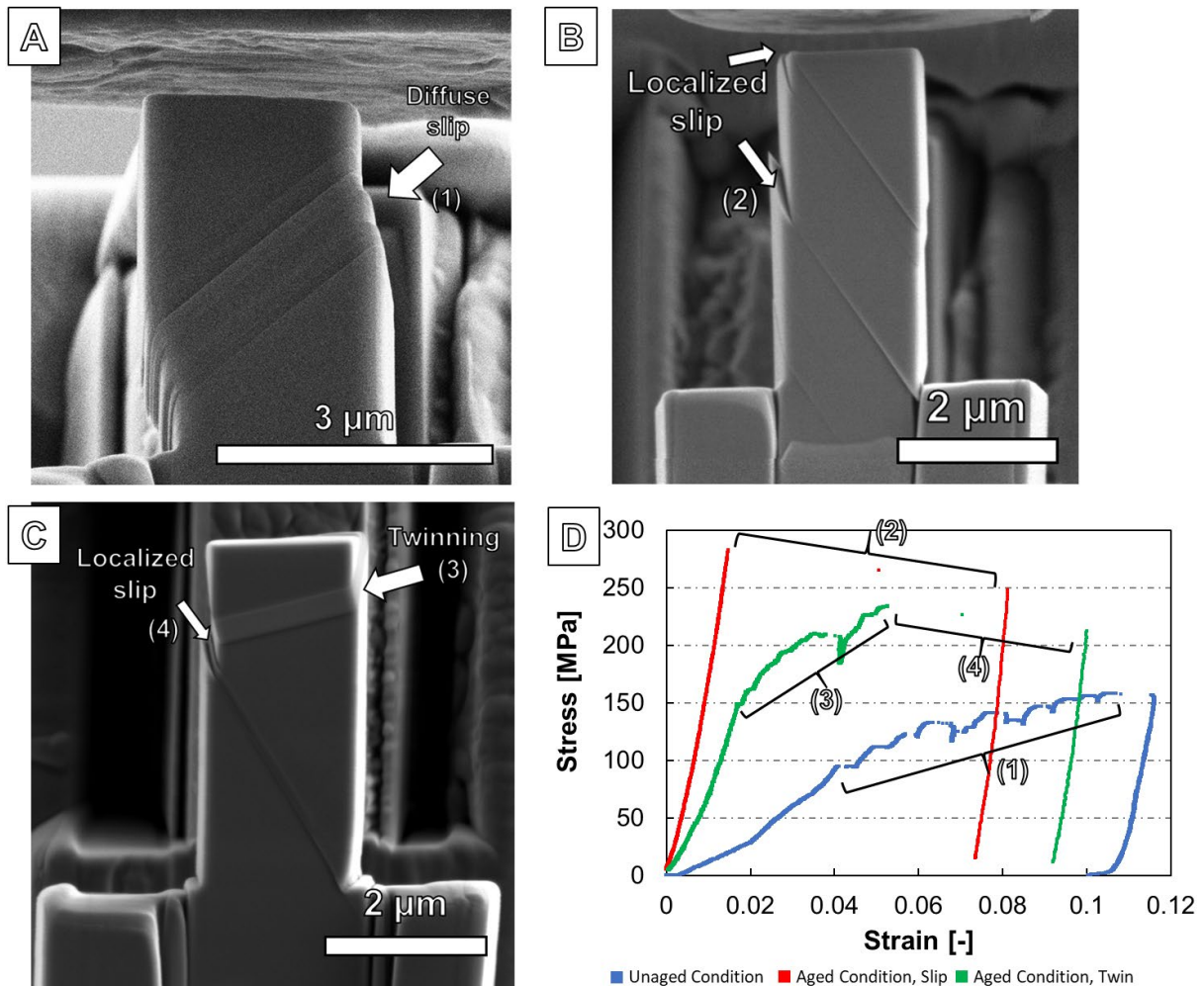
Figure 6-23. SEM images of (A) a representative deformed unaged micropillar, (B) a representative aged micropillar of set 1, (C) a representative aged micropillar of set 2. (D) The corresponding resolved shear stress-strain curves of the micropillars (A-C). The different deformation events are indicated with arrow signs and correlated with the strain-strain curves

6.1.2.5. Conclusion

In this study, we explored the different possible interactions between the dislocations and Pt$_2$Mo-structured precipitates (Ni$_2$Cr type) at room temperature. Since Pt$_2$Mo-structured precipitates are used in a wide class of Ni-Cr and Ni-Cr-Mo alloys used in power generation industries [67,172], the findings reported here serve the need to further understand the deformation behaviors of these alloys. The advances made in this work are summarized as followed:

1. Molecular dynamics simulations examined type 1 and type 2 interactions. As defined in section 2.1, Type 1 describes the situation in which a shift of a matrix dislocation by a perfect Burger's vector on a particular slip system maintains the ordered precipitate

103

structure while type 2 does not; thereby creating an APB. In type 1, no elongation of the ISF is observed as the dislocations do not disrupt the order of the precipitates. In type 2, the ABP energy and the resolved shear stresses on the dislocation partials determine the formation and elongation of the ISF.

2. Micropillar compression was performed to activate type 2 interactions in two different loading orientation. The results provided direct observation of the loading orientation on the activation of slip versus twin in type 2 interaction. The experimental observation is consistent with the MD results, showing that deformation twinning activates when the resolved shear stress on the trail partial is lower than that of the leading partial (described as the ratio between Schmid factors of the dislocation partials)

3. Additionally, MD results provided a possible twin formation mechanism from an energy-based approach; thus, it confirms that the type 2 interaction between the dislocations and the Pt_2Mo-structured precipitates lead to the deformation twinning in Ni-Cr type alloys.

4. The strain burst analysis has shown that deformation twinning reduces the plastic intermittency as compared to dislocation slip.

6.2. Voids

6.2.1. Influence of void swelling on grain and grain boundary plasticity of ~33 dpa irradiated 304SS.

6.2.1.1. Background

Irradiation assisted stress corrosion cracking (IASCC), is a major degradation mechanism for light water reactor components. To understand and develop predictive models for IGSCC for materials in nuclear reactor environment, we need to understand how irradiation-induced defects on crack propagation. In particular, long term high temperature neutron irradiation can cause void swelling in austenitic stainless steels; therefore, it is of high interest to understand how void microstructure influences the IGSCC of neutron irradiated materials.

In this study, 33 dpa neutron irradiated 304SS with two different swelling level (2% and 3.7%) are examined. Macroscale crack growth rate tests were performed at Idaho National Laboratory showing that the crack growth rates are particularly low compared to other neutron irradiated stainless steels. This leads to the hypothesis that low amount of void swelling can reduce IGSCC susceptibility for neutron irradiated materials. The crack growth rates for two different swelling conditions are reported in Table. 6.4; and the values are compared against other neutron irradiated stainless steels in Figure

Table 6.4. Crack growth rates of two different swelling conditions performed at Idaho National Lab

Applied Stress Intensity	CT1 (3.7% swelling)	CT2 (2% swelling)
K=16ksi√in	7.2×10^{-10} mm/s	1.9×10^{-9} mm/s
K=18ksi√in	8.0×10^{-10} mm/s	4.9×10^{-9} mm/s
K=20ksi√in	2.1×10^{-9} mm/s	Not available
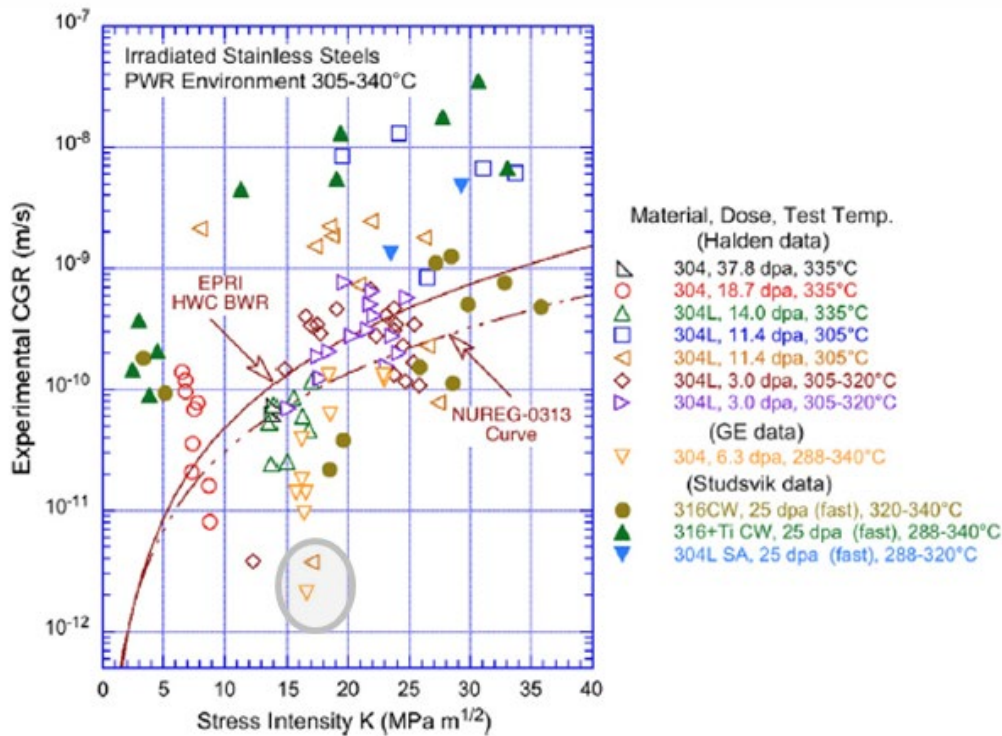
Figure 6-24. Experimental crack growth rate versus stress intensity. The shaded circle indicates the level the 2% and 3.7% swelling 304SS fall into. [188]

6.2.1.2. Methods

The material block, AISI 304 stainless steel, was used in the reflector assemblies in the Experimental Breeder Reactor-II fast reactor. Two samples were cut from the 304SS material and provided by Idaho National Laboratory. Two samples have seen 33 dpa of neutron dose where sample 1 has <2% swelling and sample 2 has 3.7% swelling. The time-averaged temperature was 390°C; however, due to gradient gamma heating, the maximum average temperature inside material block is estimated to be about 460°C.

Two sets of neutron-irradiated 304SS are received. One set of specimens are the CT-test specimens after the crack growth rate tests. The other set of specimens are the bulk neutron-irradiated specimens. Figure 6.25A shows the SEM image of the polished surface of the Ct-test specimen. Figure 6.25B shows the zoomed-in view of the crack tips. The microscale tensile bars can be selected to contain the crack tip or contain a regular grain boundary. In this study, we examine both the normal grain boundaries and grain boundaries containing a crack tip
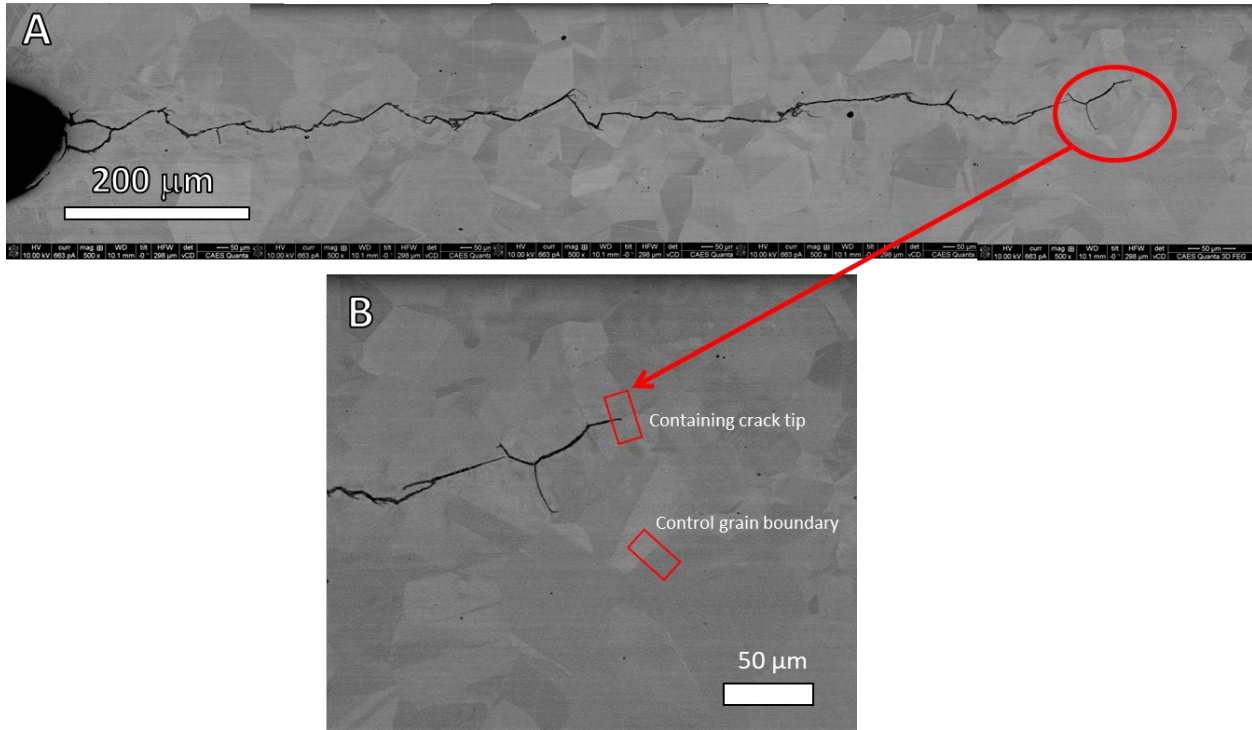

Figure 6-25. A) SEM image of a CT-specimen after the crack growth rate test. B) Zoomed-in SEM image of the crack tip region.

A FEI Quanta 3D FEG dual beam was utilized for the microtensle fabrication and testing. First, the electron back scatter diffraction (EBSD) was used to map out the grain orientations, and the high angle grain boundaries were selected for testing, as shown in Figure 6.26A. The foil, which contains the grain boundary of interest, was lifted out with the micromanipulator and mounted on the Push-to-Pull (PTP) device, manufactured by Bruker. The foil was then made into tensile bar and cleaned at 15 keV and 0.1 Na to avoid FIB damage, as shown in Figure 6.26B. The tensile tests were performed *in situ* SEM using the PI-88 Picoindenter. The tests were done in constant displacement rate of 10 nm/s and the tensile bars were tested to failure. Figure 6.26C shows the image of a fracture tensile bar. TEM was performed to examine the voided microstructure.
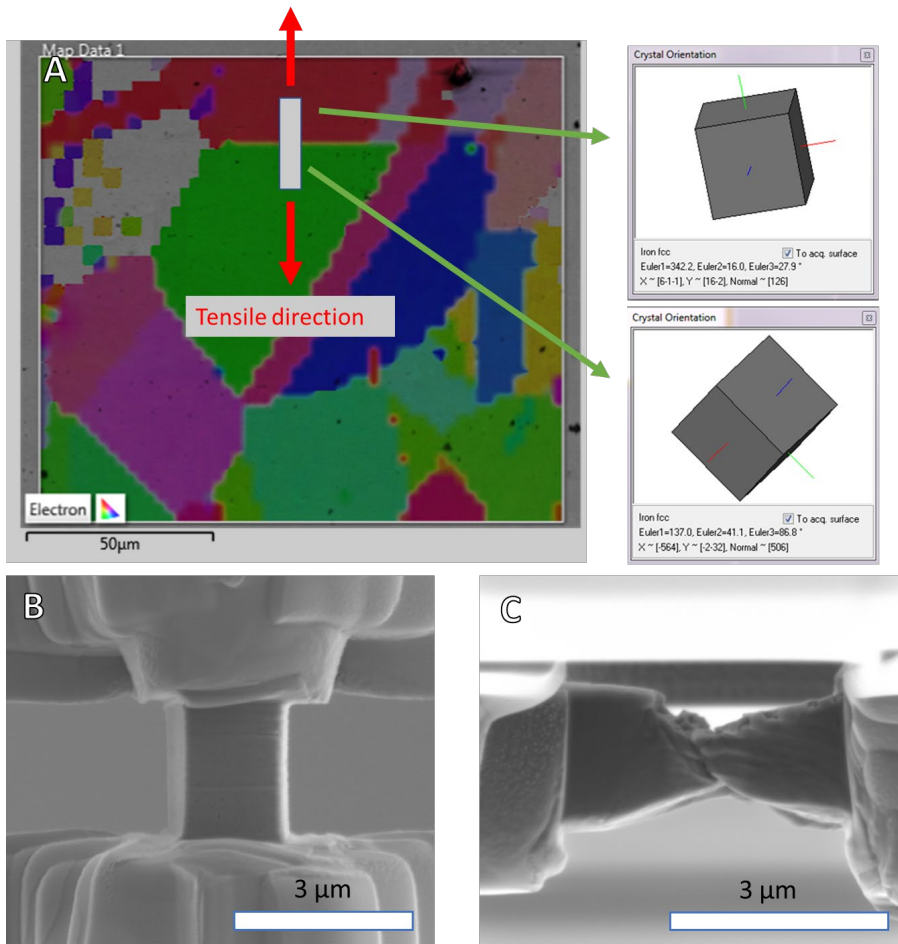
Figure 6-26. A) EBSD map overlaid on the SEM image showing the grain boundary selection process. B) Strain-stress curves of the Digital-Image corrected curve and the machine-measured curve. C) A representative SEM image of the deformed microtensile bar

6.2.1.3. Results and Analysis
6.2.1.3.1. Transmission Electron Microscopy

Figure 6.27 shows the montage image of high angle annular dark field (HAADF) images and the bright field TEM images showing the voided microstructures. The images show a uniform distribution of voids within the grains; and voids are not observed to nucleate on the grain boundaries.
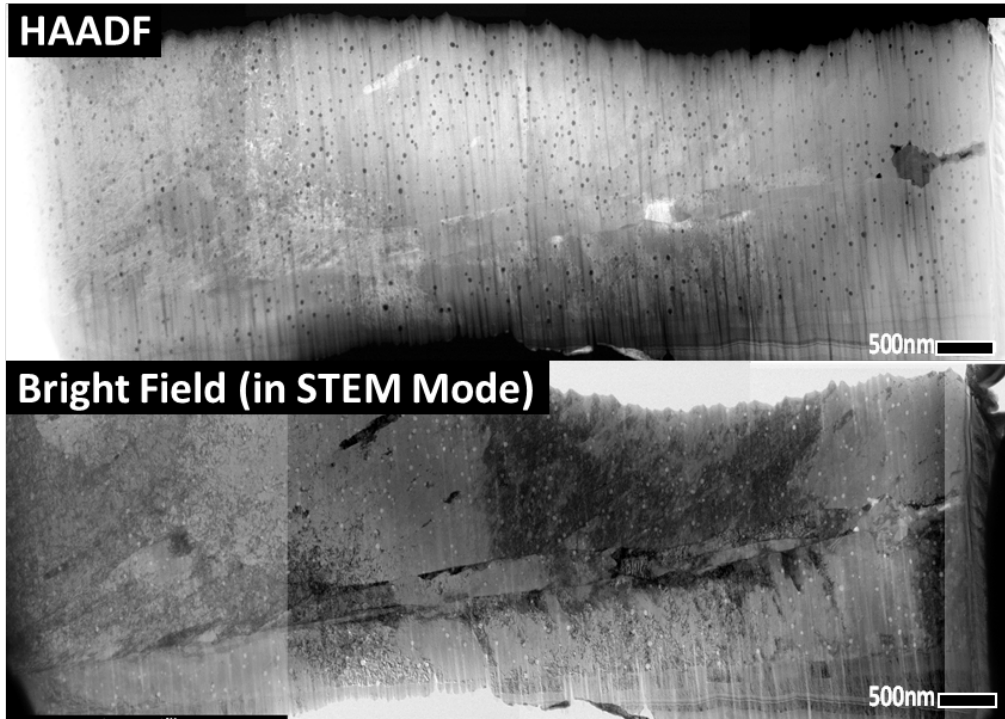
Figure 6-27. A) HAADF image montage. B) Corresponding Bright Field TEM image

Aside from the voided microstructure, the microstructure consists of a dense distribution of stacking faults and dislocations caused by radiation damage (Figure 6.28A). The dense distribution of stacking faults and dislocation loops are known to induce severe strain localization. However, the combined effect between voids and stacking faults/loops on plasticity have not been assessed microscopically. Figure 6.28B shows a representative zoom-in BF TEM image of the voided microstructure. ImageJ was utilized to quantify the size distribution of the voids, as shown in Table. 6.5.

Figure 6-28. A) Bright Field TEM showing a dense distribution of stacking faults and dislocations due to radiation damage. B) A representative BF TEM image of the voided microstructure for void size quantification.

Table 6.5. Void size distribution
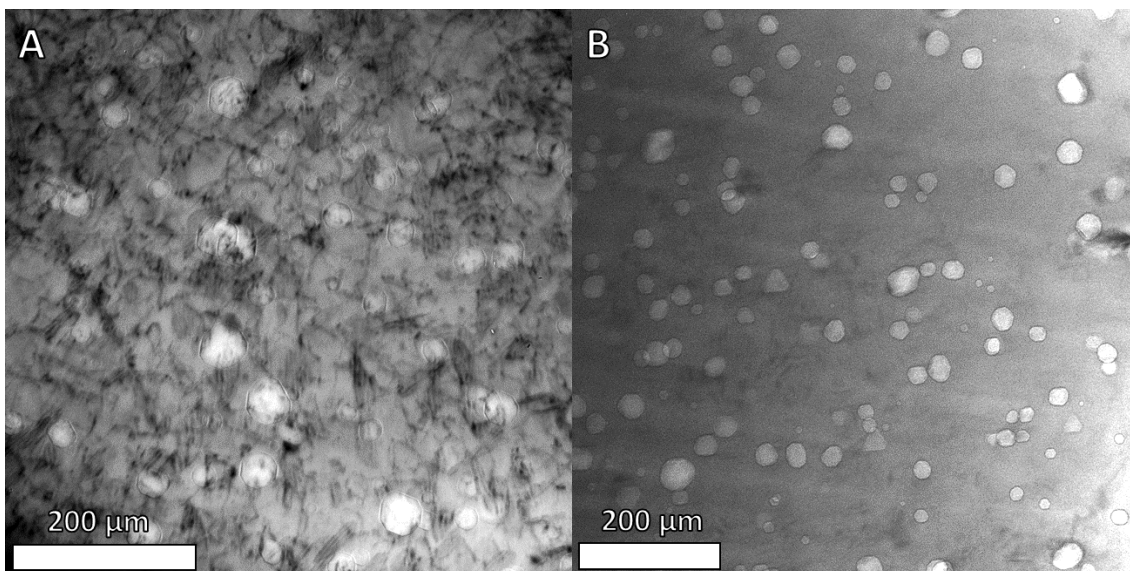
	Mean Void Size (nm)	Standard deviation (nm)
2% swelling sample	23.3	9.6
3.7% swelling sample	25.3	9.6

6.2.1.3.2. Nanoindentation

Nanoindentation was performed on the two neutron-irradiated specimens and the unirradiated 304SS material. The hardness versus depth curves are shown in Figure 6.29. The hardness values between the 2% and 3.7% swelling are quite similar. The change in hardness after the neutron irradiation is ~1.1-~1.5 GPa. The hardness values of the neutron irradiated materials are consistent with hardness values of 10 dpa proton-irradiated materials measured previously [115]. The similar hardness values suggest that the 33 dpa neutron-irradiated materials have passed the saturation dose for hardness increase.
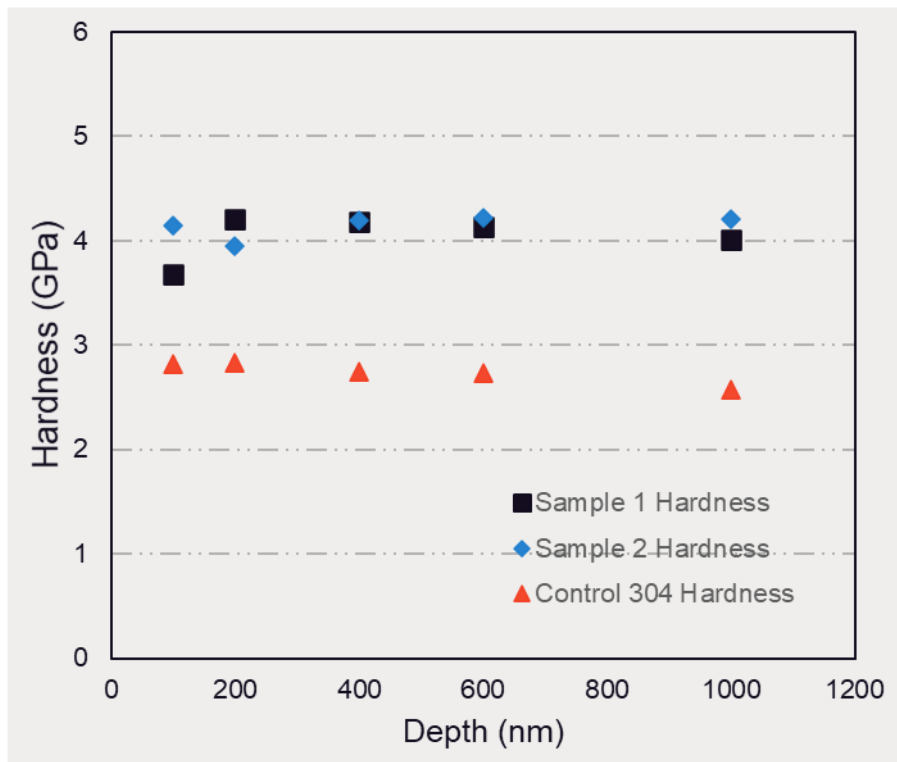
Figure 6-29. Nanoindentation hardness versus depth curves. Samples 1 and 2 correspond to 2% and 3.7% swelling 33 dpa neutron-irradiated materials. The control 304SS is the unirradiated condition.

6.2.1.3.3. Microscale tensile testing

The bicrystal microtensile tests containing high angle grain boundaries are tested to failure. Figure 6.30A shows a representative SEM image after testing. All the microtensile bars of this type deformed and failed within the grains, as shown in Figure 6.30B. The neutron-irradiated materials deformed in a ductile fashion with the absence of slip formation (Figure 6.30A). The corresponding stress-strain curves of these tests show no significant strain burst and stable plastic flow (Figure 6.30C). The observation of ductile deformation behavior in the 33 dpa neutron irradiated specimens is remarkable. Although the microstructure consists of a dense distribution of stack faults and loops, which are known to induce strain localization, no localized slip was observed. The 33 dpa samples with <2% and 3.7% swelling have the average CRSS values of 409 MPa and 346 Mpa, and the total elongation of ~60-67%. The microtensile test of proton-irradiated material, in Chapter 5, shows that the 10 dpa proton-irradiated shows an average CRSS of 437 and a total elongation of ~11%.
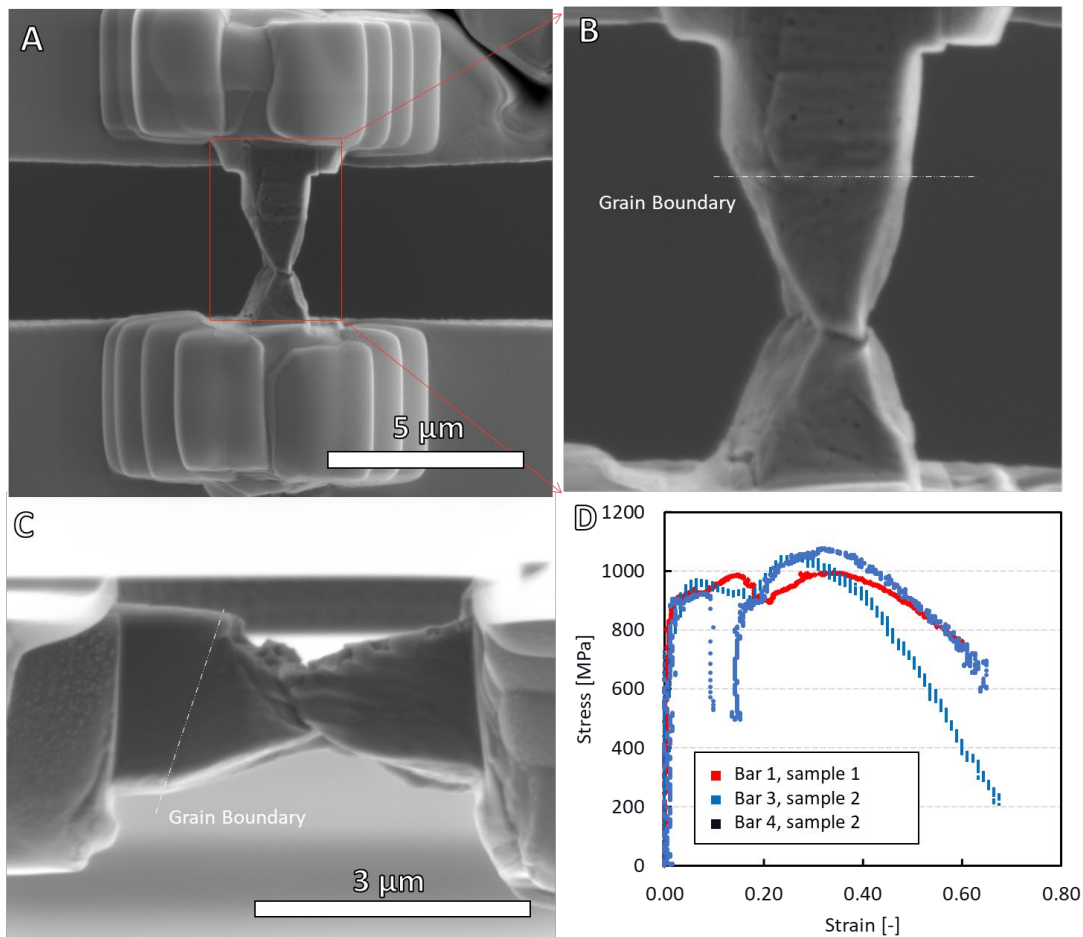
Figure 6-30. A) SEM image of the deformed Bar 1 sample 2. B) Zoom-in SEM image of Bar 1 sample 2 showing the deformation and failure took place within the lower grain. C) SEM image of the deformed bar 1 sample 1. D) DIC-corrected stress-strain curves of a few tests in both samples. Sample 1 and sample 2 correspond to 33 dpa neutron-irradiated 304SS with ~2% and ~3.7% swelling, respectively.

The second type of bicrystal testing performed was shown in Figure 6.31. The grain boundary is notched (granted that the notch is blunt) in order to reduce the cross-sectional area and increase the applied stress seen by the grain boundary. Figure 6.31 shows the stress-strain curve and the corresponding SEM images of bicrystal microtensile sample at different points on the stress-strain curve. There is visible motion of the grain boundary, however the failure did not take place at the grain boundary. This suggests that the grain boundary is subjected to very high normal stress compared to the rest of the test sample, however the grain boundary remains strong.
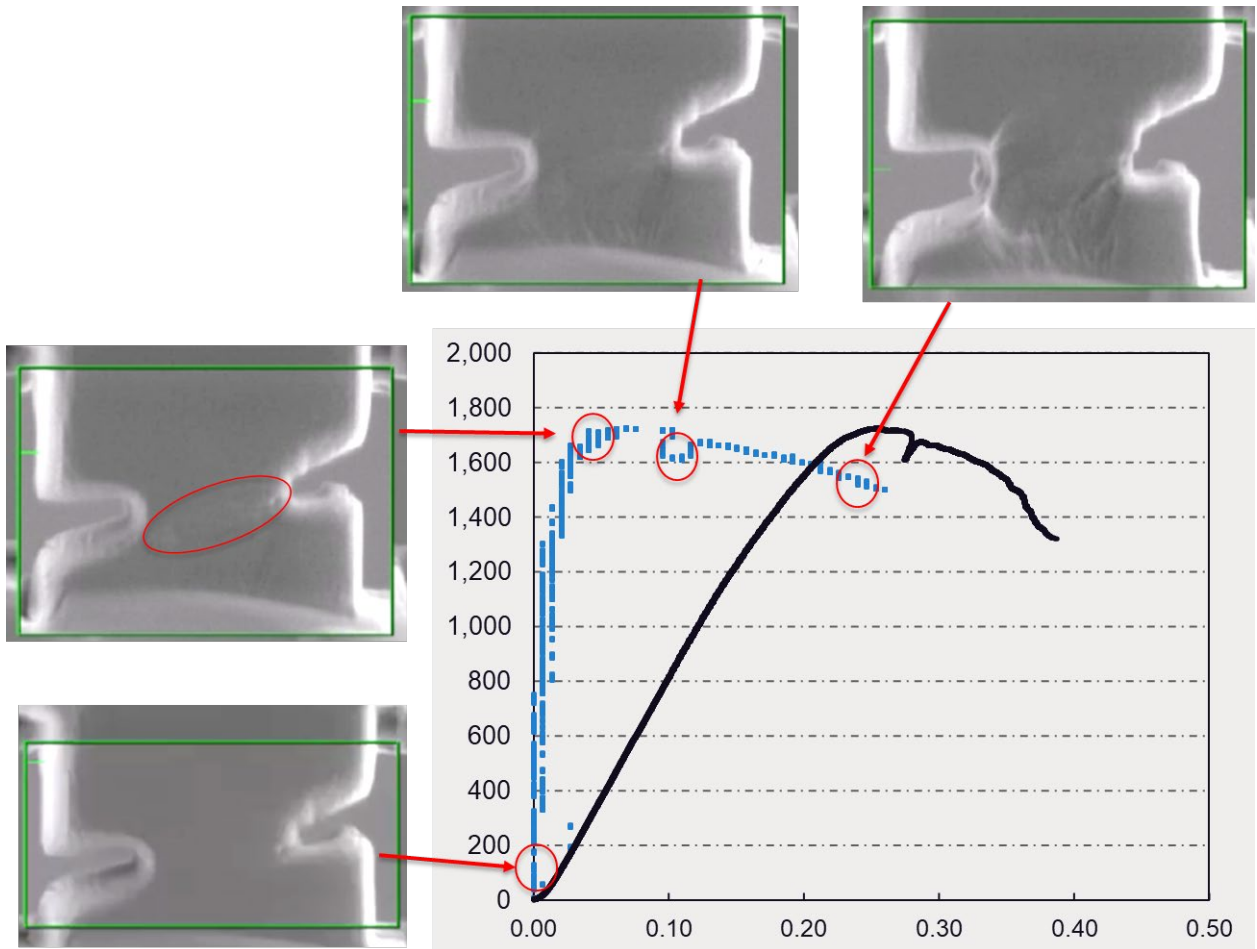

Figure 6-31. Blunt notched bicrystal microtensile bar's stress-strain curve

To further assess the role of voids on initiation intergranular cracking, the bicrystal microtensiles containing the crack tip are tested, as shown Figure 6.32. Figure 6.32A-E show the SEM snapshots corresponding to different points in the stress-strain curve. The crack opens (Figure 6.31C) and

becomes blunted during the deformation. The necking failure eventually took place within the lower grain. In three different bicrystal microtensile testing setup, no grain boundary failure was observed.
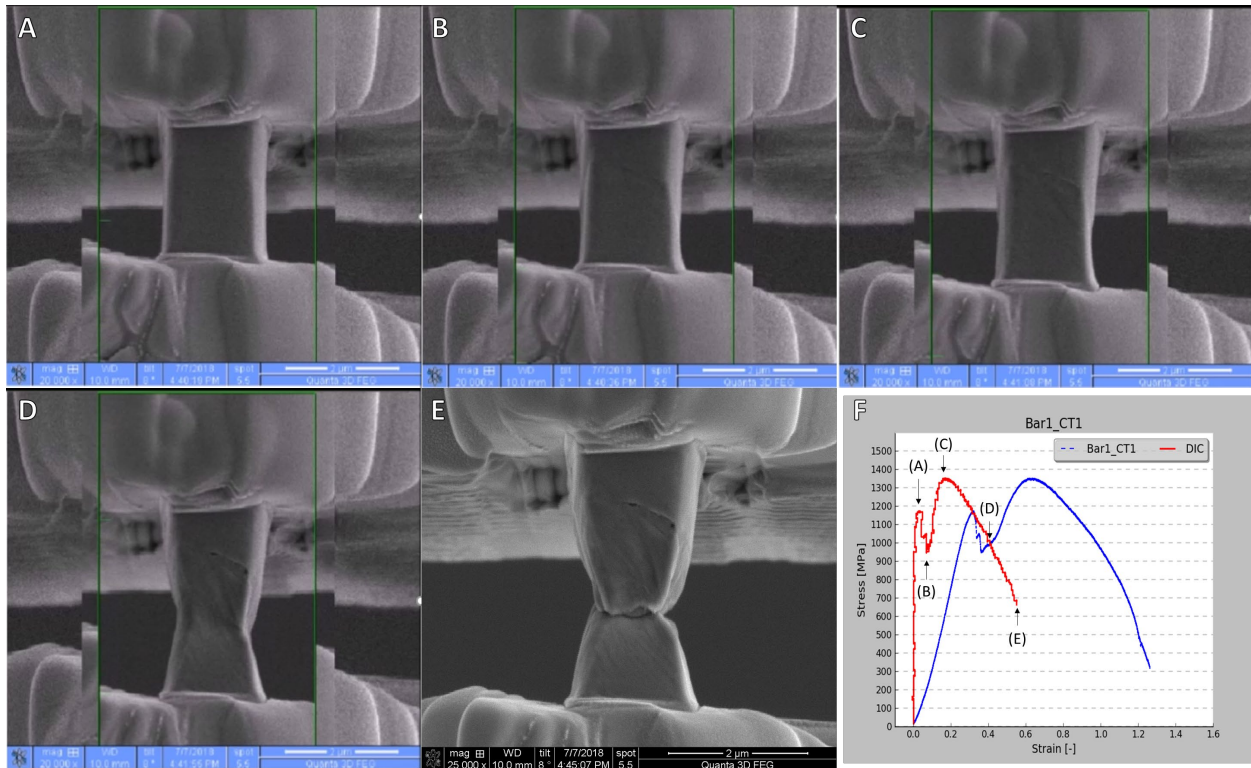

Figure 6-32 Bicrystal microtensile test containing a crack tip. (A), (B), (C), (D), and € correspond

6.2.1.4. Discussion
6.2.1.4.1. The role of intragranular voids on inhibiting strain localization

The dislocation and void interaction via molecular dynamics have been extensively studied [189]. It was shown that the dislocation can either shear or loop around the voids depending on the void size and distribution. The voids remain stable and are not destroyed/dissolved after the dislocation shearing, unlike the radiation-induced loops and stacking faults. Figure 6.33 shows the molecular dynamics simulation of an edge dislocation and a 10 nm void under 300 MPa shear stress for FeNiCr of the same composition as 304SS. The simulation was run in periodic boundary condition to see the effect of successive dislocation passing, it was found that the void retains its strength after multiple dislocation passing. For the neutron irradiated 304SS materials in our study, the dislocations would have to loop about the voids due to the large void size. Due to the stability of the void, the defect free channel cannot be created in contrast to the microstructure containing only radiation-induced loops and stacking faults.
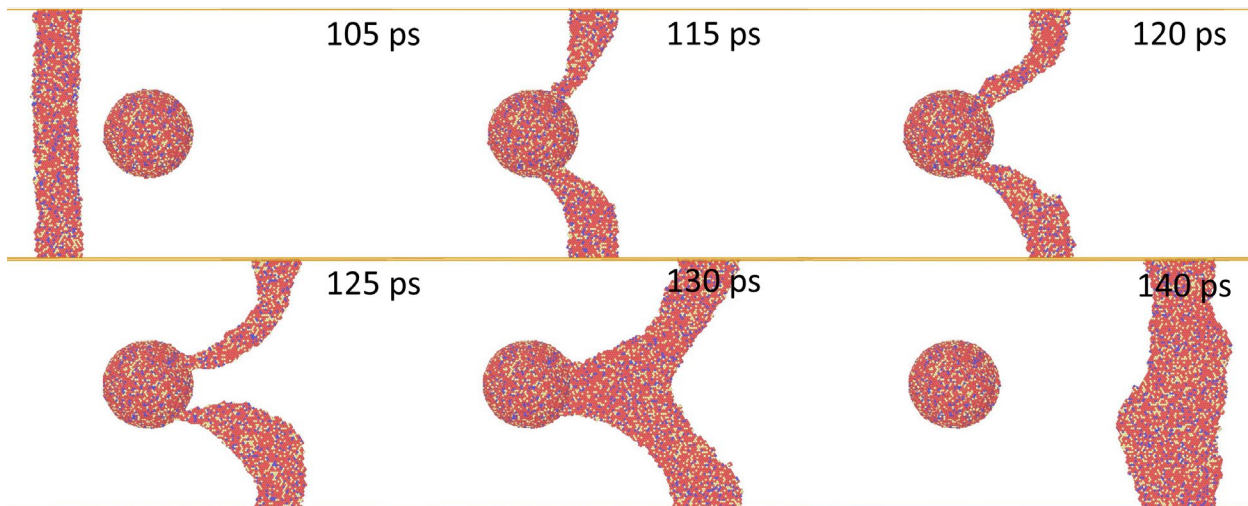
112

Figure 6-33. Molecular dynamics simulation of an edge dislocation – 10 nm void interaction under 300 MPa shear stress in FeCrNi alloy with the same composition as 304SS

Furthermore, the different types of bicrystal microtensile tests performed here directly demonstrate the effect of suppressing strain localization in irradiated materials with voids/cavities on grain boundary failure. In contrast to intergranular void and bubbles which are known to increase the grain boundary stress concentration, the intragranular voids provide a beneficial role of suppressing strain localization. However, for high level of swelling, the materials can no longer deform plasticly and therefore fracture brittlely, as reported in [7]. Comparing with the crack growth rate test shown in the background section, the microscale data rationalize the observation of the very low crack growth rate in the 33 dpa neutron irradiated materials with 2-3.7% void swelling compared to other irradiated materials with no void swelling. This suggests that low level of intragranular void swelling has a beneficial effect in inhibit intergranular cracking.

6.2.1.4.1. Internal block volume concept

In addition to the effect of voids on the grain boundary failure, the void microstructure also has a strong influence on plastic deformation of the grains. In the 2D interface defect, the block volume model was used to describe the influence of interface on the grain plasticity. Depending on the BVR ratio, the deformation can go from multiple slip coupled with strain burst to stabilized plasticity and necking. In a similar fashion, the void microstructure has a similar effect on grain plasticity as it suppresses localization. Remarkably, macroscopic-like necking can take place within microscale single crystal as the result. We introduce the internal block volume concept to describe the potential usage of void microstructure to suppress unstable plastic flow in microscale volume.
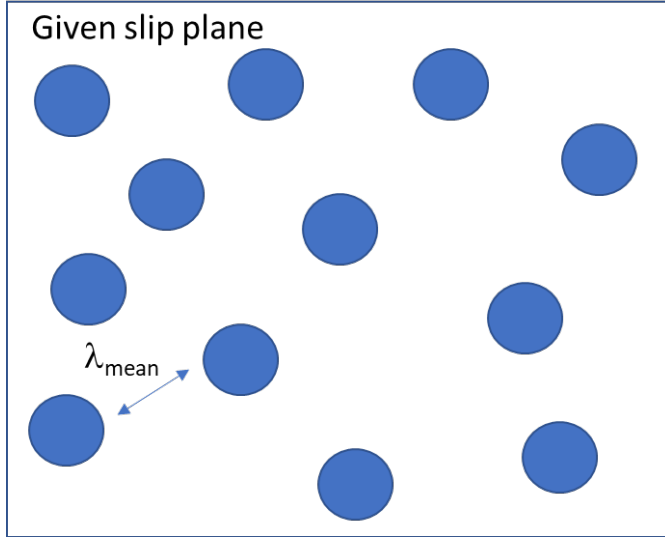
Figure 6-34 Schematic of a slip plane containing a uniform distribution of voids where λ$_{mean}$ is the defect mean spacing

Figure 6.35 shows the schematic used for the derivation. Let us assume that it requires a minimum number of voids, k, on individual slip plane to suppress strain burst and unstable plastic flow for given sample dimension.

$$\lambda_{mean} = \frac{1}{\sqrt{N_{void} d_{void}}}$$

Where N_{void} = number density (m^{-3}), d$_{void}$ = diameter (m)

Let A to be the area of the slip plane and B be the angle between the slip normal and the normal loading direction. The average number of voids, <n> , on a given slip plane is calculated as

$$< n >= \frac{4}{\pi} \frac{A}{\lambda_{mean}^2}$$

Let P(k) to be the total probability of finding k voids or less than in any active slip plane. Assuming random distribution, P(k) is calculated as:

$$P(k) = \sum_{k=0}^{k} e^{-<n>} \frac{< n >^k}{k!}$$

For k = 30 voids for a 1 um by 1 um by 2 um rectangular pillar, loading direction = [001], we can then generate the internal blocked volume map a shown in Figure 6.36.
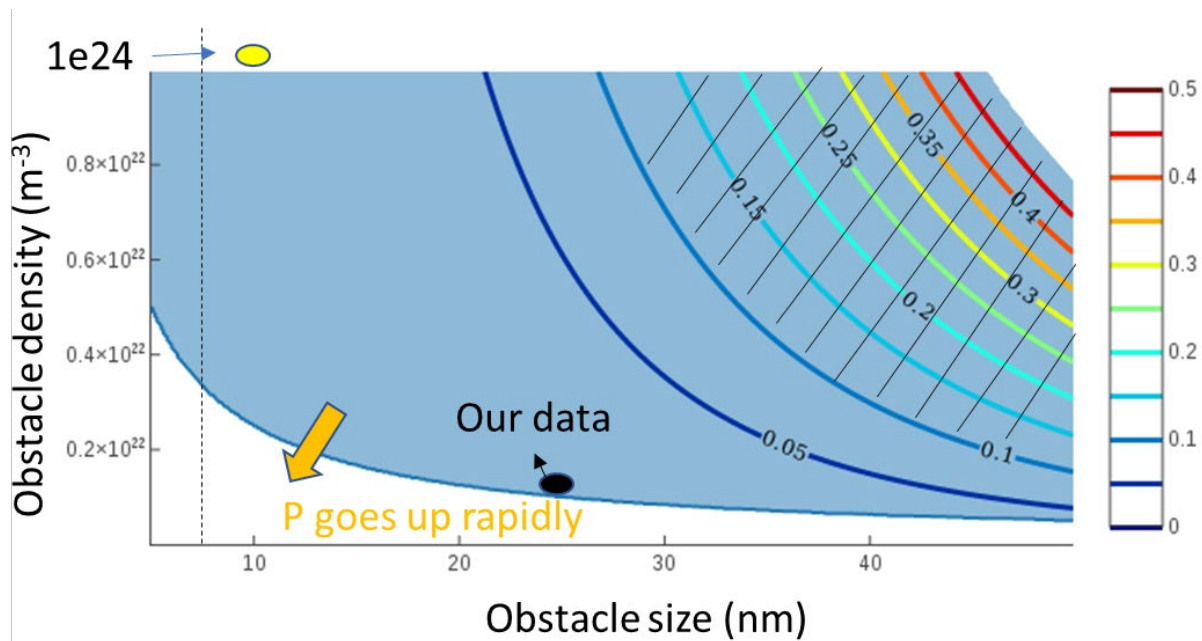
Figure 6-35 The contour map of P(k) as a function of obstacle size and obstacle density. The shaped region has the P(k) value of less than 10^{-4}. The contour lines indicate the volume fraction of the void swelling. The black-dashed region has the void volume fraction of greater than 10%

The shaded region of the contour map shows the range of void size and obstacle density where the probability of finding less than k voids is less than 10^{-4}. In other words, these distribution of void size and density can effectively stabilize plastic flow and minimize strain localization. Ref [190] have observed stabilized plastic flow in the single crystal Cu nanopillars, containing a high density of sub-10 nm He bubbles. The data is indicated by the yellow circle. Our 2-3.7% swelling data is indicated by the black circle. However, the map is not applicable for excessive void swelling (>10%) where plasticity is fully suppressed and brittle failure can immediately take place, which have been observed in nuclear reactor materials. The challenge is the k value is unknown and will require extensive dislocation dynamics and experimental data collection to determine the k value. It will be the opportunity for future work.

6.2.1.5. Conclusion

Void microstructure has been directly shown via microscale to suppress slip and strain localization. We indicate that low level of void swelling has a beneficial effect in inhibiting crack initiation and promoting crack blunting. Furthermore, the stability of void strongly increase the ability to control unstable plastic flow at the microscale.

Chapter 7 Thesis Discussion

For each study, the study discussion section has provided in-depth analysis and discussion for different defect types. In this chapter, we provide a comprehensive discussion of the role of mechanical stability of defect on plastic deformation and failure.

7.1. Mechanical stability of defect and plastic deformation

Here we define the concept of mechanical defect stability as the amount of plastic shear strain required to destroy the defects within particular slip bands and thus substantially lower the resistance of dislocation glide. Figure 7.1 arranges the different defect types in increasing order of defect stability. We observed a clear trend that the deformation behaviors and the stress-strain curves follow an increasing order of plastic stability as the defect stability increases. Low-stability defects such as radiation-induced loops and radiation-induced-disordered precipitates cannot retain their strength after very low level of plastic shear strain. The channels of low dislocation resistance can be quickly created after the initial dislocation glide interactions. The dislocations preferentially glide within those channels leading to localized slip and strain localization as a result, as shown in Figure 7.1A2 and Figure 7.1B2. As the defects increase in stability, it requires higher level of plastic shear strain (e.i. excessive dislocation glide) to destroy the strengthening defects and create defect free channels. Shearable medium size metallic precipitates and intermetallic precipitates (Figure 7.1C) are considered to have medium level of mechanical stability. For these defects, the plastic strain level required to destroy/dissolve these defects are much higher compared to SIA loops and LRO precipitates with low level of mechanical defect stability. The strain burst (unstable plastic flow) is significantly reduced compared to defects with low stability. For defects of high level of mechanical stability such as voids, they can completely suppress strain localization as they can excellently retain their strength through out the duration of the deformation. Figure 7.1D2 demonstrates the full suppression of channeling and the enabling of macroscopic necking in the microscale bicrystal tensile sample. The corresponding stress-strain curve shows the stabilized plastic flow as the result. To test the limit of the mechanical stability of defect on deformation and failure, we utilize hard coating interface as a 2D defect. In Chapter 5, using the blocked volume concept, it was demonstrated that the stability of the interface and the "blocked" volume governs the deformation and failure of the grain. As shown in Figure 7.1E2, full suppression of slip and strain localization took place for high level of BVR sample. The stress-strain curve shows significant strain hardening and macroscopic like necking behavior. By using uniaxial microscale tests, we clearly demonstrate there is a strong correlation between the mechanical stability of defects and plastic stability, in which the plastic deformation can be controlled from localized slip to fully macroscopic-like necking.
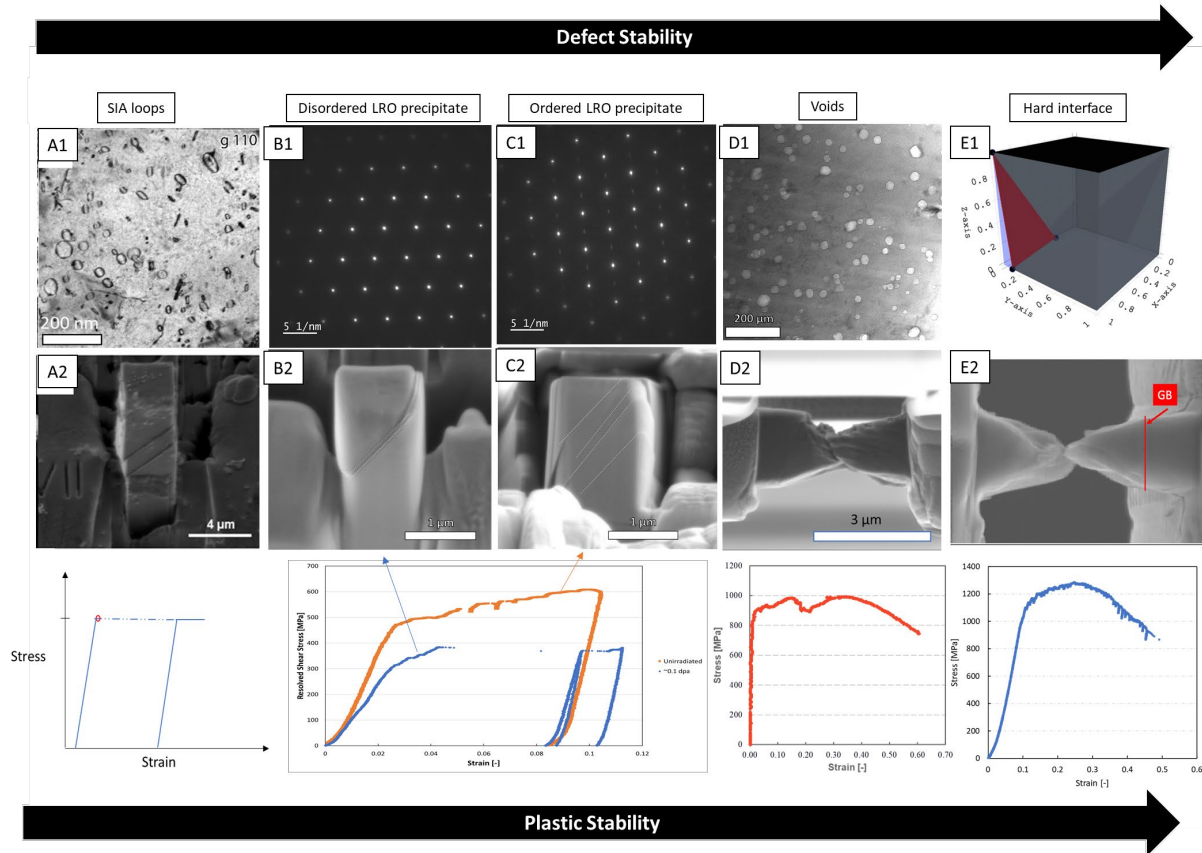
116

Figure 7-1. Defect stability versus plastic stability. The different defect types and the corresponding deformation are arranged in increasing order of defect stability.

The microscale tensile and compression tests show that defects with low mechanical stability induces severe strain bursts which correspond to strain localization. In chapter 6, we have discussed and derived the relationship between strain burst and the mechanical stability of defects. As shown in the schematic of Figure 7.1, we consider a scenario where localize slip and strain burst take place. At the point of strain burst C, the shear strain rate increases abruptly as the result of the localized slip. By combining Eqs. 6.2-6.5, the expression for the shear strain rate at the point of mechanical instability is as follows:

$$\dot{\gamma}_{C^+} = \frac{b^2 \rho \tau_{c,C^-}}{B_{C^+}} \quad Eq.\ 7.1$$

Where $\dot{\gamma}_{C^+}$: shear strain rate at the point of strain burst, b: dislocation Burger vector, τ_{c,C^-}: critical shear stress required to glide through the defects, B_{C^+}: slip resistance
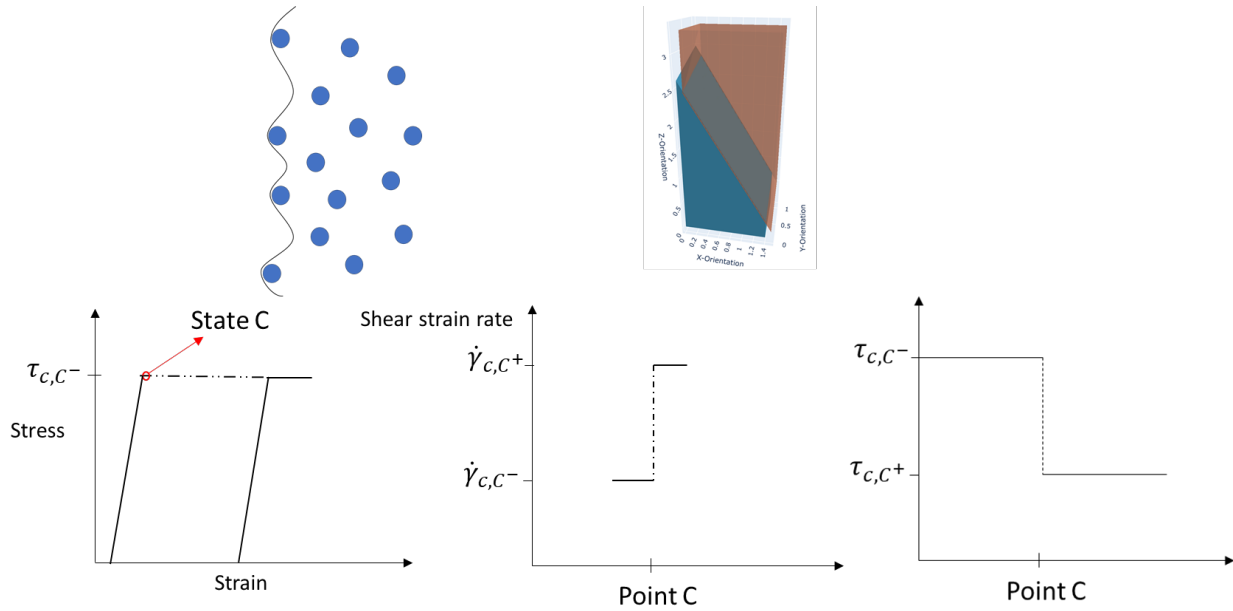
117

Figure 7-2 Schematic for linking strain burst and defect stability

The degree of strain burst can be described by the increase in shear strain rate at the point of the instability. The Eq. 7.1 describes the situation where the strength of defects on a given slip plane decreases dramatically (formation of defect free channel), the driving force (due to the current applied stress) is significantly greater than the stress required for dislocation glide in the defect channel, leading to the dramatic increase in dislocation velocity manifested as strain burst. The Eq. 7.1 states that the degree of strain burst is proportional to the strength of the defects before the formation of the defect free channel and inversely proportional to the material slip resistance in those channels (relatively small). In other words, the stronger the defect the more severe the strain localization for defect with low stability. The strength of the defect, in this context, is described by the critical resolved shear stress of the single crystal microscale sample. The Eq. 7.1. can be used to explain the role of interstitial Nitrogen on strain localization (Chapter 3). By changing the radiation-induced loop size and distribution with the addition of interstitial Nitrogen, the intensity of the strain localization can be increased or decreased depending on the change in the distribution and size. For future work, the mechanical testing of single crystal iron with different Nitrogen contents is desired in order to confirm the relation between defect strength and localization.

7.2. Defect stability and intergranular crack initiation

Previous section discusses how the mechanical stability of defects influence the plasticity within the grain. Here we discuss the its role on the initiation of intergranular failure by comparing radiation-induced loops (Chapter 4) and voids (Chapter 6). Figure 7.3 present the schematics demonstrate the scenarios when voids are dominant defect (Figure 6.7.3A) and radiation-induced loops are dominant (Figure 6.34B). In the void-dominant microstructure, the stability of

the voids prevents the formation of defect free channels, inhibiting localized slip. In contrast, the metastable radiation-induced loops can get cleared to form defect free channels promoting slip localization. The localized slip significantly increases dislocation pile-up at the end of the free channels at the grain boundary, thus increasing the stress intensity to initiate crack formation. It has been shown that strain localization has a direct influence on intergranular crack initiation of irradiation materials containing dominant microstructure of radiation-induced loops [28,191]. Another interesting aspect is that although the 33 dpa neutron irradiated materials contain a dense distribution of defects (SIA loops and stacking faults) in addition to the voids, it appears that the plasticity is governed by the most stable defect type within the slip plane.
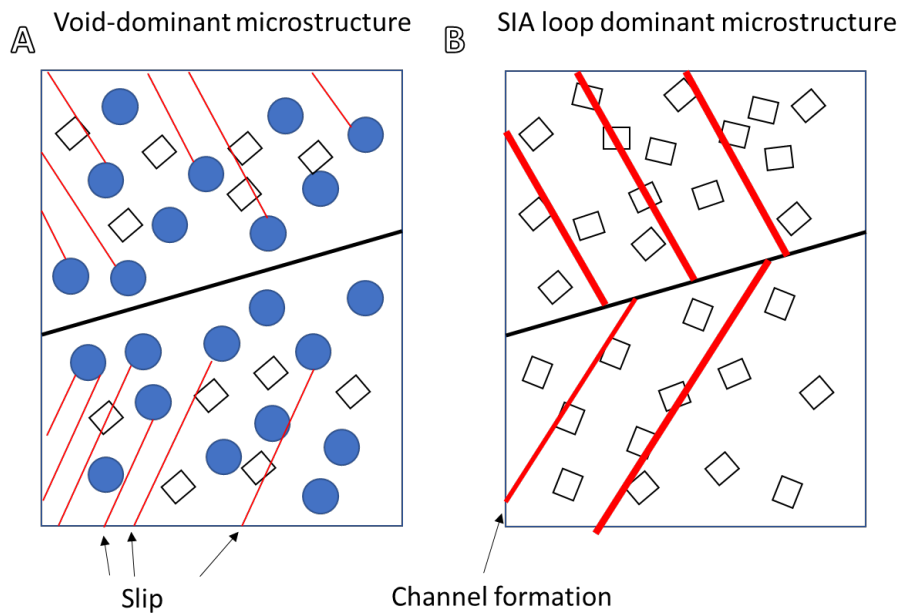

Figure 7-3   Schematic of A) void-dominant microstructure bicrystal and B) SIA loop dominant microstructure bicrystal

Chapter 8 Summary and Future Work

Figure 8.1 summaries the different applications of SSMT performed in this thesis. Different techniques including micropillar, microtensile, and bicrystal microtensile have be developed to study both grain and grain boundary behaviors. We found that SSMT provides the ability to directly observe deformation behaviors with great control of material parameters. The work in this thesis was limited to room temperature testing with displacement rate of $\sim10^{-3}$. For future work, we aim to expand the capability of SSMT to a wide range of temperature (from cryogenic to high temperature) and strain rate (low strain to high strain rate). Nevertheless, the work performed in this thesis contributes to the ever-growing applications of SSMT for assessing engineering materials. The key findings are summarized as follows:

- The mechanical stability of defects directly controls the plastic stability (strain burst response) and strain localization. Consequently, the defect stability also plays a big role in inhibiting intergranular cracking as it reduces strain localization.
- Nitrogen interstitial modifies the radiation-induced microstructure via defect trapping of the point defect clusters, leading to larger loop sizes with increasing nitrogen content (Chapter 3).
- Radiation-induced (SIA) loops lead to severe strain localization at the microscale and the observation was consistent with the macroscopic deformation (Chapter 4)
- The blocked volume concept was introduced to describe the influence of interfacial constraint on the plastic flow of grains at the microscale. For high BVR, the strain burst and plastic instability are fully suppressed, enabling uniform elongation and macroscopic-like necking behavior in single crystal microscale samples (Chapter 5)
- High angle martensitic lath boundaries are found to be more susceptible to intergranular failure compared to low angle martensitic lath boundaries in irradiated tempered-martensitic alloys (Chapter 5)
- The novel microscale testing technique of a bicrystal was developed to measure oxidized grain boundary strength. The strength of oxidized grain boundaries of different thermal history in Nickel-based alloy 600 has been assessed (Chapter 6)
- It was found that low level of radiation significantly reduces the mechanical stability of LRO precipitates via irradiation in irradiated Nickel-based alloy 718. (Chapter 7)
- For LRO Pt2Mo-structured precipitates, the role of loading orientation controls the activation of slip and twinning. Twinning was found to stabilize plastic flow as compared to slip (Chapter 7)
- Voids were found to be highly mechanically stable. The strain localization and slip were fully suppressed in 33 dpa neutron-irradiated 304SS with 2-3.7% void swelling. The suppression of strain localization shows a beneficial role in inhibiting intergranular crack initiation. (Chapter 7)
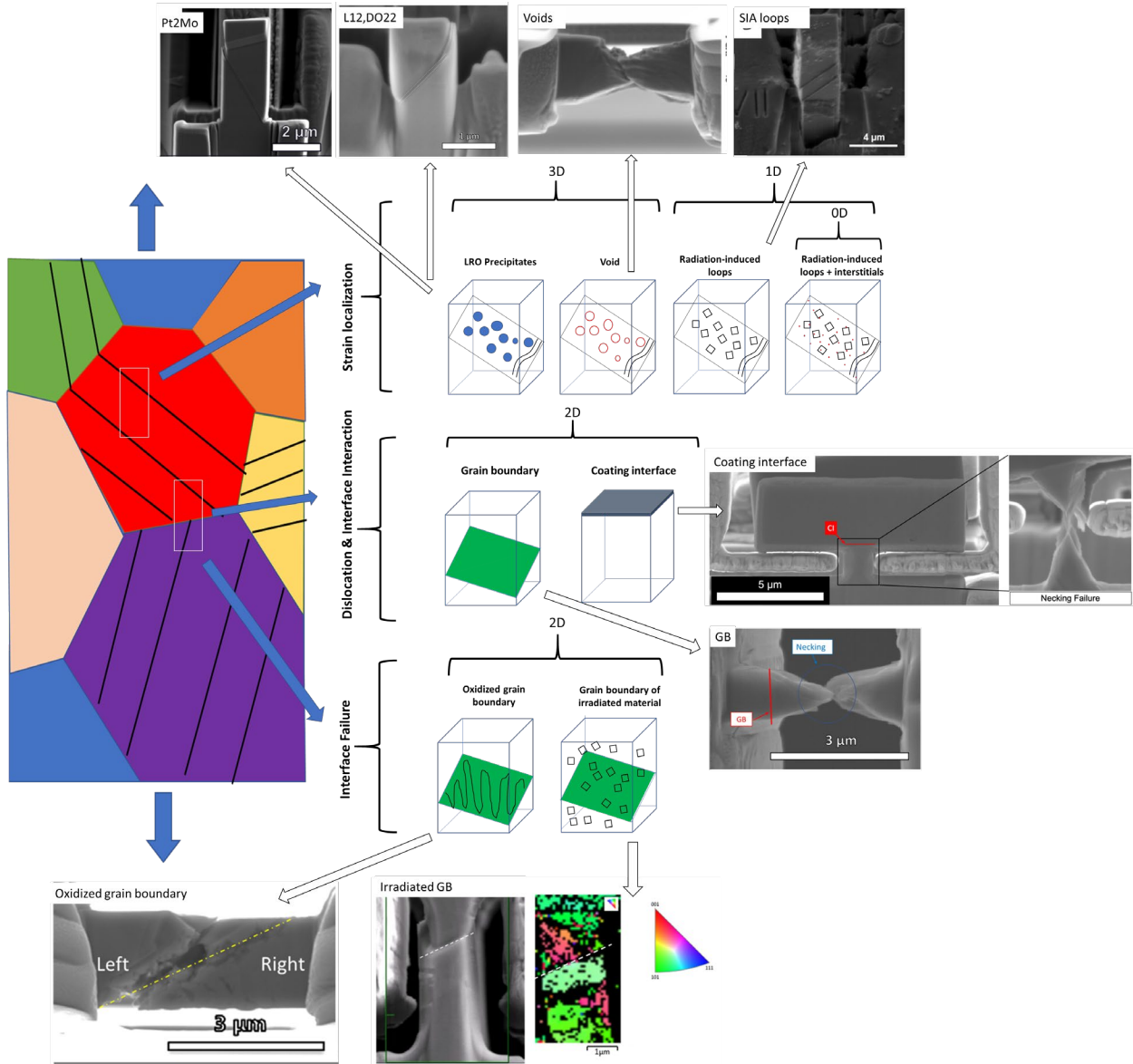
Figure 8-1. Summary of the use of SSMT in this thesis

References